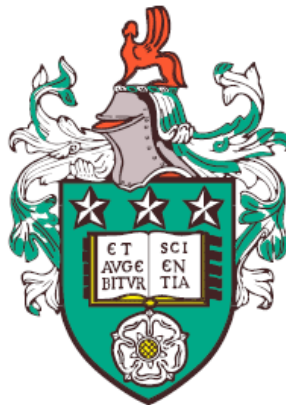


# Quasi-dimensional modelling of Exhaust Gas Recirculation and Fuel Stratification in SI engines

Jamie Karl Smith  
BSc Hons.

Submitted in accordance with the requirements for the degree of  
*Doctor of Philosophy*



The University of Leeds  
School of Mechanical Engineering

March 2019

## Publications & Copyright

The candidate confirms that the work submitted is his own, except where work which has formed part of jointly authored publications has been included. The contribution of the candidate and the other authors to this work has been explicitly indicated below. The candidate confirms that appropriate credit has been given within the thesis where reference has been made to the work of others.

In the following papers the candidate completed the derivation of theoretical sub-models and their implementation into a predictive code. The results from the predictive code was also completed by the candidate. The co-authors between them provided CFD turbulence data, experimental data for model validation purposes and technical discussion on the results.

Chapter 4 is largely based on a jointly authored journal article: Jamie Karl Smith, Phil Roberts, Alexandros Kountouriotis, David Richardson, Pavlos Aleiferis and Daniel Ruprecht, **A comparison of EGR correction factor models based on SI engine data**, SAE International Journal of Engines, 2018 - accepted 29/11/2018.

The validation results in Chapter 5 are based on a jointly-authored journal article: Jamie Karl Smith, Phil Roberts, Alexandros Kountouriotis, David Richardson, Pavlos Aleiferis and Daniel Ruprecht, **Thermodynamic modelling of a stratified charge spark ignition engine**, International Journal of Engine Research, 2018, [doi:10.1177/1468087418784845](https://doi.org/10.1177/1468087418784845).

The candidate confirms that the work submitted is his own and that the appropriate credit has been given where reference has been made to the work of others. This copy has been supplied on the understanding that it is copyright material and that no quotation from this thesis may be published without proper acknowledgment. The right of Jamie Karl Smith to be identified as Author of this work has been asserted by him in accordance with the Copyright, Designs and Patents Act 1998.

# Acknowledgements

Firstly I would like to thank Professor Alexey Burluka for introducing me to the project and supervising me during the initial stages. Dr Daniel Ruprecht picked up the project where Alexey left off. Daniel's enthusiasm and encouragement throughout the project went a long way in helping me develop as a researcher, always keeping me on the right course. Dr. Malcolm Lawes also imparted some words of wisdom along the way.

Jaguar Land Rover must be acknowledged for providing me with a wonderful opportunity to work alongside industry. From JLR I would particularly like to thank Dave Richardson for his support over the entirety of the project. I must also thank Imperial College London who provided relevant experimental and CFD data through their connection with Jaguar Land Rover.

There are number of students within the combustion group during my time at Leeds, most of who have all contributed something to improving my daily working life. In no particular order I would like to acknowledge: Aaron, Ben, Jeong-Do, Moustafa, Ahmed and Luke. I would also like to extend my thanks to Tony who showed me the ropes with LUSIE and LUSIEDA when I first started. I would like to thank other friends such as Connor, Kiran, Maisie, my friends from home and my sister Chloe for keeping me sane and not letting me get ahead of myself over the course of my PhD.

A huge thank you must go to my parents Joanne and Karl for supporting me throughout everything. It is extremely difficult to convey in words how much I appreciate everything they have done for me, but I shall be forever grateful for what you have done. The financial burden on my parents during my time at University was made easier, allowing me to enjoy University without any financial worries and have some other great experiences, thanks to the money given to me by my grandparents Harold and Avril and my Auntie Sharon.

Last and by no means least I would like to thank my girlfriend Emily (I must be serious as I have used your full first name). She has been there from the very start of my undergraduate degree and is still somehow putting up with me even now. I am thankful for your support on a daily basis allowing me to be the best I can possibly be.

# Abstract

In a bid to meet the latest government regulations on pollution, and consumer demands, engine manufacturers are continually looking at new combustion strategies that consume less fuel, produce fewer emissions or improve engine thermal efficiency. The automotive industry are also looking to reduce production and design costs. Computational models save prototyping costs in drafting, manufacturing and assembly of parts, as well as eliminating the time taken to produce these prototypes.

One possible combustion strategy to meet these demands is fuel stratification where the fuel-air mixture is not perfectly mixed, leaving a fuel rich zone near the spark and a fuel lean zone near the cylinder walls. Combustion of a spatially and temporally varying equivalence ratio has been modelled using the Leeds University Spark Ignition Engine (LUSIE) quasi-dimensional thermodynamic code. The radially varying equivalence ratio was informed by distributions found within the literature. New sub-models that simulate the effect of burnt gas expansion and turbulent mixing on the initial equivalence ratio distribution have been integrated into the combustion code. The stratified fuel model was validated against experimental engine data, showing reasonable agreement for both the pressure trace and heat release profile. Further simulations investigated the effect of increasing stratification and centrally lean fuel with a rich zone near the walls. Qualitative trends from these studies agree with the literature, increasing model validity.

A second strategy to be employed is the recirculation of cooled exhaust gas (EGR) into the cylinder. Compared here is the accuracy of EGR correction factors under engine conditions. The effect of EGR on the laminar burning velocity has been determined from engine data using the Leeds University Spark Ignition Engine Data Analysis (LUSIEDA) reverse thermodynamic code. The engine data ranges from 5-25% EGR with the spark advance and intake pressure altered to maintain a constant engine load. A correlation is suggested for how the laminar burning velocity reduces with increasing EGR, based on experimental data. Existing correlations along with that found in this study were implemented into the predictive LUSIE with the resulting predictions compared against measurements. The correlation suggested here is in good agreement over the entire experimental range, providing the best fit to engine data under a number of running conditions when compared to models from the literature.

# Contents

---

|  |             |
|--|-------------|
| <b>List of Figures</b>   | <b>xv</b>   |
| <b>List of Tables</b>  | <b>xvi</b>  |
| <b>Nomenclature</b>  | <b>xvii</b> |
| <b>1 Introduction</b>  | <b>1</b>    |
| 1.1 Introduction . . . . .                                       | 1           |
| 1.2 Scope of the current work . . . . .                          | 2           |
| 1.2.1 Novel contributions . . . . .                              | 3           |
| 1.3 Thesis Outline . . . . .                                     | 3           |
| <b>2 Spark Ignition Engines</b>                                  | <b>5</b>    |
| 2.1 Overview . . . . .   | 5           |
| 2.2 Turbulence in SI engines . . . . .                           | 7           |
| 2.2.1 Turbulent velocity . . . . .                               | 8           |
| 2.2.2 Turbulent kinetic energy . . . . .                         | 10          |
| 2.2.3 Turbulent scales in engines . . . . .                      | 11          |
| 2.2.4 Turbulent bulk flow in engines: Swirl and Tumble . . . . . | 14          |
| 2.3 Combustion in SI engines . . . . .                           | 15          |
| 2.3.1 Laminar premixed flames . . . . .                          | 16          |
| 2.3.2 Turbulent premixed flames . . . . .                        | 22          |

---

|          |   |           |
|----------|---|-----------|
| 2.4      | Autoignition . . . . .                            | 27        |
| 2.5      | Cycle-to-cycle Variability . . . . .              | 27        |
| 2.6      | Stratified Charge Engines . . . . .               | 29        |
| 2.6.1    | Mixture formation . . . . .                       | 32        |
| 2.6.2    | Partially premixed combustion . . . . .           | 33        |
| 2.6.3    | Stratified charge modelling . . . . .             | 34        |
| 2.7      | Exhaust Gas Recirculation and Residuals . . . . . | 38        |
| 2.7.1    | Residuals . . . . .                               | 39        |
| 2.7.2    | Exhaust Gas Recirculation . . . . .               | 39        |
| <b>3</b> | <b>Combustion code</b>                            |           |
|          | <b>&amp; Engine Description</b>                   | <b>43</b> |
| 3.1      | Introduction . . . . .                            | 43        |
| 3.2      | LUSIE Simulation Software . . . . .               | 44        |
| 3.2.1    | Overview . . . . .                                | 44        |
| 3.2.2    | Model assumptions . . . . .                       | 45        |
| 3.2.3    | Zonal modelling . . . . .                         | 45        |
| 3.2.4    | Laminar burning velocity . . . . .                | 49        |
| 3.2.5    | Turbulent burning velocity . . . . .              | 52        |
| 3.2.6    | Turbulent flame acceleration . . . . .            | 55        |
| 3.2.7    | Flame-wall interaction . . . . .                  | 57        |
| 3.2.8    | Flame geometry . . . . .                          | 57        |
| 3.2.9    | Heat transfer . . . . .                           | 58        |
| 3.2.10   | Blow-by . . . . .                                 | 59        |
| 3.2.11   | Turbulence . . . . .                              | 60        |
| 3.3      | LUSIEDA Reverse Analysis . . . . .                | 61        |
| 3.4      | SI combustion code validation . . . . .           | 62        |
| 3.4.1    | Motoring cycle validation . . . . .               | 62        |

---

|          |   |            |
|----------|---|------------|
| 3.4.2    | Firing cycle validation . . . . .                     | 63         |
| 3.5      | Description of Engine . . . . .                       | 64         |
| <b>4</b> | <b>Exhaust Gas Recirculation in<br/>SI engines</b>    | <b>67</b>  |
| 4.1      | Chapter Overview . . . . .                            | 67         |
| 4.2      | Pre-existing correlations . . . . .                   | 67         |
| 4.3      | Engine data correlation . . . . .                     | 69         |
| 4.3.1    | Turbulent-laminar burning velocity relation . . . . . | 72         |
| 4.3.2    | Final correlation . . . . .                           | 75         |
| 4.4      | Predictive modelling . . . . .                        | 80         |
| 4.4.1    | 1500 rpm, 0.79 MPa GMEP . . . . .                     | 80         |
| 4.4.2    | 1500 rpm, 0.36 MPa GMEP . . . . .                     | 90         |
| 4.4.3    | 2000 rpm, 0.98 MPa GMEP . . . . .                     | 95         |
| 4.4.4    | Spark kernel delay time . . . . .                     | 99         |
| 4.5      | Chapter Summary . . . . .                             | 100        |
| <b>5</b> | <b>Stratified Fuel Model</b>                          | <b>102</b> |
| 5.1      | Chapter Overview . . . . .                            | 102        |
| 5.2      | Stratified charge . . . . .                           | 102        |
| 5.3      | Equivalence ratio distribution . . . . .              | 104        |
| 5.4      | Burned gas expansion . . . . .                        | 108        |
| 5.5      | Turbulent mixing . . . . .                            | 110        |
| 5.5.1    | Turbulent diffusivity . . . . .                       | 112        |
| 5.5.2    | Fuel injection timing . . . . .                       | 114        |
| 5.6      | Stratified model validation . . . . .                 | 115        |
| 5.7      | Predictive stratified modelling . . . . .             | 118        |
| 5.7.1    | Varying stratification level . . . . .                | 119        |

---

|          |   |            |
|----------|---|------------|
| 5.7.2    | Rich-lean and lean-rich stratification profiles . . . . . | 123        |
| 5.8      | Chapter Summary . . . . .                                 | 127        |
| <b>6</b> | <b>Conclusions and Reccomendations</b>                    | <b>131</b> |
| 6.1      | Introduction . . . . .                                    | 131        |
| 6.2      | Summary of EGR modelling conclusions . . . . .            | 132        |
| 6.3      | Summary of stratified fuel model conclusions . . . . .    | 133        |
| 6.4      | Reccomendations for future work . . . . .                 | 134        |
|          | <b>References</b>   | <b>136</b> |
| <b>A</b> | <b>Fuel specification</b>                                 | <b>155</b> |

# List of Figures

---

|     |  |    |
|-----|--|----|
| 2.1 | Indicating diagram for a Jaguar Land Rover Single Cylinder Research Engine at 2000 rpm and wide open throttle. With regards to valve timings the intake valve opened at $344^\circ$ bTDC and closed at $90^\circ$ bTDC with the exhaust valve opening at $134^\circ$ aTDC and closing at $347^\circ$ bTDC. . . . . | 7  |
| 2.2 | Reynolds decomposition for time-dependent flow, reproduced from Ling [2014]. . . . .   | 9  |
| 2.3 | Transversal and longitudinal spatial velocity correlations. The arrows represent the vector orientation of $u$ . . . . .   | 12 |
| 2.4 | Schematic of in-cylinder Swirl and Tumble. Reproduced from Wilson et al. [1993] . . . . .  | 14 |
| 2.5 | Concentration and temperature profiles for the mechanism of flame propagation. Taken from Conway [2013] where it was adapted from Griffiths et al. [1995]. . . . .   | 16 |
| 2.6 | Schlieren image of a cellular iso-octane/air mixture at 360 K and 0.5 MPa, taken from Mumby [2016]. . . . .  | 18 |
| 2.7 | Variation of laminar flame speed with flame stretch for iso-octane/air mixtures at 360 K and 1.0 MPa, taken from Mumby [2016]. . . . .   | 19 |
| 2.8 | Variation of $u_n$ and $u_{nr}$ with stretch rate for iso-octane-air mixtures. Taken from Gillespie et al. [2000]. . . . .   | 20 |
| 2.9 | Laminar burning velocity for iso-octane and 90 RON (90% iso-octane, 10% n-heptane mixture) at varying equivalence ratios at 358 K and 0.1 MPa, taken from Bradley et al. [1998]. . . . .   | 21 |

---

|      |   |    |
|------|---|----|
| 2.10 | Radii definitions that are traditionally attributed to turbulent pre-mixed flames, modified from Conway [2013]. . . . .   | 22 |
| 2.11 | DNS simulations showing how turbulent burning velocity diminishes at high turbulence intensity, taken from Nivarti and Cant [2017]. . . . .   | 24 |
| 2.12 | A Borghi diagram containing information on turbulent combustion regimes. . . . .  | 25 |
| 2.13 | General engine operating map for a GDI engine. Recreation based on engine map found in Horie et al. [2004]. . . . .   | 30 |
| 2.14 | Categories of stratified charge engines, taken from Fansler et al. [2015] where it was reproduced from Zhao et al. [1999]. . . . .  | 32 |
| 2.15 | In-cylinder pressure curves computed by neglecting turbulent fluctuations in mixture fraction (solid lines) and by invoking the mass-weighted (dashed lines) and canonical (dotted-dashed lines) beta-PDFs for the mixture fraction, taken from Huang et al. [2014a]. . . . . | 36 |
| 2.16 | Schematic of a low pressure EGR loop for a turbo-charged four cylinder engine, taken from Gukelberger et al. [2015]. . . . .  | 40 |
| 3.1  | Two and Three-zone models including definitions used within LUSIE   | 46 |
| 3.2  | Wiebe function of the cumulative mass fraction burned for different values of $a$ and $m$ . . . . .   | 47 |
| 3.3  | Comparison of laminar burning velocity models at varying equivalence ratio at pressure 5 bar and temperature 360 K. . . . .   | 49 |
| 3.4  | Comparison of laminar burning velocity models at varying equivalence ratio at pressure 35 bar and temperature 600 K. . . . .  | 50 |
| 3.5  | Laminar burning velocity for TRF gasoline surrogate with added ethanol at various pressures and $T_u = 360\text{K}$ . Data taken from Mumby [2016]. . . . .   | 51 |
| 3.6  | U/K diagram with Zimont-Lipatnikov model plotted. . . . .   | 54 |
| 3.7  | LUSIE pressure trace simulations for APF model developed by Abdi Aghdam [2003] and error function model proposed by Lipatnikov and Chomiak [2000], under arbitrary running conditions. . . . .  | 58 |

|      |   |    |
|------|---|----|
| 3.8  | Visual output of GGEOM showing the Jaguar Land Rover single cylinder research engine geometry and flame radius for a given crank angle. . . . .   | 59 |
| 3.9  | Crank resolved turbulent RMS velocity and integral length scale generated using CFD . . . . .   | 61 |
| 3.10 | LUSIE simulated motoring pressure trace compared to experimental firing cycle. . . . .  | 63 |
| 3.11 | LUSIE simulated crank-resolved pressure trace with tuned constants and experimental data at 1500 rpm and GMEP of 0.79 MPa. . . . .  | 64 |
| 3.12 | Jaguar Land Rover test engine. . . . .  | 65 |
| 4.1  | External EGR, post exhaust residual gas and total in-cylinder residuals for each case described in Table 4.2. . . . .   | 70 |
| 4.2  | Flowchart describing process of obtaining EGR correction factor from engine pressure trace data. . . . .  | 71 |
| 4.3  | Correction factor resulting when considering data from different numbers of cycles. The average difference between the results is 1.5%. . .   | 72 |
| 4.4  | Correction factor resulting from sensitivity analysis of $C_{ut}$ ( $C_{ut}=0.33$ ). The maximum difference over all points is 1.5%. . . . .  | 75 |
| 4.5  | Back calculated laminar burning velocity plotted against the change in in-cylinder pressure (symbols) and curve fitting of $u_l$ (lines). . . . .   | 76 |
| 4.6  | EGR correction factor plotted against the change in in-cylinder pressure for increasing levels of EGR. . . . .  | 77 |
| 4.7  | Turbulent mass burning velocity plotted against burned gas radius for increasing levels of EGR. . . . .   | 78 |
| 4.8  | EGR correction factor plotted against mass fraction of residuals. The plot compares results from the present study to correction factors found within the literature. . . . .   | 79 |
| 4.9  | Predicted engine pressure traces comparing the correlation found in the present study to models found in the literature, at 5% EGR. Experimental data is comprised of 36 fast, 77 middle and 47 slow combustion cycles. . . . . | 81 |

---

|      |  |    |
|------|--|----|
| 4.10 | Predicted engine pressure traces comparing the correlation found in the present study to models found in the literature, at 10% EGR. Experimental data is comprised of 41 fast, 51 middle and 45 slow combustion cycles. . . . . | 82 |
| 4.11 | Predicted engine pressure traces comparing the correlation found in the present study to models found in the literature, at 15% EGR. Experimental data is comprised of 37 fast, 63 middle and 41 slow combustion cycles. . . . . | 83 |
| 4.12 | Predicted engine pressure traces comparing the correlation found in the present study to models found in the literature, at 20% EGR. Experimental data is comprised of 46 fast, 63 middle and 44 slow combustion cycles. . . . . | 84 |
| 4.13 | Predicted engine pressure traces comparing the correlation found in the present study to models found in the literature, at 25% EGR. Experimental data is comprised of 44 fast, 65 middle and 44 slow combustion cycles. . . . . | 85 |
| 4.14 | RMS error against measured pressure trace for varying levels of EGR for simulations at 1500 rpm and GMEP of 0.79 MPa. . . . .  | 85 |
| 4.15 | Predicted mass fraction burned comparing the correlation found in the present study to models found in the literature, at 5% EGR. . . .  | 86 |
| 4.16 | Predicted mass fraction burned comparing the correlation found in the present study and in the literature to experimental data, at 10% EGR. . . . .  | 86 |
| 4.17 | Predicted mass fraction burned comparing the correlation found in the present study to models found in the literature, at 15% EGR. . . .   | 87 |
| 4.18 | Predicted mass fraction burned comparing the correlation found in the present study to models found in the literature, at 20% EGR. . . .   | 87 |
| 4.19 | Predicted mass fraction comparing the correlation found in the present study to models found in the literature, at 25% EGR. . . . .  | 88 |
| 4.20 | RMS error for predicted mass fraction burned for varying levels of EGR for simulations at 1500 rpm and GMEP of 0.79 MPa. . . . .   | 88 |
| 4.21 | RMS error for predicted mass fraction burned for varying levels of EGR for simulations at 1500 rpm and GMEP of 0.79 MPa showing the three best performing models only. . . . .   | 89 |

---

|      |  |    |
|------|--|----|
| 4.22 | LUSIE simulated crank-resolved pressure trace with tuned constants and experimental data at 1500 rpm and GMEP of 0.36 MPa. Experimental data is comprised of 31 fast, 66 middle and 46 slow combustion cycles. . . . .   | 90 |
| 4.23 | Simulated crank-resolved pressure trace comparing the correlation determined in the present study and models from the literature to experimental data at 5% EGR, 1500 rpm and GMEP of 0.36 MPa. Experimental data is comprised of 42 fast, 46 middle and 51 slow combustion cycles. . . . .  | 91 |
| 4.24 | Simulated crank-resolved pressure trace comparing the correlation determined in the present study and models from the literature to experimental data at 10% EGR, 1500 rpm and GMEP of 0.36 MPa. Experimental data is comprised of 44 fast, 65 middle and 39 slow combustion cycles. . . . . | 92 |
| 4.25 | Simulated crank-resolved pressure trace comparing the correlation determined in the present study and models from the literature to experimental data at 15% EGR, 1500 rpm and GMEP of 0.36 MPa. Experimental data is comprised of 42 fast, 74 middle and 39 slow combustion cycles. . . . . | 93 |
| 4.26 | Simulated crank-resolved pressure trace comparing the correlation determined in the present study and models from the literature to experimental data at 20% EGR, 1500 rpm and GMEP of 0.36 MPa. Experimental data is comprised of 44 fast, 64 middle and 48 slow combustion cycles. . . . . | 93 |
| 4.27 | RMS error against measured pressure trace for varying levels of EGR for simulations at 1500 rpm and GMEP of 0.36 MPa. . . . .  | 94 |
| 4.28 | LUSIE simulated crank-resolved pressure trace with tuned constants and experimental data at 2000 rpm and GMEP of 0.98 MPa. Experimental data is comprised of 44 fast, 55 middle and 48 slow combustion cycles. . . . .   | 95 |
| 4.29 | Simulated crank-resolved pressure trace comparing the correlation determined in the present study and models from the literature to experimental data at 5% EGR, 2000 rpm and GMEP of 0.98 MPa. Experimental data is comprised of 41 fast, 67 middle and 46 slow combustion cycles. . . . .  | 96 |

---

|      |  |     |
|------|--|-----|
| 4.30 | Simulated crank-resolved pressure trace comparing the correlation determined in the present study and models from the literature to experimental data at 10% EGR, 2000 rpm and GMEP of 0.98 MPa. Experimental data is comprised of 41 fast, 60 middle and 45 slow combustion cycles. . . . . | 97  |
| 4.31 | Simulated crank-resolved pressure trace comparing the correlation determined in the present study and models from the literature to experimental data at 15% EGR, 2000 rpm and GMEP of 0.98 MPa. Experimental data is comprised of 39 fast, 71 middle and 46 slow combustion cycles. . . . . | 97  |
| 4.32 | Simulated crank-resolved pressure trace comparing the correlation determined in the present study and models from the literature to experimental data at 20% EGR, 2000 rpm and GMEP of 0.98 MPa. Experimental data is comprised of 48 fast, 54 middle and 49 slow combustion cycles. . . . . | 98  |
| 4.33 | RMS errors for simulated pressure traces with respect to experimental mean cycle at 2000 rpm and GMEP of 0.98 MPa. . . . .   | 98  |
| 4.34 | Spark kernel delay time at increasing mass fractions of EGR for three engine speed/load conditions. . . . .  | 99  |
| 5.1  | (a) Equivalence ratio profile taken from (a)Shi et al. [2016] (b) Pires Da Cruz et al. [2000] (c) Moriyoshi et al. [1996]. . . . .   | 105 |
| 5.2  | Data points taken from Moriyoshi et al. [2003] with fitted function. . . . .   | 106 |
| 5.3  | Graphical representation of adapted three-zone model for stratified case. . . . .  | 107 |
| 5.4  | Unburned and burned zones before and after the burned gas expansion. Reproduced from Abdi Aghdam [2003]. . . . .   | 109 |
| 5.5  | Infinitesimal elective annular element in the unburned zone before and after the burned gas expansion. Reproduced from Abdi Aghdam [2003]. . . . .   | 110 |
| 5.6  | Initial equivalence ratio distributions ( $t=0$ ) for experimentally fitted Fermi function (Eq. (5.6)), with $dr = 20$ and $r_0 = 5$ and turbulent mixing model (Eq. (5.19)). . . . .  | 112 |

---

|      |  |     |
|------|--|-----|
| 5.7  | Equivalence ratio distributions calculated by LUSIE for turbulent mixing with and without burned gas expansion. . . . .  | 114 |
| 5.8  | LUSIE simulated crank-resolved pressure trace, mean experimental cycle and 95% confidence interval at 1500 rpm and GMEP of 0.36 MPa.   | 117 |
| 5.9  | LUSIE simulated crank-resolved pressure trace, mean experimental cycle and 95% confidence interval for the stratified case at 1500 rpm and GMEP of 0.36 MPa. . . . .               | 118 |
| 5.10 | Percentage heat release for the simulated and experimental case under stratified conditions at 1500 rpm and GMEP of 0.36 MPa. . . . .  | 119 |
| 5.11 | Radially varying initial ( $t=0$ ) equivalence ratio for cases 1-8. . . . .  | 120 |
| 5.12 | Crank resolved in-cylinder pressure profiles for increasing stratification at 1500 rpm. . . . .  | 121 |
| 5.13 | Comparison of pressure profiles for case 8 (used for stratified model validation) with case 3 at 1500 rpm. . . . .   | 122 |
| 5.14 | Crank resolved mass fraction burned profiles for increasing stratification at 1500 rpm. . . . .  | 123 |
| 5.15 | Maximum burned gas temperature for increasing stratification levels at 1500 rpm. . . . .   | 124 |
| 5.16 | Mean laminar burning velocity for increasing stratification at 1500 rpm.   | 124 |
| 5.17 | Mean turbulent entrainment velocity for increasing stratification at 1500 rpm. . . . .   | 125 |
| 5.18 | Crank resolved equivalence ratios for cases 1-8 with optimal equivalence ratios residing in the highlighted section. . . . .   | 126 |
| 5.19 | Two equivalence ratio profiles with same minima and maxima for rich-lean and lean-rich stratification profiles. . . . .  | 127 |
| 5.20 | Crank resolved pressure trace for rich-lean and lean-rich stratification profiles at high and low levels of stratification. . . . .  | 128 |
| 5.21 | Rate of change of pressure w.r.t crank angle for rich-lean and lean-rich stratification profiles at high and low levels of stratification. . . . .                                 | 129 |
| 5.22 | Rate of change of pressure w.r.t time for (a) a centrally rich stratification pattern and (b) a centrally lean stratification pattern. Taken from Fujimoto et al. [1995] . . . . . | 130 |

|  |     |
|--|-----|
| 5.23 Crank resolved mass fraction burned for rich-lean and lean-rich stratification profiles at high and low levels of stratification. . . . . | 130 |
|--|-----|

# List of Tables

---

|     |  |     |
|-----|--|-----|
| 2.1 | Turbulence constant, $F_\lambda$ to determine Taylor length scale from integral length scale. . . . .                                | 13  |
| 3.1 | Coefficients for Rhodes and Keck [1985] laminar burning velocity model.  | 51  |
| 3.2 | Running conditions for LUSIE validation. . . . .   | 62  |
| 3.3 | Jaguar Land Rover SCRE specification . . . . .   | 64  |
| 4.1 | Summary of EGR correction factor correlations. . . . .   | 69  |
| 4.2 | Experimental running conditions for increasing levels of EGR to maintain a constant engine load of 0.79 MPa GMEP at 1500rpm. . . . . | 70  |
| 5.1 | Exhaust gas data at 1500rpm and 0.36 MPa GMEP . . . . .  | 115 |
| 5.2 | Running conditions for homogenous and stratified experimental data. .  | 116 |
| 5.3 | Cases for varying stratification . . . . .   | 120 |

# Nomenclature

---

## Roman & Greek Symbols

| Symbol       | Units                          | Description                            |
|--------------|--------------------------------|--|
| A            | m <sup>2</sup>                 | Area                                   |
| $C_{\tau_b}$ | -                              | Characteristic burn-up time constant   |
| $C_{ut}$     | -                              | Zimont burning velocity model constant |
| $\delta_l$   | m                              | Laminar flame thickness                |
| $\delta_t$   | m                              | Turbulent flame thickness              |
| Da           | -                              | Damköhler number                       |
| $f_d$        | -                              | Flame development factor               |
| $f_{rb}$     | m                              | Radius of burned gas                   |
| $f_{re}$     | m                              | Radius of entrained gas                |
| K            | -                              | Karlovitz number                       |
| k            | m <sup>2</sup> /s <sup>2</sup> | Turbulent kinetic energy               |
| Le           | -                              | Lewis number                           |
| L            | m                              | Turbulent integral length scale        |
| $\lambda$    | m                              | Turbulent Taylor length scale          |
| $\eta$       | m                              | Turbulent Kolmogorov length scale      |
| m            | kg                             | Mass                                   |
| $\dot{m}$    | kg/s                           | Mass flow rate                         |
| P            | Pa                             | Pressure                               |
| $\phi$       | -                              | Fuel-air equivalence ratio             |
| $\rho$       | kg/m <sup>3</sup>              | Density                                |
| r            | m                              | Radius                                 |
| Re           | -                              | Reynolds number                        |
| T            | K                              | Temperature                            |
| t            | s                              | Time                                   |
| $u'$         | m/s                            | Turbulent RMS velocity                 |
| $u'_k$       | m/s                            | Effective turbulent RMS velocity       |
| $u_l$        | m/s                            | Laminar burning velocity               |
| $u_t$        | m/s                            | Turbulent burning velocity             |
| $\nu$        | m <sup>2</sup> /s              | Kinematic viscosity                    |
| V            | m <sup>3</sup>                 | Volume                                 |

## Abbreviations

|         |   |
|---------|---|
| aTDC    | After top dead centre                                       |
| BDC     | Bottom dead centre  |
| bTDC    | Before top dead centre                                      |
| BMEP    | Brake mean effective pressure                               |
| BSFC    | Brake specific fuel consumption                             |
| CAI     | Controlled auto-ignition                                    |
| CFD     | Computational fluid dynamics                                |
| COV     | Coefficient of variability                                  |
| DI      | Direct injection  |
| EGR     | Exhaust gas recirculation                                   |
| GDI     | Gasoline direct injection                                   |
| GMEP    | Gross mean effective pressure                               |
| ICE     | Internal combustion engine                                  |
| IMEP    | Indicated mean effective pressure                           |
| LUSIE   | Leeds university spark ignition engine (code)               |
| LUSIEDA | Leeds university spark ignition engine data analysis (code) |
| MBT     | Maximum brake torque  |
| PDF     | Probability density function                                |
| RANS    | Reynolds averaged Navier Stokes                             |
| RMS     | Root mean squared   |
| SC      | Stratified charge   |
| SCRE    | Single cylinder research engine                             |
| SI      | Spark Ignition  |
| TDC     | Top dead centre   |

# Chapter 1

## Introduction

---

### 1.1 Introduction

Spark ignition engines are extremely versatile and are used in numerous applications, from two-stroke engines in scooters, motorbikes (older models) and lawnmowers, to four-stroke engines in cars and light aircraft. The number of vehicles on the road is continuously growing with the total licensed vehicles on the road in the UK increasing by an average of 650,000 a year between 2012 and 2015 (Department for Transport [2016]). Coupled with the decrease in the availability and sustainability of fossil fuels, government legislation on controlling emissions is becoming ever more stringent.

Computational modelling looks a promising technique in the development of Internal Combustion Engines (ICEs) allowing for a reduction in the number of prototypes manufactured, thus lowering cost. Two common methods of numerical engine modelling are: Computational Fluid Dynamics (CFD) and Thermodynamic quasi-dimensional modelling. CFD solves fluid dynamic equations and can resolve engine processes in 3-D. The thermodynamic code solves thermodynamic relations and utilises burning velocity correlations to compute combustion. The thermodynamic model typically resolves the flame radius at a given time step but does not fully resolve in 3-D. While the spatial resolution is reduced for the quasi-dimensional model the computational power needed is greatly reduced with typical computation times measured in seconds and minutes as opposed to hours, days or even weeks for the CFD case.

The latest European regulations (EURO VI) came into effect in 2014, with the

primary focus to reduce nitrogen oxide (NO<sub>x</sub>) emissions, albeit in Diesel engines. While NO<sub>x</sub> limits may not have changed from EURO V to EURO VI for gasoline engines, NO<sub>x</sub> emissions still remain a hurdle when looking to improve thermal efficiency of the engine and prevent the use of a lean-burn strategy. The introduction of cooled exhaust gas into the combustion chamber has proven to be an effective strategy in NO<sub>x</sub> reduction (Takaki et al. [2014], Kumano and Yamaoka [2014], Alger et al. [2011]) while increasing the ratio of specific heats and thus thermal efficiency of the engine. The cooled EGR leads to a reduction in the laminar burning velocity. For computer simulations of combustion engines the EGR is modelled using a correction factor that reduces the laminar burning velocity with increasing EGR. Multiple examples of these correction factors exist however none have been derived directly from an engine. Currently, to the best of the author's knowledge, no work exists that compares these models in terms of their accuracy under engine conditions. Therefore, it is not clear which models are useful to simulate the effect of EGR on combustion in SI engines or whether any of them are predictive at all.

Another promising engine strategy at low speeds and low loads is to operate with a stratified charge as opposed to the 'traditional' homogeneous charge. Benefits of utilising a stratified charge include reduced pumping losses due to unthrottled part-load operation, decreased heat loss to cylinder walls and an increase in compression ratio due to lower end gas temperatures associated with stratified combustion (Zhao et al. [1999]).

## 1.2 Scope of the current work

The scope of the current work was to develop new simulation techniques to model EGR and stratified combustion and then integrate these models into a quasi-dimensional thermodynamic predictive code known as the Leeds University Spark Ignition Engine (LUSIE) code to predict the modern combustion strategies introduced in section 1.1. The pre-existing homogeneous combustion code, which has been validated numerous times under these conditions, is extended to now predict the entire engine map. This includes additional sub-models to account for the stratified mode of operation and an updated correlation for the effect of EGR on SI engine combustion. The performance of these models is typically evaluated for the in-cylinder pressure data, and mass fraction burned profile. Finally conclusions are drawn from the research and provide a direction for future work.

### 1.2.1 Novel contributions

The most important novel aspects of this work can be identified as:

- Conception of a method to determine the EGR correction factor, which is associated with the laminar burning velocity, using engine pressure trace data and a reverse thermodynamic code. The correlation found is, to the author's knowledge, the only case derived directly from engine data.
- Identifying which EGR correction factors from the literature are capable of predicting accurate engine pressure trace data (if any) at various engine speed/load conditions with EGR rates from 5-25% compared.
- Derivation of the model constant  $C_{ut}$  for the Zimont-Lipatnikov turbulent burning velocity model using the U/K turbulent burning velocity correlation
- Validation of a quasi-dimensional fuel model against experimental engine data. The model includes a burned gas expansion for a spherically propagating flame and turbulent mixing model simulating the temporal change in an initial equivalence ratio distribution.

## 1.3 Thesis Outline

- Chapter 2 - In this chapter an extended review into turbulence, combustion and two engine strategies of interest is undertaken. Statements made on these topics have been supported by peer-reviewed publications. Work has been critically reviewed and any issues with studies from the literature are highlighted. The engine strategies of interest are the stratified charge operating mode and the effects on combustion when introducing cool recirculated exhaust gas into the cylinder. These strategies, being the focus of the work presented here, are discussed in depth.
- Chapter 3 - The predictive SI engine combustion code and the reverse thermodynamic analysis code are introduced and described in detail. The chapter includes a description of the quasi-dimensional zonal models, turbulent and laminar burning velocity sub-models, heat-transfer and blow-by. The inclusion of turbulence into a quasi-dimensional model is discussed. The single-cylinder research engine used to carry out experimental work for model validation purposes is also introduced.

- Chapter 4 - The focus of this chapter is the effect of exhaust gas recirculation on SI engine combustion. The chapter describes the novel method of determining an EGR correction factor to the laminar burning velocity from engine data. The correlation from engine data is then compared to correlations found in the literature. These correlations are compared to experimental pressure data under a number of engine speed/load conditions to determine the predictability of each model.
- Chapter 5 - A quasi-dimensional thermodynamic model is extended to include the stratified charge operating range. The stratified charge model is incorporated through the use of a radially varying equivalence ratio. The effect of burned gas expansion and turbulent mixing alter the profile in time. The quasi-dimensional model is validated against experimental engine data for the pressure trace and heat release. A parametric study into changing the equivalence ratio profile is also described.
- Chapter 6 - Important conclusions drawn from the investigations into EGR correction factors (Chapter 4) and stratified fuel modelling (Chapter 5) are stated in this chapter. Suggestions for future work to improve the combustion codes, as well as further general combustion research are put forward.

# Chapter 2

## Spark Ignition Engines

---

### 2.1 Overview

Spark ignition (SI) engines use a spark, that is generated using a spark plug, to ignite the unburned mixture in the engine, converting the chemical energy of the fuel into useful work through an exothermic reaction known as combustion. The reciprocating piston engine is the dominant SI engine design and is the focus of the work presented in this thesis.

The reciprocating piston engine can use a four stroke cycle, where each engine cycle comprises of:

- **Intake** - Air is inducted into the cylinder through intake valves as the piston moves from top dead centre (TDC), where the cylinder volume is at its minimum, to bottom dead centre (BDC), where the cylinder volume is at its maximum. The induction of fresh gas creates in-cylinder turbulence motion.
- **Compression** - The compression stroke starts when both valves are closed and the cylinder is compressed to a small fraction of its total volume. The in-cylinder volume decrease leads to an increase of in-cylinder pressure. When the compression stroke approaches TDC combustion is initiated and the in-cylinder pressure increases more rapidly.
- **Expansion** - The expansion stroke starts at TDC, where the high pressure and high temperature gas pushes the piston down forcing the crank to rotate. As the piston approaches BDC the exhaust valve is opened.
- **Exhaust** - The exhaust stroke starts at BDC and moves to TDC. The increase

of in-cylinder pressure forces mass to flow through the open exhaust valve into the low pressure exhaust manifold. As the piston approaches TDC the cycle restarts.

This study focuses on the closed part of the engine cycle, neglecting to model the intricate intake and exhaust processes, which are accounted for when setting initial boundary conditions. The thermodynamic effects of isentropic compression/expansion of a gas within the engine can be simply calculated from the first law of thermodynamics, for a perfect gas, by (Adkins [1987]):

$$PV^\gamma = \text{Constant} \quad (2.1a)$$

$$TV^{\gamma-1} = \text{Constant} \quad (2.1b)$$

where  $P$  is pressure,  $V$  is volume,  $T$  is temperature and  $\gamma$  is the specific heat at constant pressure,  $c_P$ , divided by the specific heat at constant volume,  $c_V$ .

$$\gamma = \frac{c_P}{c_V} \quad (2.2)$$

While the ideal gas law breaks down at high pressures, any possible invalidity in assuming an ideal gas under engine conditions is countered by the high temperatures associated with combustion (Verhelst and Sheppard [2009]).

The indicating diagram describes the change in in-cylinder pressure w.r.t volume, from which the Gross Mean Effective Pressure (GMEP) can be calculated by:

$$\int_{-180^\circ}^{180^\circ} \frac{P \, dV}{V_d} \quad (2.3)$$

where  $V_d$  is the displaced volume. An indicating diagram for 300 firing cycles is shown in Figure 2.1, where the sharp increase in pressure in the indicating diagram is due to heat release from combustion, with the steady pressure rise/decline due to compression/expansion effects of the gas respectively. It is therefore the combustion process that is the defining performance parameter of any spark ignition internal combustion engine (ICE).

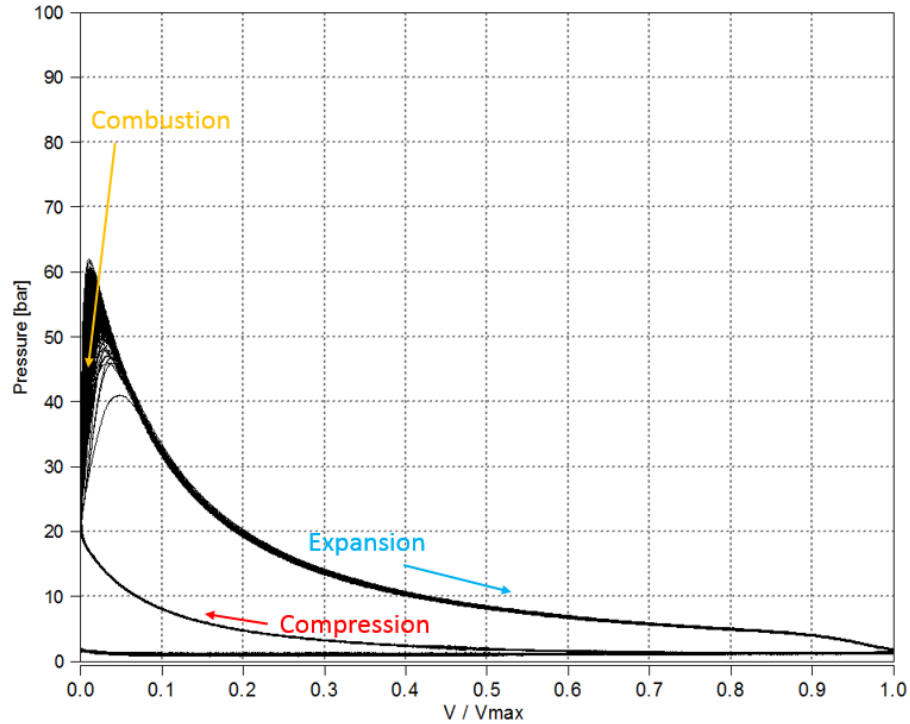


Figure 2.1: Indicating diagram for a Jaguar Land Rover Single Cylinder Research Engine at 2000 rpm and wide open throttle. With regards to valve timings the intake valve opened at  $344^\circ$  bTDC and closed at  $90^\circ$  bTDC with the exhaust valve opening at  $134^\circ$  aTDC and closing at  $347^\circ$  bTDC.

## 2.2 Turbulence in SI engines

Turbulent motion in a fluid flow was defined by Bradshaw [1971] as:

*“Turbulence is a three dimensional time dependent motion in which vortex stretching causes velocity fluctuations to spread to all wavelengths between a maximum determined by the boundary conditions of the flow and minimum determined by viscous forces. It is the usual state of fluid motion except at low Reynolds numbers”.*

The Reynolds number is a dimensionless quantity which compares inertial to viscous forces:

$$\text{Re} = \frac{u'L}{\nu} \quad (2.4)$$

where  $u'$  is the turbulent root mean squared (RMS) velocity,  $L$  is the integral length scale of turbulence and  $\nu$  is the kinematic viscosity. A high Reynolds number indicates that a flow is turbulent, whereas a low Reynolds number indicates a laminar flow. The majority of the in-cylinder turbulence found in an SI engine comes from the intake flow (Tabaczynski [1976]). Knowledge of turbulence is required to understand the concepts of turbulent combustion that occurs within reciprocating internal combustion engines.

Turbulence can be described as homogeneous when the mean properties of the flow are spatially uniform and are statistically equivalent to measures taken at other positions. Isotropic turbulence is where the flow has no preferential direction. This means that measurements taken using from one probe orientation are statistically the same when taken from another orientation. Due to the stochastic nature of turbulence, statistical analysis is required to describe the complexity of turbulence problems.

This section outlines turbulence parameters that are important for turbulent combustion such as turbulence velocity and length scales. It also introduces the bulk motions that occur within engines and why these bulk flows offer various advantages to engine designers.

### 2.2.1 Turbulent velocity

The turbulent velocity can be thought of as a mean flow velocity and an instantaneous statistically varying turbulent velocity. The two are related via the Reynolds decomposition (Heywood [1988]):

$$U(t) = \bar{U}(t) + u(t) \quad (2.5)$$

For a steady flow,  $\bar{U}$  is time independent and can be described by:

$$\bar{U} = \lim_{\tau \rightarrow \infty} \frac{1}{\tau} \int_{t_0}^{t_0+\tau} U dt \quad (2.6)$$

The fluctuating velocity,  $u$ , is defined by a Root Mean Squared (RMS) value:

$$u' = \lim_{\tau \rightarrow \infty} \left[ \frac{1}{\tau} \int_{t_0}^{t_0+\tau} (U^2 - \bar{U}^2) dt \right]^{\frac{1}{2}} \quad (2.7)$$

The “turbulence intensity” is defined as  $u'/\bar{U}$ , however for cases in which the mean

flow velocity is zero it is typical for the turbulence intensity to be simply given by  $u'$ . Essentially  $u'$  can be thought of as the standard deviation of the fluctuations around the mean. The Reynolds decomposition of a Eulerian turbulent velocity measurement is shown schematically in Figure 2.2.

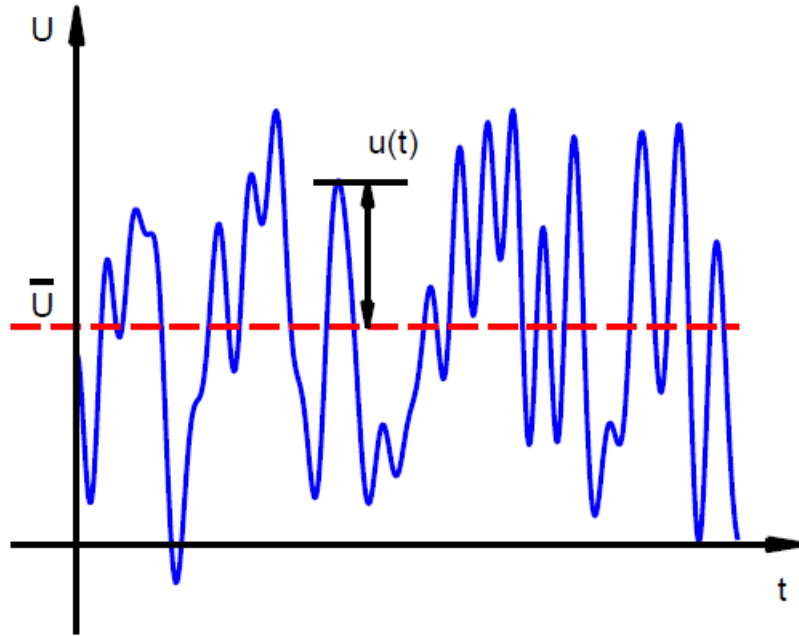


Figure 2.2: Reynolds decomposition for time-dependent flow, reproduced from Ling [2014].

In an engine the turbulence velocity is dependent upon the crank angle and the cycle number and is a measure of the turbulent velocity at some point in the combustion chamber. Eq. (2.5) is modified to correspond to the Reynolds decomposition found within an internal combustion engine (ICE):

$$U(\theta, i) = \bar{U}(\theta) + u(\theta, i) \quad (2.8)$$

where  $\theta$  is the crank angle and  $i$  is the cycle number. Large scale flow structures have been found to be present for each cycle. The ensemble average mean velocity,  $\bar{U}_{EA}$ , represents the “bulk” flow present in the combustion chamber and is calculated by:

$$\bar{U}_{EA} = \frac{1}{N} \sum_{i=1}^N U(\theta, i) \quad (2.9)$$

where  $N$  is the number of cycles used in the averaging. Hussin [2012] investigated the number of cycles required to determine a  $u'$  value, where it was concluded that  $N \geq \text{Engine speed (rpm)}/7.5$  gives a good statistical sample.

### 2.2.2 Turbulent kinetic energy

The specific turbulent kinetic energy,  $k$ , is another important parameter when studying turbulence. For a 3-D flow field the turbulent kinetic energy can be expressed as:

$$k = \frac{1}{2}(u_x'^2 + u_y'^2 + u_z'^2) \quad (2.10)$$

For the case of isotropic turbulence, which is often assumed for engines, the turbulent kinetic energy is reduced to:

$$k = \frac{3}{2}u'^2 \quad (2.11)$$

Conway [2013], who looked to implement a 0-D  $k$ - $\varepsilon$  model into LUSIE, where  $\varepsilon$  is the kinetic energy dissipation, states that from a modelling perspective it is the turbulent kinetic energy that is predicted before being converted into turbulent RMS velocity:

$$u' = \sqrt{\frac{2}{3}k} \quad (2.12)$$

The in-cylinder turbulence is largely driven by the intake of air through the inlet valve. Once the inlet valve is closed the turbulent kinetic energy starts to dissipate due to the lack of driving force<sup>1</sup> (Tennekes and Lumley [1972]). The dissipation of turbulent kinetic energy is given by:

$$\varepsilon = u'^3/L. \quad (2.13)$$

Three key implications of Eq. (2.13) are:

- The dissipation rate is controlled by the largest eddy scales only
- The rate of dissipation is independent of viscosity
- The rate of dissipation is proportional to the kinetic energy,  $k$ .

Although a 0-D model has been incorporated into LUSIE, the  $k$ - $\varepsilon$  (and some variations upon the original) is a common technique used for engine turbulence modelling using 3-D CFD (Payri et al. [2004], Rakopoulos et al. [2010], Roberts et al. [2018]). The 0-D case has recently been extended in the study by Bozza et al.

---

<sup>1</sup>While the turbulence does generally dissipate throughout the cycle it is not unusual to see an increase in turbulent kinetic energy as the cylinder approaches TDC, due to piston motion.

[2018a] and Bozza et al. [2018b] in an aim to account for the turbulent bulk motion of tumble (see section 2.2.4) within the cylinder.

### 2.2.3 Turbulent scales in engines

Three scales are typically used to characterise the size of the eddies in turbulent flow: the integral length scale,  $L$ , the Taylor scale,  $\lambda$  and the Kolmogorov scale,  $\eta$ . The scales have no precise numbers to define them as the scales can vary hugely depending on the application, instead they characterise orders of magnitude. The length scale of turbulence can be thought of as the diameter of a given eddy.

The largest eddy length/time scale, also known as the integral scale, can be derived using an autocorrelation function. The concept of autocorrelation is based on taking the product of  $\overline{u(x)u(x+r)}$  at increasing values of  $r$ . If the product remains almost constant as  $r$  is increased then  $u$  is said to correlate well with itself. The distance over which  $u$  correlates well with itself is then a measure of the largest eddies in the flow field. Typically a normalised autocorrelation function is used:

$$R(r) = \frac{\overline{u(x)u(x+r)}}{u^2} \quad (2.14)$$

The area under an autocorrelation function  $R(r)$  gives an indication of the characteristic size of the energy containing eddies within a flow (Tennekes and Lumley [1972]). This is known as the integral scale.

$$L = \int_0^\infty R(r) dr \quad (2.15)$$

The normalised autocorrelation function may be either longitudinal or transverse depending upon the vector orientation of  $u$  and  $r$ . This difference is presented in Figure 2.3.

The longitudinal and transverse integral length scales, for homogeneous and isotropic flow, are related by (Hinze [1959]):

$$L_L = 2L_T \quad (2.16)$$

The autocorrelation function can also be expressed temporally, where the turbulent velocity is measured at two points in time:

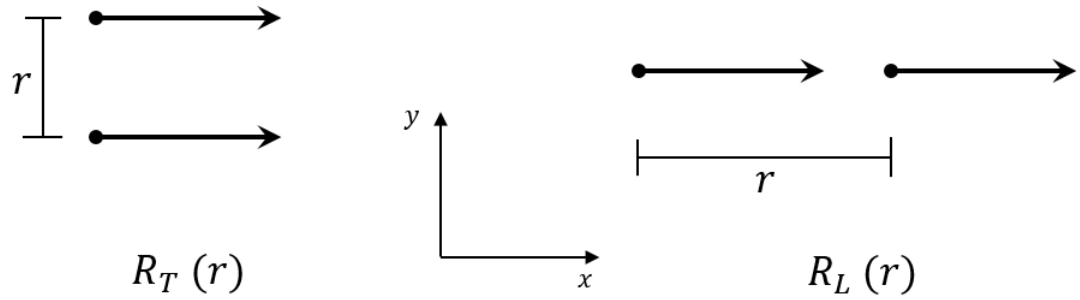


Figure 2.3: Transversal and longitudinal spatial velocity correlations. The arrows represent the vector orientation of  $u$ .

$$R(t) = \frac{\overline{u(t_0)u(t_0 + t)}}{u'^2} \quad (2.17)$$

where  $t_0$  is the initial point in time. From this the integral time scale,  $\tau_L$  can be calculated:

$$\tau_L = \int_{t=0}^{t=\infty} R(t) dt \quad (2.18)$$

The integral length scale can therefore be related to the integral time scale by:

$$L = u' \tau_L \quad (2.19)$$

The Kolmogorov length scale is that of the smallest dissipative eddies. The energy of the small scale eddies is dissipated due to the viscosity of the fluid. Kolmogorov theory is based upon two hypotheses of similarity [Kolmogorov [1991b,a]]. The first hypothesis of similarity states that in locally isotropic turbulence the statistics of the smallest scale eddies is dependent upon the viscosity,  $\nu$ , and the mean energy dissipation  $\bar{\varepsilon}$ . The Kolmogorov length scale can therefore be calculated using:

$$\eta = \left( \frac{\nu}{\bar{\varepsilon}} \right)^{\frac{1}{4}} \quad (2.20)$$

The Kolmogorov scale can also be defined in terms of the Reynolds number and integral scale:

$$\eta = \frac{L}{Re^{3/4}} \quad (2.21)$$

The second hypothesis of similarity proposed by Kolmogorov stated that: at large Reynolds numbers turbulent motions in the range  $\eta \ll l \ll L$  on the scale of  $l$  are dependent upon the mean dissipation rate but are independent of the viscosity.

The scale in between the largest integral scale and smallest Kolmogorov scale is known as the Taylor scale, or Taylor micro-scale (Hinze [1959], Tennekes and Lumley [1972], Turns [1996]). However, while the general consensus is that the Taylor scale lies between the largest and smallest scales, the overall definition is somewhat ambiguous. It has been proposed that the Taylor scale can be derived from the autocorrelation used to determine the integral scale by (Lipatnikov [2012]):

$$\lambda = \left( -\frac{1}{2} \frac{d^2 R}{dr^2} \right)_{r \rightarrow 0}^{-1/2} \quad (2.22)$$

The longitudinal and transverse Taylor scales are related by:

$$\lambda_L = \lambda_T \sqrt{2} \quad (2.23)$$

Like the integral scale the temporal autocorrelation function can be used to find the Taylor time scale of turbulence:

$$\tau_\lambda = \left( -\frac{1}{2} \frac{d^2 R}{dt^2} \right)_{t \rightarrow 0}^{-1/2} \quad (2.24)$$

The Taylor scale in practice can be linked to a predictive integral scale by (Law [2006]):

$$\lambda = \frac{L}{F_\lambda Re^{0.5}} \quad (2.25)$$

where  $F_\lambda$  is a proportionality constant based on empirical data, with values from the literature stated in Table 2.1

Table 2.1: Turbulence constant,  $F_\lambda$  to determine Taylor length scale from integral length scale.

| $F_\lambda$ | Source                     |
|-------------|----------------------------|
| $\sqrt{40}$ | Abdel-Gayed et al. [1987]  |
| $\sqrt{15}$ | Tennekes and Lumley [1972] |
| $\sqrt{16}$ | Scott [1992]               |

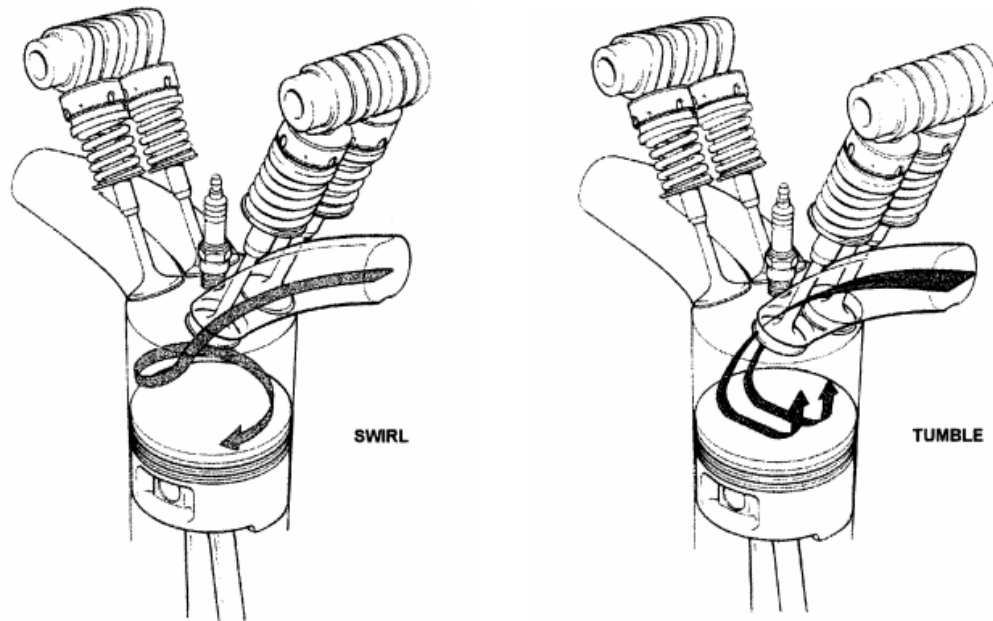


Figure 2.4: Schematic of in-cylinder Swirl and Tumble. Reproduced from Wilson et al. [1993]

#### 2.2.4 Turbulent bulk flow in engines: Swirl and Tumble

While turbulence is random, bulk motions can form within engines. These bulk motions are referred to as swirl and tumble, where swirl is defined as a rotating flow along an axis parallel to the cylinder axis, and tumble is a rotating flow along the axis perpendicular to the cylinder axis. Swirl and tumble are shown schematically in Figure 2.4.

It has been well documented that the intake port and combustion chamber geometries are what dictate the formation of these bulk motions (Heywood [1988]), thus enabling engine designers to consciously choose the type of coherent in-cylinder motion based on their requirements.

For a gasoline direct injection (GDI) engine the effect of swirl motion inhibits mixing and is typically seen as beneficial to stratified charge engines. The review paper by Hill and Zhang [1994] found that the effect of swirl increases the rate of combustion and the burning speed, due to the enhanced turbulence intensity of the flow structure. As swirl decays the turbulence tends to become homogeneous and isotropic (Liou and Santavicca [1983], Liou et al. [1984]), assumptions typically made using turbulence modelling techniques.

Tumble motion is of significant importance to this study as the experimental engine modelled here generates a tumbling in-cylinder flow. Both Wheeler et al.

[2013] and Takahashi et al. [2016] found that medium to high tumble increased the EGR limit, with the EGR limit being the maximum level of EGR permissible for combustion to occur. This increase in EGR limit is needed to offset the increase in NO<sub>x</sub> emissions at higher levels of tumble (Zhang et al. [2014]). The mechanism of NO<sub>x</sub> increase is due to the reduced burning times and therefore increased in-cylinder temperature that occur due to increased turbulence levels when comparing high to low tumble cases (Takahashi et al. [2016]). The increase in turbulence caused by tumble has also been found to be amplified during compression due to piston motion (Witze [1983]). This faster burning for high tumble also results in a reduction of CO formation and an improvement in Brake Specific Fuel Consumption. It has also been found that higher levels of tumble leads to a reduction in cycle-to-cycle variability (Omura et al. [2016]). The probable cause of this reduction is the increase in mixing for GDI engines reducing the levels of small inhomogeneities within the charge. Greater mixing would however lead to an increase in wall wetting, where the mixture condenses on the combustion chamber walls, leading to an increase in HC emissions which is observed for greater tumble (Zhang et al. [2014]). From these observations it can be concluded that higher levels of tumble increases the in-cylinder charge mixing.

## 2.3 Combustion in SI engines

Combustion is the self-supported release of energy through the exothermic oxidation of fuel (Griffiths et al. [1995]), converting the energy within said fuel into mechanical work. Combustion in a SI engine occurs within a cylinder, which can also be referred to as a combustion chamber, where a spark electrode is used to determine the point of ignition. The point of ignition, also known as the spark advance, is a vital parameter with regards to engine performance. The optimum spark timing, also known as Maximum Brake Torque (MBT) timing, is when the engine torque is at a maximum for a given engine speed. The MBT spark timing is typically when 50% of the mass is burned by around 10° after Top Dead Centre (aTDC). Achieving this depends on other engine running conditions, such as pressure, temperature and levels of exhaust gas recirculation. MBT timing is typically determined experimentally using an engine dynamometer or through simulations (Heywood [1988]), where multiple MBT timings can be found for a single running condition. To reduce the chance of autoignition it is the least advanced MBT spark timing that is used.

### 2.3.1 Laminar premixed flames

With the flow field within an SI engine being highly turbulent, the transition between laminar and turbulent flame propagation is extremely fast. Although the flame kernel is initially laminar, wrinkling quickly occurs as the flame is subjected to in-cylinder turbulence. This section describes the physiochemical properties of laminar combustion such as burning velocity, effects due to stretching and laminar flame instabilities.

#### 2.3.1.1 Propagation of laminar premixed flames

Laminar premixed flames comprise of a thin reaction zone which is also known as the laminar flame thickness. The mechanism of laminar flame propagation within this reaction zone is highly complex, however the overall propagation of a laminar flame can be simplified into four zones. This zonal division is shown in Figure 2.5 and assumes a one-dimensional adiabatic unstretched premixed flame.

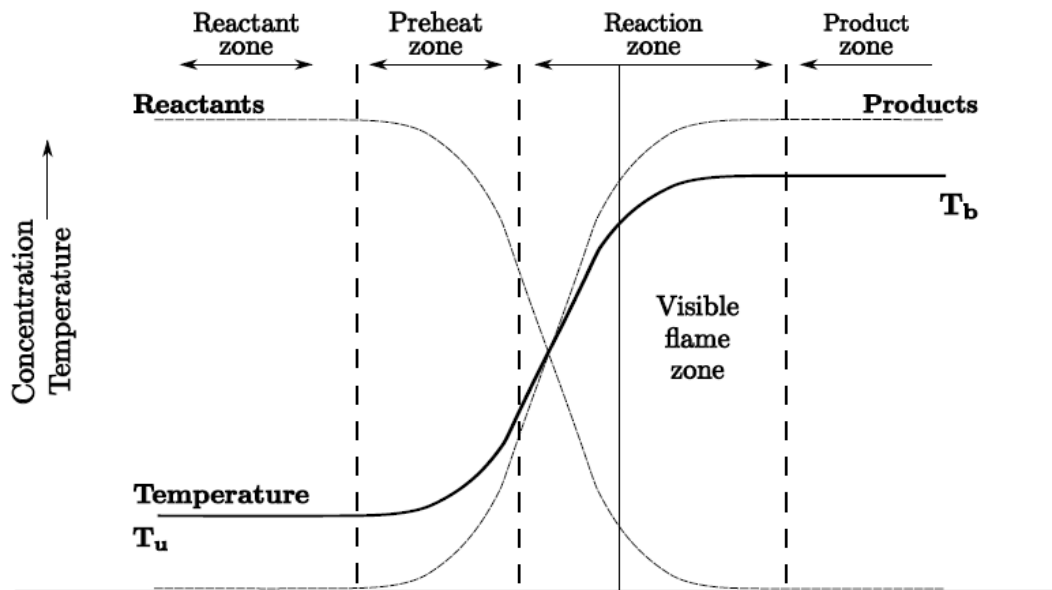


Figure 2.5: Concentration and temperature profiles for the mechanism of flame propagation. Taken from Conway [2013] where it was adapted from Griffiths et al. [1995].

The four main zones are as follows: Reactant zone, where the fuel and air mixture are contained. Preheat zone, where the reaction rate is negligible and conductive heat flow into the cooler region is greater than the heat loss, causing an increase in gas temperature. The reaction zone structure is determined by the balance between

the reaction and the molecular diffusion. The reaction rate is small except in a small temperature interval  $T_u < T < T_b$  where  $T_u$  is the temperature of the unburned reactants and  $T_b$  is the temperature of the burned gas. In this temperature interval self-sustaining reactions are supported. These self-sustaining reactions lead to all of the reactants being consumed. Once all the reactants are consumed only products of the combustion remain, this is the product zone. The emission of electronically excited species such as CH, CN, C<sub>2</sub>, CHO and CO<sub>2</sub>, emit light in the reaction zone as they return to their ground state (Griffiths et al. [1995]), hence the flame becomes visible.

### 2.3.1.2 Laminar burning velocity and flame thickness

An unstretched laminar flame will propagate through a mixture at a characteristic rate, known as the burning velocity. This unstretched burning velocity is only dependent upon the mixture composition, temperature and pressure (Gillespie et al. [2000]). The laminar burning velocity is defined as the relative velocity, normal to the flame front, with which the unburned gas moves into this front (Rallis and Garforth [1980]). Under ideal conditions, where the flame stretch rate is zero, the laminar burning velocity is also the mass burning rate, i.e. the rate of propagation equal to rate of conversion of unburned gas into burned gas, and can be expressed as:

$$u_l = \frac{1}{\rho_u} \left( \frac{\dot{m}_r}{A} \right) \quad (2.26)$$

where  $\rho_u$  is the density of the unburned gas, A is the surface area of the cold front and  $\dot{m}_r$  is the mass burning rate of the reactants. Most practical flames can rarely be modelled as one-dimensional and require a stretch factor to take into account strain and curvature effects.

A propagating flame in a non-uniform laminar flow-field is subjected to strain and curvature effects, leading to changes in frontal area and thus laminar burning velocity (see Eq. (2.26)). The total rate of flame stretch, acting at a point on the flame surface, is defined as the rate of change of the flame area, A, of an infinitesimal element surrounding that point over the infinitesimal area (Bradley et al. [1998]):

$$\alpha = \frac{1}{A} \left( \frac{dA}{dt} \right) \quad (2.27)$$

The effect of flame stretching is essential to suppress the onset of cellularity, where the flame is perturbed by instabilities and is deemed unstable. The form of instabilities are characterised by cells, cracks or ridges appearing within the flame

front for what should be a smooth laminar flame. It is worth noting that for this work flame instabilities were neither observed or predicted due to the effect of turbulence on the flame. However, the high pressures associated with engines means that instabilities are highly likely to exist during the initial laminar-like flame propagation, prior to the main turbulent flame, under engine running conditions (Bradley et al. [2009]). The transition from a stable flame into a cellular flame structure is observed at the critical Peclet number (Gu et al. [2000]):

$$Pe_{cl} = \frac{r_{cl}}{\delta_l} \quad (2.28)$$

where  $r_{cl}$  is the radius at which the cellular flame structure becomes apparent. A schlieren image of a cellular flame is shown in Figure 2.6. The laminar flame instabilities have the appearance of cracks in the flame structure, before the flame cracking leads to a metastable cellular flame (Bradley and Harper [1994]). The

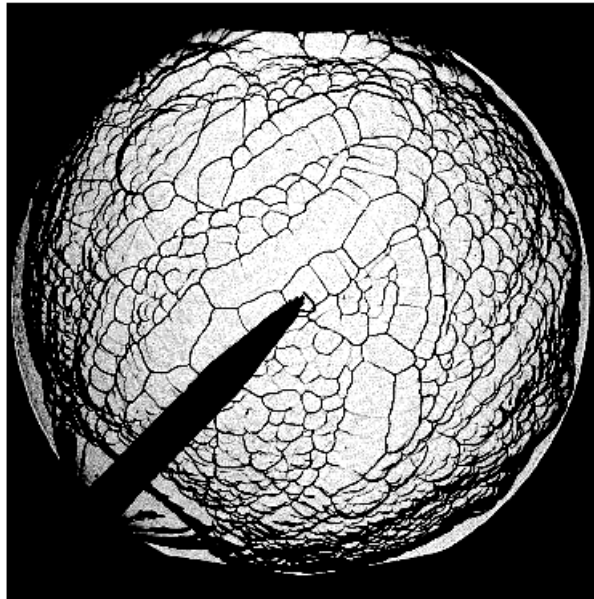


Figure 2.6: Schlieren image of a cellular iso-octane/air mixture at 360 K and 0.5 MPa, taken from Mumby [2016].

effect of this cellular structure on the laminar flame speed, and therefore laminar burning velocity, is presented in Figure 2.7. Once the stable flame becomes unstable at the critical Peclet number,  $Pe_{cl}$ , the stretched laminar flame speed experiences a sharp increase due to the cellular structure, where the surface area is much greater than it is for the smooth laminar flame. The cause of these instabilities can be categorised into two mechanisms, the hydrodynamic instability and the diffusive thermal instability. A full description of these mechanisms has been omitted for the sake of brevity. Readers are directed to the works of Lipatnikov [2012], Conway

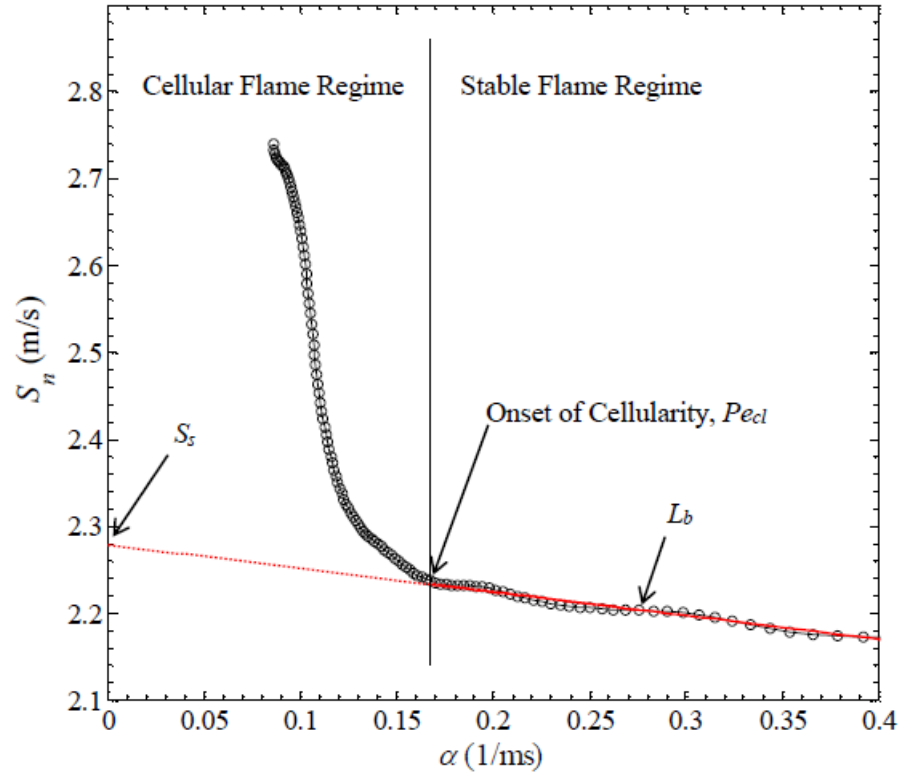


Figure 2.7: Variation of laminar flame speed with flame stretch for iso-octane/air mixtures at 360 K and 1.0 MPa, taken from Mumby [2016].

[2013], Ling [2014], Mumby [2016] for further detailed information.

For a non-planar flame the mass of gas entrained into the flame is seldom the same as the rate of formation of the burned product, due to flame thickness (Gillespie et al. [2000]). The stretched laminar burning velocity can therefore be defined based on the entrainment velocity (Rallis and Garforth [1980]):

$$u_n = \frac{1}{\rho_u} \left( \frac{\dot{m}_e}{A} \right) \quad (2.29)$$

or on the rate of production of burned gas (Bradley et al. [1996]):

$$u_{nr} = \frac{1}{\rho_u} \left( \frac{\dot{m}_r}{A} \right). \quad (2.30)$$

The stretched laminar burning velocity,  $u_n$ , based on the rate of entrainment is determined from optical experiments, such as those by Bradley et al. [1998], Jerzembeck et al. [2009] and Baloo et al. [2016]. Whereas the laminar burning velocity based on the rate of burned gas production,  $u_{nr}$ , is typically determined from pressure rises (Ryan and Lestz [1980], Metghalchi and Keck [1982], Rhodes and Keck [1985]). Presented in Figure 2.8 are the two burning velocities described by Eqs. (2.29) and

(2.30) at increasing stretch rates. It is shown that at zero stretch these two quantities are equal.

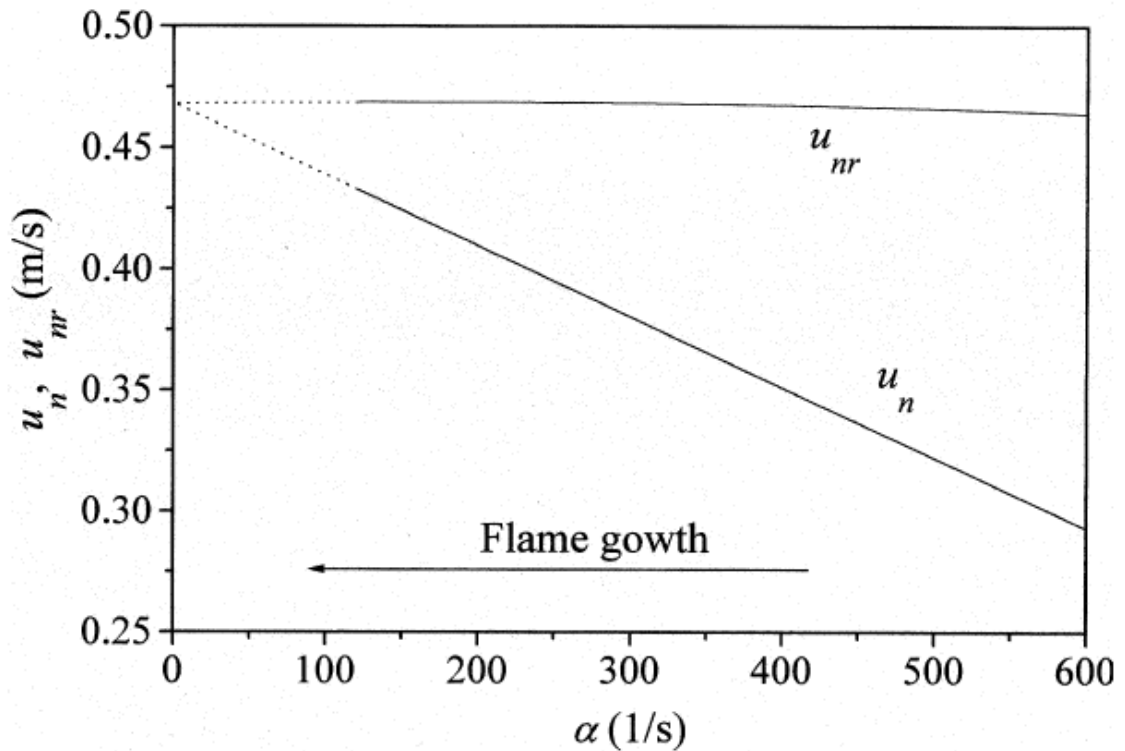


Figure 2.8: Variation of  $u_n$  and  $u_{nr}$  with stretch rate for iso-octane-air mixtures. Taken from Gillespie et al. [2000].

As previously stated the laminar burning velocity depends on mixture composition. This can mean either the type of fuel, equivalence ratio, or for engine applications the amount of residual gas recirculated into the combustion chamber. The effect of this exhaust gas recirculation (EGR) on the laminar burning velocity is discussed in section 2.7. The dependence of the laminar burning velocity on fuel:air equivalence ratio is shown in Figure 2.9. The maximum laminar burning velocity is shown to be at an equivalence ratio between 1.0 (stoichiometric) and 1.1. An investigation into the effect of carbon number on the burning velocity of gasoline components<sup>2</sup> was carried out by Burluka et al. [2016] who found that the maximum burning velocity was at  $\phi = 1.1$  regardless of carbon number. Despite the short time spent propagating as a laminar flame, the laminar burning velocity,  $u_l$ , is a vital parameter for calculating premixed turbulent combustion.

The laminar burning velocity is different to the laminar flame speed, which is defined as a measure of the flame propagation velocity relative to a stationary ob-

<sup>2</sup>The gasoline components analysed were: n-pentane, n-hexane, n-heptane and n-octane.

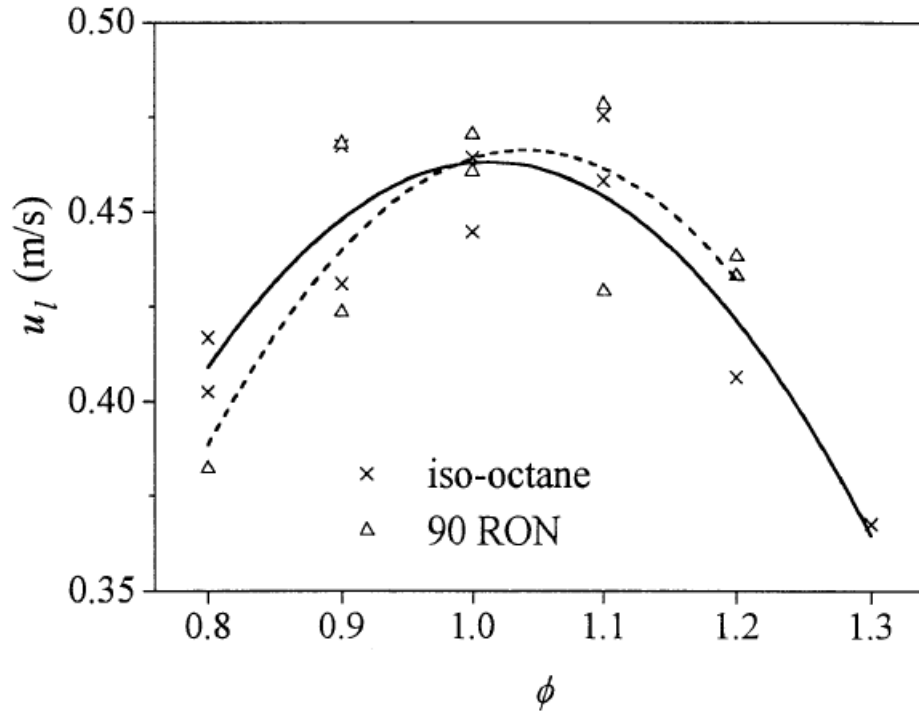


Figure 2.9: Laminar burning velocity for iso-octane and 90 RON (90% iso-octane, 10% n-heptane mixture) at varying equivalence ratios at 358 K and 0.1 MPa, taken from Bradley et al. [1998].

server. The flame speed is not an intrinsic property of the mixture instead being dependent upon the configuration of the experiment. The laminar flame speed is easily measured as it is simply the rate of change of the flame radius,  $f_r$ , w.r.t time.

$$S_n = \frac{df_r}{dt} \quad (2.31)$$

The stretched laminar flame speed,  $S_n$ , is the sum of the stretched laminar burning velocity and the velocity of the gas,  $v_g$ , expanding adjacent to the flame front.

$$S_n = v_g + u_n \quad (2.32)$$

The laminar flame thickness represents the depth of the reaction zone (Griffiths et al. [1995]), where the conversion of unburned gas to burned gas occurs gradually. The flame thickness of a laminar flame is difficult to quantify, and as such numerous definitions exist. Definitions of laminar flame thickness can be based on mass diffusion, thermal diffusion or a hydrodynamic length (Gillespie et al. [2000]). An approximation of the laminar flame thickness using a hydrodynamic length is

expressed as (Abdel-Gayed et al. [1984]):

$$\delta_l = \nu/u_l \quad (2.33)$$

### 2.3.2 Turbulent premixed flames

Both experimental and Direct Numerical Solution (DNS) data show that the difference in molecular transport coefficients for the fuel, oxidant and heat at weak, moderate and high turbulence are important for describing turbulent premixed combustion (Lipatnikov and Chomiak [2005]).

A turbulent flame has three primary regions associated with it: the flame has a leading edge (front),  $f_{re}$ , a reaction zone (thickness),  $\delta_t$ , and a trailing edge (burned gas radius),  $f_{rb}$ , as is illustrated diagrammatically in Figure 2.10. These definitions are used throughout this study. The average radius,  $f_{rav}$ , is included for clarity, however it does not take part in any of the modelling used in this study.

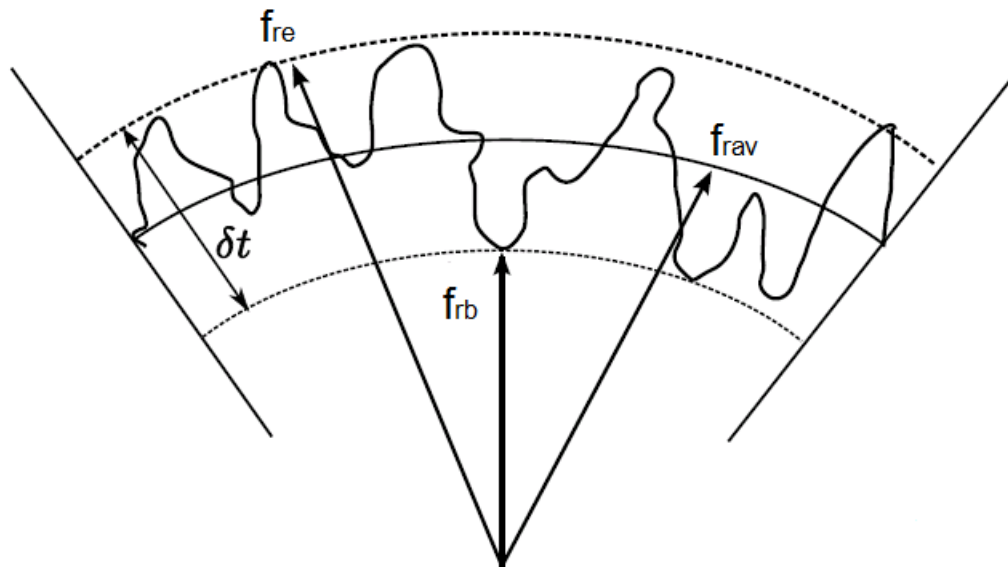


Figure 2.10: Radii definitions that are traditionally attributed to turbulent premixed flames, modified from Conway [2013].

This section describes relevant combustion parameters, flame propagation (including flame structure), and burning velocity for turbulent premixed flames.

### 2.3.2.1 Turbulent combustion parameters

Turbulent flames are subject to constant deformation through interaction with the flow field. The wrinkling effect of turbulence on a flame surface can be described using the Karlovitz number,  $K$ , which is the ratio of chemical lifetime,  $\tau_c$ , to turbulent scale lifetime,  $\tau_\lambda$ , for which the turbulent scale is typically the Taylor micro-scale (Abdel-Gayed et al. [1987]):

$$K = \frac{\tau_c}{\tau_\lambda} \quad (2.34)$$

The Karlovitz number can be written in terms of the laminar burning velocity,  $u_l$ , and laminar flame thickness,  $\delta_l$ :

$$K = \left( \frac{u'}{\lambda} \right) \left( \frac{\delta_l}{u_l} \right) \quad (2.35)$$

Another dimensionless number used to describe the effect of turbulence on combustion is the Damköhler number:

$$\text{Da} = \left( \frac{L}{u'} \right) \left( \frac{u_l}{\delta_l} \right) \quad (2.36)$$

The Damköhler number is a ratio of turbulent time-scale to chemical lifetime, i.e. the inverse of the Karlovitz number. The Damköhler number uses the integral length scale unlike the definition of the Karlovitz number in Eq.(2.34) which uses the Taylor micro-scale. These two dimensionless numbers can be used to quantify the structures of common flames. A discussion of the flame structure of turbulent premixed combustion and the relevant structure to SI engines is found in section 2.3.2.3.

### 2.3.2.2 Turbulent burning velocity

Experimental data of turbulent burning velocities and turbulent flame speeds at moderate turbulence were reviewed by Lipatnikov and Chomiak [2002]. The general trends were:

- Turbulent burning velocity and turbulent flame speed increased with increasing turbulent RMS velocity.
- Turbulent burning velocity and  $du_t/du'$  increase with an increasing laminar

burning velocity.

- Turbulent flame speed and burning velocity increases due to increasing pressure despite the laminar burning velocity decreasing.
- The effect of the integral length scale on the turbulent flame speed can be contradictory but most available results show an increase in turbulent burning for an increasing integral length scale.
- A decrease in turbulent burning velocities and flame speeds for an increasing molecular heat diffusivity.

While the turbulent burning velocity does increase with turbulent RMS velocity, this effect does not hold true for ever increasing RMS values. Nivarti and Cant [2017] used DNS to investigate the bending effect in premixed turbulent flames. The bending effect is presented in Fig. 2.11, where the turbulent burning velocity stops increasing linearly with turbulent RMS velocity. This effect has been reviewed by Lipatnikov and Chomiak [2002], Lipatnikov [2012] and Driscoll [2008] without any real explanation being formed.

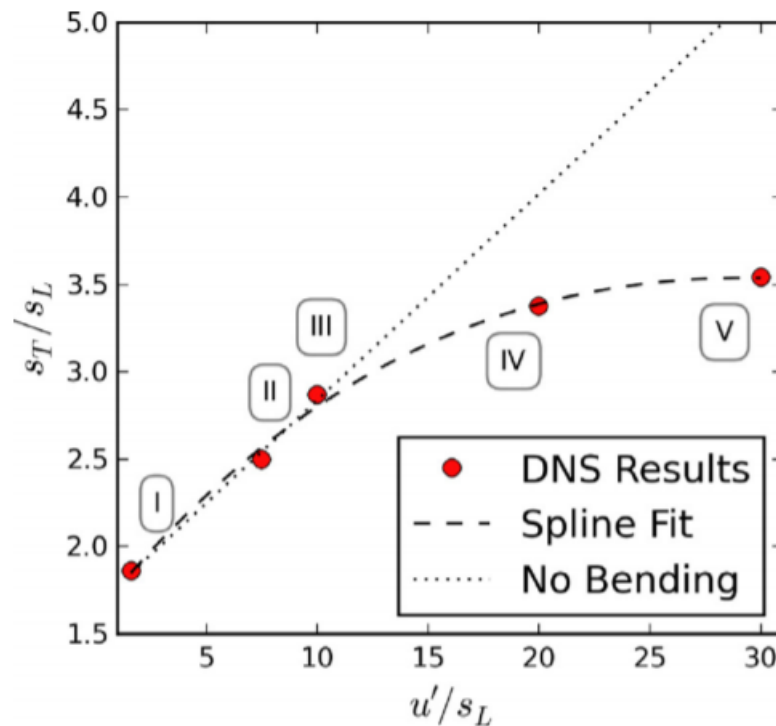


Figure 2.11: DNS simulations showing how turbulent burning velocity diminishes at high turbulence intensity, taken from Nivarti and Cant [2017].

Nivarti and Cant [2017] concluded that the turbulent burning velocity is governed

by the flame surface area even at high levels of turbulence. Through analysing the tangential strain and mean curvature the non-linear flame surface area is calculated. One important conclusion drawn is that local flame quenching appears not to govern the “bending” effect.

### 2.3.2.3 Combustion regimes

The combustion can be described as either laminar or turbulent depending on the Reynolds number of the unburnt gas. Premixed turbulent combustion may be further categorised based on  $L/\delta_t$ , a dimensionless turbulent length scale, and  $u'/u_t$ , a dimensionless turbulent velocity. These are plotted against each other on logarithmic scales in Figure 2.12.

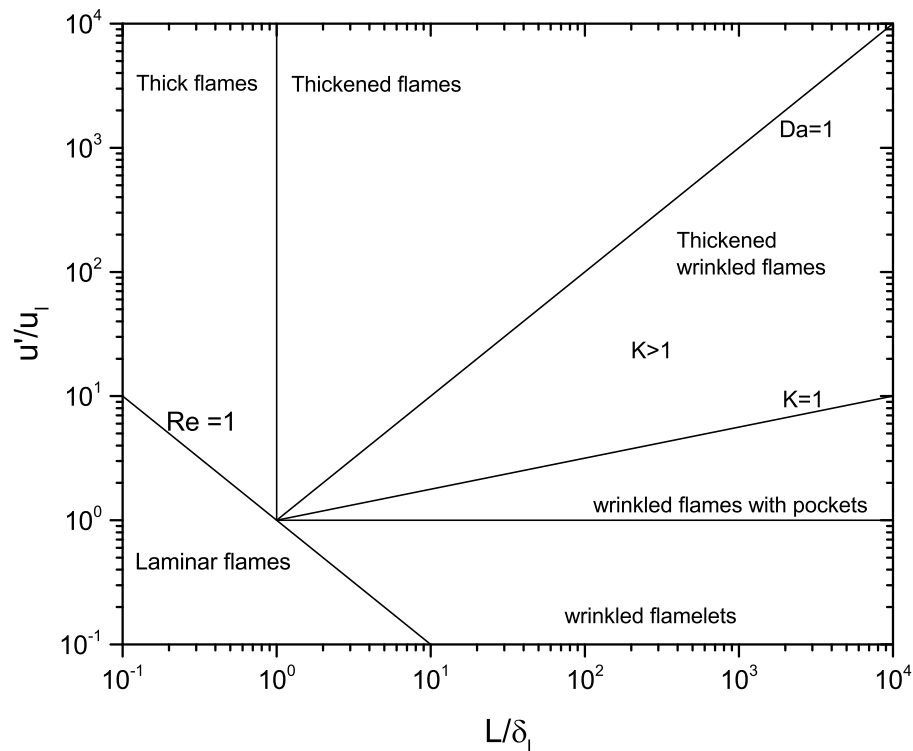


Figure 2.12: A Borghi diagram containing information on turbulent combustion regimes.

The lines in Figure 2.12 separate the boundaries between different combustion regimes, which are typically defined as follows (Griffiths et al. [1995], Borghi et al. [1998])

$Re < 1$  **Laminar combustion**

$Re > 1, K > 1, Da > 1$  **Thickened flames:** Turbulence is fast compared to chemistry and combustion occurs without a distinct propagating flame front.

$Re > 1, K > 1, Da < 1, u' > u_l$  **Wrinkled flames with pockets:** The flame surface is wrinkled and may be discontinuous but remains similar to a laminar flame in structure. This is because chemical reactions occur faster than they can be acted upon by the turbulence. Due to it behaving as a wrinkled laminar flame it can be grouped into the flamelet regime.

$Re > 1, K > 1, Da < 1, u' < u_l$  **Wrinkled flamelets:** A laminar flame that is wrinkled by the turbulence with a continuous unbroken flame surface.

Conway [2013] found for four different engines (boosted and non-boosted) that SI engine combustion lies within the wrinkled flame with pockets region. The study by Ling [2014] was found to be in agreement that SI combustion occurs in the flamelet regime, however some points were determined to be in the wrinkled flamelets region. This is possibly attributed to the low engine speed of 750 rpm<sup>3</sup>, where the turbulent RMS velocity would be considerably lower. Borghi et al. [1998] stated that the boundaries between domains are fairly arbitrary and in reality are much less well defined than the lines indicate.

#### 2.3.2.4 Flame propagation

For the flame to propagate the spark plug must provide enough energy for the reactions to be self-sustaining. Liu et al. [2013] found that a flame propagating in an SI engine has three main stages. The first stage is where the flame has a fast initial acceleration. This is possibly associated with the transition from a laminar to turbulent flame shortly after the spark kernel is formed. During this initial stage only around 3% of the mass is burned. The second stage is where the flame then propagates at relatively constant burning rate, with around 30% of the total mass burned at the end of the steady propagation stage. The final stage is where the flame decelerates and quenches as it approaches the cylinder walls, the distance at which the flame decelerates was found to be one and half times the integral length scale of the turbulent flow. It is during this deceleration of the flame that the remaining mass ( $\approx 70\%$ ) is burned.

As the flame radius increases the turbulence length scales relative to the size of the flame change. This relative change between flame radius and turbulent length

---

<sup>3</sup>750 rpm is typically an idling engine speed, as opposed to a running speed. A typical running speed of 1500rpm would produce higher  $u'$  values.

scales effects how the turbulence interacts with the flame as it propagates. Small radii flames are more likely to be convected by the larger scale eddies, with only the smaller scales capable of wrinkling the flame. As the flame grows the larger eddy length scales will also contribute to flame wrinkling and the flame will undergo wrinkling for the whole turbulence spectrum. The increase in turbulent burning velocity due to this phenomena is typically accounted for through use of a flame development factor (Lipatnikov and Chomiak [1997]) or an effective turbulent RMS velocity (Abdel-Gayed et al. [1987]). A description of these models can be found in section 3.2.6.

## 2.4 Autoignition

While autoignition itself has not been investigated in this study, an advantage of introducing recirculated exhaust gas into the cylinder is a reduction in the probability of an autoignition event occurring, and this is one of the fundamental reasons why this strategy is employed (see section 2.7 ). It therefore seems prudent to provide a brief description of autoignition and explain why engine manufacturers seek to reduce the probability of its occurrence.

Autoignition occurs when the end gas (unburned mixture away from the propagating flame front) spontaneously ignites due to the pressure and temperature of the mixture (Heywood [1988]). This end gas autoignition then causes the remaining unburned gas to ignite. This process can lead to knocking where the in-cylinder pressure fluctuates largely, creating large vibrational noise within the engine. Engine manufactures seek to reduce knocking as the violent pressure oscillations have been known to destroy engine components. Autoignition is a limiting factor when looking to improve the thermal efficiency of SI engines. Thermal efficiency is governed by compression ratio and specific heat ratio. Increasing the compression ratio is limited due to the increased chance of an autoignition event.

## 2.5 Cycle-to-cycle Variability

Cyclic variations in engines may be defined as the non-repeatability of the combustion process on a cycle-resolved basis (Ball et al. [1998]). Deterministic effects from previous combustion cycles are carried on to subsequent cycles. The changes in pressure traces between cycles is dependant upon the operating conditions and is not random, however due to the fluctuations of the in-cylinder turbulent flow, the pres-

sure trace may be different even under the same operating conditions. Abdi Aghdam et al. [2007] found that a linear variation in the turbulent RMS velocity induces non-linear changes in the pressure development that is associated with the temperature feedback of the flame. The most significant causes of cyclic variation are as follows (Dai et al. [2000]):

- The turbulent RMS velocity ( $u'$ ).
- The speed and direction of the mean turbulent flow at the spark plug.
- Equivalence ratio at the spark plug and in the chamber.
- Variation in spark discharge characteristics.
- Charge mass variations.
- Effects such as blow-by and other crevice effects.

These causes can be categorised into prior cycle effects, such as the amount of residual gas, which changes the A/F ratio in cylinder, or same cycle effects such as the flow within the cylinder. These characteristics vary from engine to engine depending on a number of factors, such as: engine geometry, the fuel injection system in use and the operating conditions of the engine (Dai et al. [2000]). Cycle to cycle variability in the combustion rate is manifest from the moment of ignition (Hill and Zhang [1994]). However the observed magnitude of the cyclic variability cannot be entirely attributed to the initial flame formation (Aleiferis et al. [2004]).

There are several ways in which cyclic variation can be measured. The most common parameters are as follows (Heywood [1988], Dai et al. [2000], Bade Shrestha and Karim [2001]):

- Indicated Mean Effective Pressure (IMEP).
- In cylinder pressure versus crank angle.
- The rate of in-cylinder pressure change.
- Mass burning rate.
- Ignition delay.
- Flame front position.

A statistical spread of the cyclic variations is known as the Coefficient of Variability (COV). The COV is measured for one of the above parameters to determine the cyclic variability. The most appropriate parameter to measure for the COV is a topic of debate. Dai et al. [2000] argues that the COV of the IMEP is a better measure for the cyclic variability as in cylinder pressure can be effected by spark phasing. Heywood [1988] suggested that a COV in IMEP that was greater than 10% would result in a deterioration of drivability noticeable to the driver. However, Samuel et al. [2010] found that COV analysis of in-cylinder pressure provided more insight into the cyclic variations during different parts of the combustion cycle. This analysis is not possible using the COV of IMEP. Throughout the work presented here the cyclic variability is utilised as a means to further categorise the type of combustion cycle predicted (fast, middle, slow) from the quasi-dimensional engine simulations.

## 2.6 Stratified Charge Engines

The concept of fuel stratification started in the 1920's when engineers tried to incorporate the best facets of SI and Diesel engines. The general idea was to use the direct-injection (DI) of the Diesel engine and ignite the fuel as it mixes with the air, thus allowing a greater compression ratio (Heywood [1988]). The combustion of inhomogeneous fuel distributions is described as partially-premixed combustion. When the charge-air mixture is simultaneously fuel rich and fuel lean at different points in space, the charge is stratified. If the composition includes fuel-air mixture at stoichiometric conditions then the combustion zone structure resembles both premixed and non-premixed flames. Due to the rich fuel mixture near the spark plug a longer spark duration is required to properly ignite the fuel.

The benefits of stratified charge were stated by Zhao et al. [1999] and include (i) reduced pumping losses due to unthrottled part-load operation, (ii) decreased heat loss to cylinder walls due to the cool air/lean mixture near the cylinder walls and (iii) an increase in compression ratio due to lower end gas temperatures associated with stratified combustion. Lower end gas temperatures reduce the chance of autoignition, although typically the stratified charge engines run under conditions in which the probability of autoignition is already small. Typically stratified mixtures are utilised at lower engine speeds at part-load conditions where the reduction in pumping losses has the greatest impact. This strategy was employed in the GDI engine maps by Mitsubishi, Mercedes-Benz, Nissan and Honda (Iwamoto et al. [1997], Karl et al. [1997], Ashizawa et al. [1998], Horie et al. [2004].) The GDI engine map

for the Honda engine is shown in Figure 2.13.

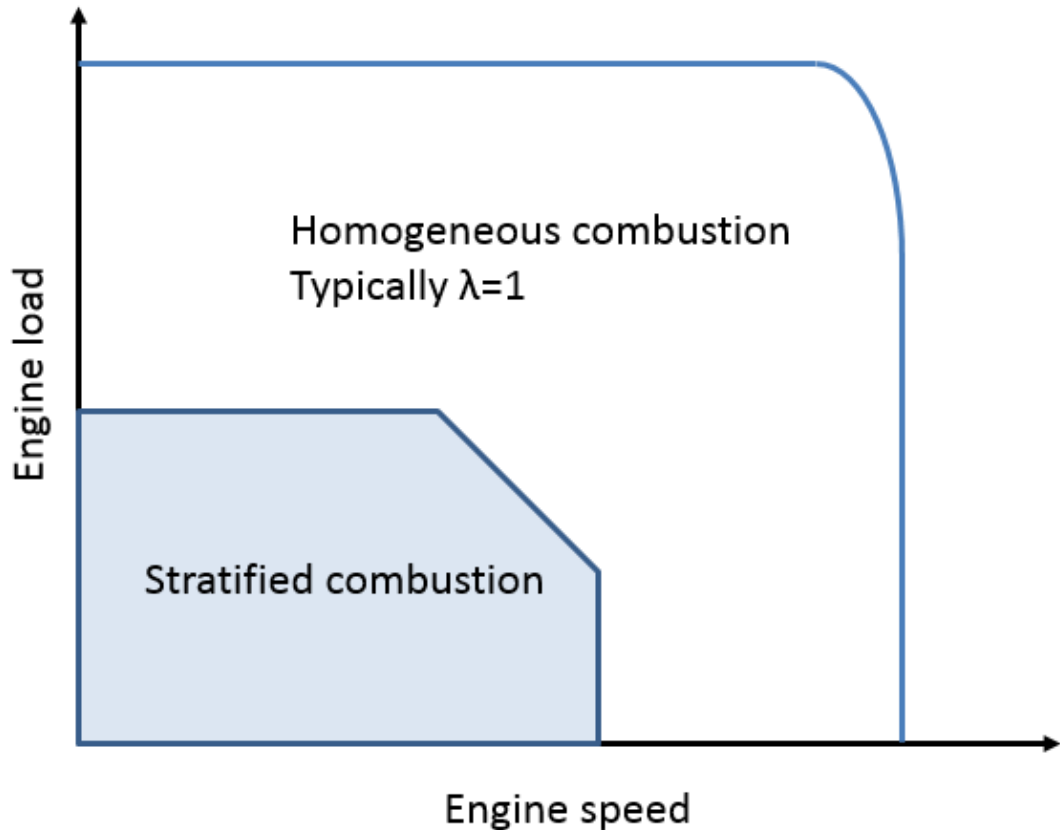


Figure 2.13: General engine operating map for a GDI engine. Recreation based on engine map found in Horie et al. [2004].

Disadvantages of fuel stratification are an increase in HC emissions when compared to a homogeneous lean burn engine due to the excess air, as well as control of the fuel spray to ensure the fuel arrives at the spark plug at the correct time. Stratification also causes the exhaust temperature to be cooler than that of a homogeneous lean burn engine, therefore consideration must be given to the aftertreatment as the three way catalyst efficiency can become sub-optimal when operating at these low temperatures (Schmieg [2010]). However, Wirth et al. [1998] found that fuel stratification is a viable combustion strategy at low load, showing a decrease in both fuel consumption and NOx emissions. This finding is supported by Silva et al. [2017] who compared a split injection stratified charge to a homogeneous baseline in a 3-cylinder engine at 4 bar BMEP and 1000 rpm using ethanol air mixtures. The lean stratified mixture at the cylinder walls will have a greater O<sub>2</sub> concentration than the homogeneous case and therefore, at the same temperature, produce more NOx emissions. The decrease in NOx is most likely attributed to the difference in combustion temperature, as the mechanism for NOx formation is dependent upon both temperature and O<sub>2</sub> concentration (Zeldovich [1985], Lavoie et al. [1970]):



where  $k_i$  is a reaction rate constant in the form of an Arrhenius function:

$$k_i \sim \exp\left(-\frac{E_{act}}{RT}\right) \quad (2.38)$$

Fujimoto et al. [1995] investigated the combustion and NOx emissions of mixture stratification in a constant volume combustion chamber (CVCC) using both propane-air and hydrogen-air mixtures. The study compared NOx emissions for homogeneous, centrally rich and centrally lean stratified mixtures, with the homogeneous case producing the lowest NOx emissions across the range of total equivalence ratios investigated. For overall lean mixtures the centrally rich stratified mixture produced the greatest NOx emissions. The results reported are for the propane-air mixtures due to it being a hydrocarbon fuel and therefore a better representation of SI engine combustion. These results contradict the findings by Wirth et al. [1998] and Silva et al. [2017]. The contradiction could be attributed to in-cylinder residuals for the engine experiments, reducing the oxygen concentration in the lean mixture as no description of skip firing (a strategy to flush out any in-cylinder residuals) is mentioned in either engine paper.

Not only has fuel stratification been investigated for NOx emissions but also soot and Particulate Number (PN). Bock et al. [2018] used a 2.0 L BMW N43B20 four-cylinder engine to analyse emissions in homogeneous (stoichiometric and lean) and stratified (lean) modes. The fuel injection for the stratified condition employed a triple injection strategy, with two injections during compression prior to the spark event and a final injection just after the spark timing. The soot levels for the stratified case at an engine speed of 1400 rpm and load of 2 bar BMEP were found to be approximately 2 mg/kWh, which is 200 times greater than the lean homogeneous case (0.01 mg/kWh) and 67 times greater than the stoichiometric homogeneous case (0.03 mg/kWh). Although emissions do suffer when operating under stratified conditions, fuel consumption does improve under the same speed and load conditions. The same study found a 8.3% improvement in Brake Specific Fuel Consumption (BSFC) when comparing the lean stratified and lean homogeneous cases, and a 17.5% improvement for the the lean stratified case when compared to the stoichiometric homogeneous case.

The heat loss to cylinder walls of a stratified charge has been investigated experimentally by Huegel et al. [2015] who used surface thermocouples in a single-cylinder engine to determine the instantaneous heat flux at various locations within the engine. The stratified charge led to lower liner temperatures for the stratified case compared to the homogeneous across all the spark timings that were investigated, however the temperature of the piston was found to be dependent upon spark timing.

The results from the literature report that stratified charge operation has a number of advantages, such as improved BSFC and a reduction in NO<sub>x</sub> emissions. These advantages make the stratified operating mode viable for engine manufacturers. It therefore seems prudent to improve modelling capability of this engine operating mode.

### 2.6.1 Mixture formation

Most modern engines utilise a direct injection (DI) technique, where the fuel is injected straight into the combustion chamber. Experimental work by Berckmüller et al. [1996] determined that injection timing is an important parameter for mixture formation in stratified engines. In an attempt to stratify the charge and prevent it mixing throughout the cylinder a late injection timing strategy is employed. Stratified charge (SC) engines can be further divided into three categories, based on the method used during mixture formation. These methods are: air-guided, wall-guided or spray-guided stratified charge engines. A schematic depicting the different categories is presented in Figure 2.14.

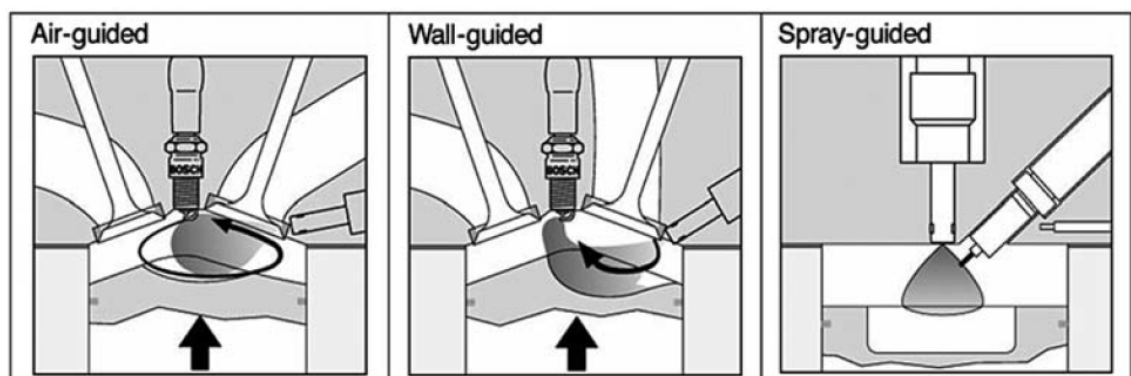


Figure 2.14: Categories of stratified charge engines, taken from Fansler et al. [2015] where it was reproduced from Zhao et al. [1999].

The spray-guided technique is the simplest method, where the spray is directly injected into the vicinity of the spark plug. This still requires design consideration

and exact positioning of the spark plug and injector. It also creates high stress on the spark plug. The wall-guided method injects onto a specially designed surface that directs the charge towards the spark plug. The issue with wall-guided systems is the level of fuel wetting that occurs on the piston surface, resulting in greater hydro-carbon (HC) emissions (Stanglmaier et al. [1999], Sandquist et al. [2000]). The air-guided system utilises the in-cylinder flow properties to transport the fuel into the vicinity of the spark plug. This method would seem the hardest to control as the turbulent in-cylinder motion varies from cycle to cycle (Dai et al. [2000]).

A recent investigation into the effect of injection timing on the air-flow structure was carried out by Chen et al. [2018], using Particle Image Velocimetry (PIV) in an optical engine running at 1300 rpm. The study found that for the late injection stratified case it took 21 crank angle degrees (CA°) to vaporise all of the fuel. It was also found that late injection timing did not increase the cycle-to-cycle variability (CCV) of the air-flow, however it did increase the (CCV) of the kinetic energy, which is thought to be the possible contributing factor in the increase in CCV of combustion.

Addepalli et al. [2017] studied the effect of mixture distribution using CFD analysis. Four stratified cases were compared, one being an “ideally” stratified case and the other three for different fuel injector orientations. The “ideally” stratified case was defined as a linearly decreasing equivalence ratio w.r.t a dimensionless distance. The study concluded that the peak heat release rate for the non-idealised cases are much lower than the idealised case, with the case closest to the ideal case still having a 32% lower peak heat release rate. The study also found that the NO<sub>x</sub> formation was greatest for the ideal condition. Performance and emissions levels were found to be highly dependent upon the mixture formation.

It can be concluded that SC engines need to be both designed and operated “just right” to work effectively (Fansler et al. [2015]). This was first postulated by Ricardo [1922] almost a century ago.

## 2.6.2 Partially premixed combustion

Partially premixed combustion occurs when a flame propagates through an inhomogeneous mixture. Lipatnikov [2012] summarises five specific effects that are involved in partially premixed combustion. These effects are:

1. Dependence of the burning rate on the inhomogeneity of the mean mixture composition.

2. Dependence of the burning rate on the turbulent pulsations in the local mixture composition.
3. Mixture-controlled after-burning of lean and rich combustion products.
4. An increase in flame surface area due to mixture inhomogeneities.
5. Variations in local burning rate due to the heat and reactant fluxes from/to neighbouring leaner or richer components.

However Bilger et al. [2005] states that in a situation where the mixture is either all fuel-rich or all fuel-lean, and the presence of a stoichiometric mixture is absent, the local combustion zone mixture resembles premixed combustion. Although the zone structure is representative of a premixed flame, the inhomogeneities do lead to local fluctuations in burning rate. This is in agreement with point 1 in the above list.

### 2.6.3 Stratified charge modelling

The literature reviewed in this section for stratified charge modelling has led to the following summary:

- CFD does a reasonable job of predicting in-cylinder pressure for a stratified charge GDI engine.
- The thermodynamic/ quasi-dimensional models have either not been validated against any experimental data, draw conclusions that have not been backed up anywhere in the literature, or simply lack the details of how fuel stratification was modelled.

There was therefore a need to develop a quasi-dimensional thermodynamic stratified charge model and validate it against experimental data. The details of the studies that allowed for such statements to be made are described in the remainder of this section.

Traditionally SC charge engines have been modelled using CFD to allow for the the spray and mixture formation to be resolved in three-dimensions. An early investigation into Gasoline Direct Injection (GDI) engines by Ahmadi-Befrui et al. [1991] investigated inhomogeneous charge combustion using a Favre averaged Navier Stokes equation. The study concluded that the pre-combustion charge distribution was largely preserved throughout the flame propagation. The charge preservation is typical for the in-cylinder generated swirl motion.

Duclos and Zolver [1998] investigated a GDI engine under three running conditions: lean homogeneous, stoichiometric homogeneous and lean stratified, using the KIVA code to solve the Reynolds Averaged Navier Stokes (RANS) equation. The study established that the flame propagation for the stratified case was different to the homogeneous case. Typically the homogeneous case burned most of the fuel as the flame approaches the liner. The stratified case had oxidised over 50% of the fuel as the piston approached TDC. At this point in time the flame was not close to the cylinder walls. This supports the claims by Ahmadi-Befrui et al. [1991] that the charge is largely preserved over the course of the flame propagation, implying small changes occur to the charge distribution over time. However, the context of these findings must be accounted for, with the charge preservation in Duclos and Zolver [1998] most likely due to the bowl-in-piston engine design used. The swirl assisted engine studied in Ahmadi-Befrui et al. [1991] also helped to preserve the charge. This charge preservation is therefore due to the engine design only and is not necessarily a trait of stratified charge operation. The study by Duclos and Zolver [1998] also found that the interactions between liquid droplets of fuel and the piston is a major problem for stratified charge engines. This wall wetting is why newer engines opt for spray-guided stratification systems. The requirement for the quasi-dimensional model is therefore to physically model the fuel injection without 3-D spatial resolution.

The studies by Huang et al. [2014b], Huang et al. [2014a] and Huang et al. [2016] also utilise the RANS equation to solve for stratified combustion in a GDI engine. The first study looked to extend the flame speed closure (FSC) model that is then closed by the Zimont-Lipatnikov turbulent burning velocity model (see section 3.2.5). The extension to the FSC model is a new method for calculating the mean density. The study also introduces a probability density function (PDF) to model the local turbulent fluctuations. This PDF is extended in Huang et al. [2014a], where a Favre averaged and Canonical PDF are compared. The results comparing the effect of the local turbulent fluctuations for both early and late injection strategies is shown in Figure 2.15. The effect of turbulent fluctuations on the in-cylinder pressure case for early fuel injection is negligible. For later fuel injection, where the mixture is likely to be stratified, the in-cylinder pressure traces do show some variation, however any variation is small when compared to the spread of experimental data that occurs due to cyclic variability. A conclusion drawn from Huang et al. [2016] is that the calculated pressure is sensitive to the invoked turbulence model, implying that modelling the spray-turbulence interaction is extremely important and therefore must be included in this project.

Wadekar et al. [2018] uses Large Eddy Simulation (LES) as opposed to RANS

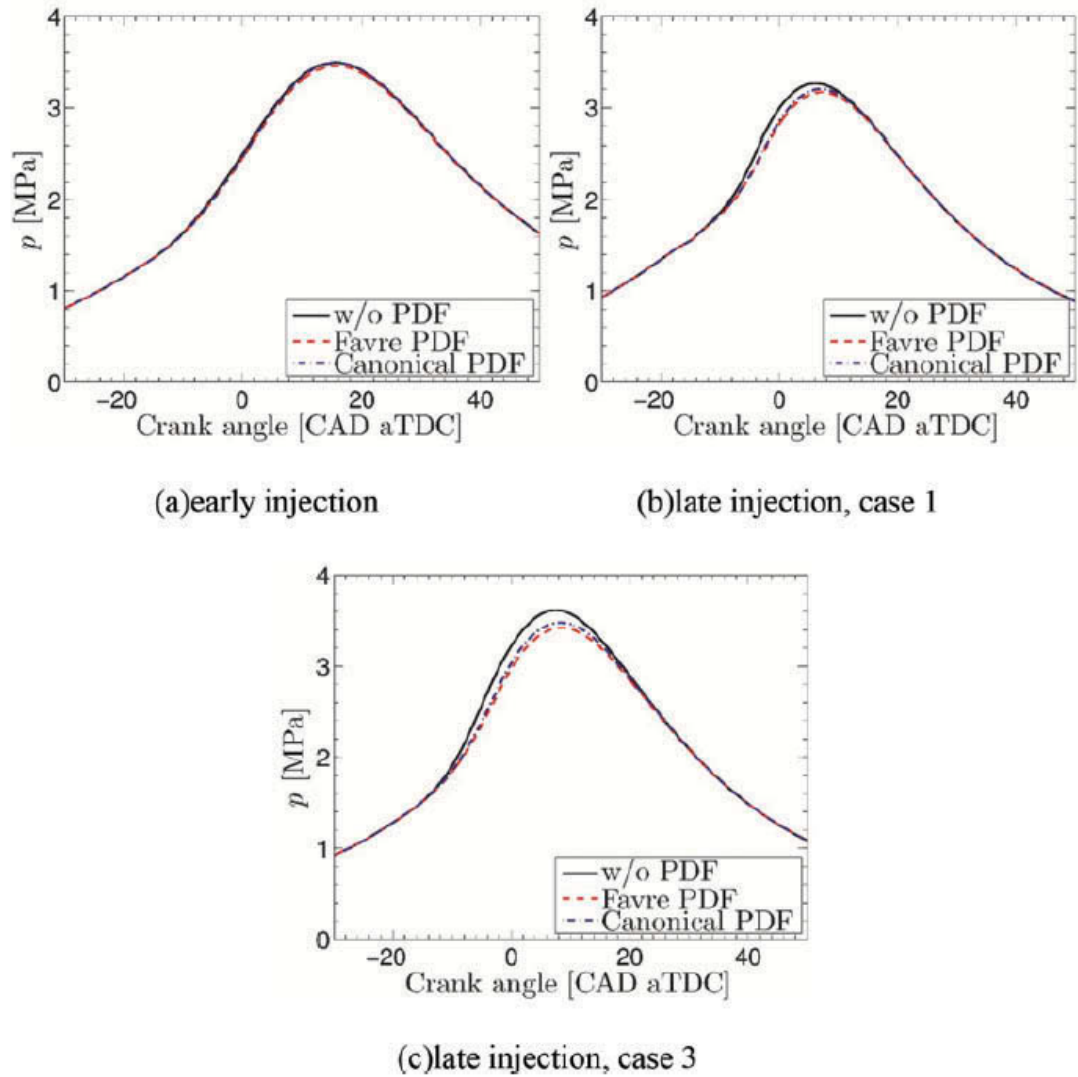


Figure 2.15: In-cylinder pressure curves computed by neglecting turbulent fluctuations in mixture fraction (solid lines) and by invoking the mass-weighted (dashed lines) and canonical (dotted-dashed lines) beta-PDFs for the mixture fraction, taken from Huang et al. [2014a].

simulations that provide ensemble and time-averaged information, which is “unsuitable for studying transient behaviour”. The study showed a reasonable agreement with experimental pressure trace data, although the error increased with engine load. Like the RANS simulations of Huang et al. [2014b,a] and Huang et al. [2016] it was found that the effect of turbulent fluctuations had a relatively large difference on peak pressure traces.

Robeck and Ellzey [1998] investigated a closed boundary combustion event using a 1-D stratified charge. The modelling aim was to replicate the boundary conditions of the experiments carried out by Moriyoshi et al. [1996]. The equivalence ratio profile

had a rich mixture of  $\phi = 1.0$  and a lean mixture of  $\phi = 0.4$  for a propane-air mixture. Under these conditions the flame structure of the stratified case was found to be similar to that of the homogeneous case, thus allowing this study to utilise the pre-existing homogeneous code under certain running conditions. Stronger stratification resulted in greater amounts of unburned mixture and increased levels of CO.

Thermodynamic and quasi-dimensional models of stratified charge engines have also been developed. Abdi Aghdam [2003] tried to develop a stratified charge model in the Leeds University Spark Ignition Engine (LUSIE) code. This included a radially varying equivalence ratio distribution and a term to model the effect of burned gas expansion on these profiles. The effect of the burned gas expansion is further described in section 5.4. Two equivalence ratio profiles were incorporated, a linear and a parabolic function. The model was never validated against experimental data, and as such had not been included in the last 3 versions of the code. Schmid et al. [2009] looked to include a fuel injection and vapourisation model into a quasi-dimensional engine code using a simple mass flow rate equation. The evaporation of the liquid fuel was validated against CFD data showing good agreement. The combustion is modelled using the entrainment approach found in Blizard and Keck [1974], and is also the approach adopted in this thesis. The study by Schmid et al. [2009] states that CFD simulations predict two stages of flame propagation. First the flame is said to propagate spherically before propagating toroidally. This change in propagation is surprising as none of the CFD data found within the literature has suggested that this is the case (Ahmadi-Befrui et al. [1991], Huang et al. [2014a,b], Duclos and Zolver [1998], Huang et al. [2016], Wadekar et al. [2018], Wallesten et al. [2002], Miyagawa et al. [2003]). Although the flame propagation seems odd compared to the other literature, the predicted pressure trace data shows good agreement with experimental data.

A slightly different approach was utilised by Sjeric et al. [2011] who looked to implement a predictive stratified charge model into a fractal combustion model. Fractal models use two zones, a burned and unburned zone, calculating the flame front as a highly wrinkled area. The rate of mass burned is calculated using:

$$\frac{dm_b}{dt} = \rho_u A_T S_l \quad (2.39)$$

where  $S_l$  is the laminar flame speed. The effect of turbulence wrinkling the flame surface is taken into account in the term  $A_T$ . Essentially the fractal model predicts the propagation of a wrinkled laminar flame<sup>4</sup>. The study modelled the charge strat-

---

<sup>4</sup>The wrinkled laminar flame is found within the flamelet regime that is typically associated with SI engine combustion. The different turbulent combustion regimes are described in section

ification by varying the equivalence ratio as a function of mass burned. The model was not validated against any experimental or CFD engine data and has since been coupled with cyclic variability models (Sjeric et al. [2015, 2016]).

Another example of zonal thermodynamic modelling of a stratified charge can be found in the article by Aliramezani et al. [2013], who looked to model a hydrogen-methane blend. Although the paper makes it clear that the equivalence ratio profile should vary radially it fails to disclose any details on how this is achieved. The model found that the trends in indicated mean effective pressure (IMEP) and brake specific fuel consumption (BSFC) agreed well with experiment, however the absolute values showed poor agreement. The use of IMEP as a metric to determine the accuracy of a stratified fuel model is questionable as little in-cylinder combustion information can be gained i.e. the in-cylinder event may look quite different for two cycles with the same IMEP.

## 2.7 Exhaust Gas Recirculation and Residuals

Exhaust gas recirculation involves purposefully reintroducing exhausted combustion products into the combustion chamber through the intake manifold. Residuals on the other hand are combustion products that are left in-cylinder after a firing cycle due to an inability for all combustion products to be exhausted. The advantages and disadvantages of both EGR and residuals are discussed in the following sections.

A review into the literature surrounding the effect of EGR on the laminar burning velocity has led to following summary:

- Only one study has investigated the effect of EGR on the laminar burning velocity close to engine conditions (Middleton et al. [2012]). No validation against experimental engine data was undertaken.
- The effect of EGR on the laminar burning velocity is typically modelled through an EGR correction factor. No EGR correction factor has yet been determined from SI engine data.
- While a couple of studies have used realistic EGR compositions (Marshall et al. [2011], Mannaa et al. [2017]) to study the effect of EGR on the laminar burning velocity, the majority of correction factors are derived using synthetic EGR containing only a small range of species.

### 2.7.1 Residuals

Alger and Wooldridge [2004] investigated the levels of residual gas fraction (RGF) in a SI engine using variable cam timing to alter the intake and exhaust valve overlap and the absolute pressures of the intake manifold. The study found that: the greater the valve overlap the greater the number of residuals, for the same valve overlap a higher manifold absolute pressure will result in lower RGF and for the same valve overlap a retarded intake valve opening time will also lead to a reduction in residuals.

The advantages of including residuals is a reduction of in-cylinder NO<sub>x</sub> production, due to the reduction in air concentration. Cycles with a greater number of residuals have reduced pumping losses. The reduction in residuals is a by-product of the valve timing strategy, where increased overlap leads to reduced pumping losses. Disadvantages of residuals include an increase in HC emissions (Peckham et al. [2011]) and cyclic variation (Finney et al. [2015]).

### 2.7.2 Exhaust Gas Recirculation

Engine manufacturers are constantly having to reduce engine emissions and improve fuel economy to meet government legislation. The latest European legislation (EURO VI) came into effect in 2014 with the focus primarily on the reduction of NO<sub>x</sub> emissions for diesel engines and PN emissions for direct injection gasoline engines. A favourable strategy to meet such regulations is to recirculate cooled exhaust gas into the cylinder.

Typically burned combustion products leave the cylinder through the exhaust valves into the exhaust manifold. The hot exhaust gas is then cooled before reaching the intake system where it then returns to the cylinder. A schematic describing the typical processes of a low pressure EGR loop, where the EGR gas is extracted downstream of the turbine and is introduced upstream of the compressor, is presented in Figure 2.16.

A high pressure EGR loop extracts the EGR gas upstream of the turbine and is reintroduced downstream of the compressor. Takaki et al. [2014] compared both the high pressure and low pressure EGR loops. The study concluded that the low pressure loop was the better system due to its reduction in knocking propensity, due to decreased NO<sub>x</sub> in the intake as the exhaust gas has to pass through the three-way catalyst. The low pressure loop was also found to have greater control when introducing the EGR, as the EGR rate is constant for a given valve opening. However, not all low pressure loops catalyse the exhaust gas and the transient response suffers

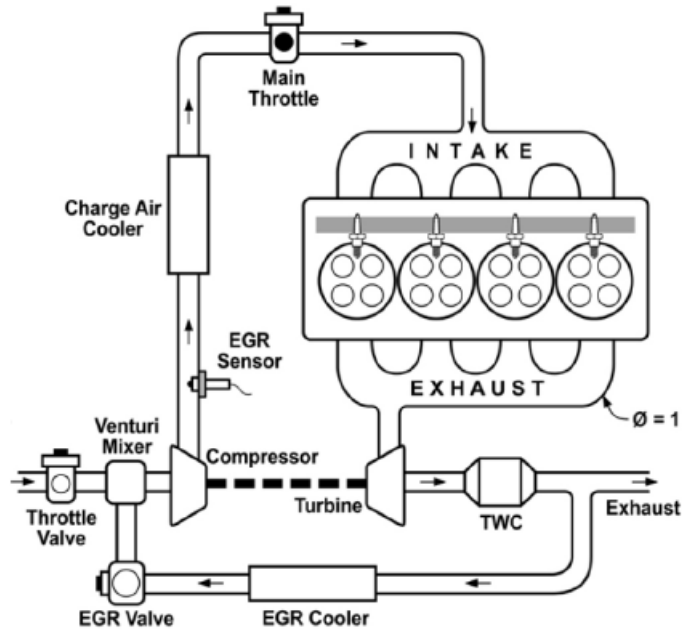


Figure 2.16: Schematic of a low pressure EGR loop for a turbo-charged four cylinder engine, taken from Gukelberger et al. [2015].

when compared to a high pressure loop.

### 2.7.2.1 Effects of EGR on combustion

The effects of EGR on combustion found within the literature can generally be split into two categories, either: engine studies on emissions/efficiency, or the effect that diluting a mixture has on the laminar burning velocity.

Engine studies have found significant improvements in brake specific fuel consumption (BSFC), with Takaki et al. [2014] finding a 5% improvement at 3200 rpm and 1.5 MPa BMEP, for 10% EGR. Alger et al. [2011] found an even greater improvement of up to 13% for the BSFC at a similar engine speed (3500 rpm) and a reduced load (0.96 MPa BMEP). The study by Alger et al. [2011] also found that increasing the levels of EGR reduced NO<sub>x</sub> emissions. Unfortunately a consequence of this is an increase in HC emissions. EGR is not just a viable solution for reducing SI engine emissions but can be applied for other engine operating modes such as controlled autoignition (CAI) i.e. Diesel engines. Cairns et al. [2006] found up to a 10% reduction in CO<sub>2</sub> when EGR was introduced to a CAI engine at part-load conditions. The same study found that at high loads for SI engine operation, EGR resulted in an approximately 30% reduction in NO<sub>x</sub> and up to an 80% reduction in HC and CO emissions when compared to a fuel enrichment strategy, where a richer mixture (greater equivalence ratio) is utilised. It is fairly obvious that the

fuel enrichment strategy would lead to an increase in BSFC compared to EGR, although this is not specifically stated. Not only does recirculating exhaust gas result in NO<sub>x</sub> and CO emission reduction and improve BSFC, it has also been found to reduce the exhaust gas temperature and suppress knocking (Kumano and Yamaoka [2014], Cairns et al. [2008]). The knock suppressant nature of adding cooled exhaust gas to the in-cylinder charge allows for an increased compression ratio, and thus an increased thermal efficiency (Edson [1964]).

The effect of EGR on the laminar burning velocity has been studied using constant volume combustion vessels (Metghalchi and Keck [1982], Rhodes and Keck [1985], Marshall et al. [2011], Galmiche et al. [2012], Mannaa et al. [2017]), heat flux burners (Bhattacharya et al. [2015]) and numerical simulations using chemical kinetics mechanisms (Middleton et al. [2012], Fu et al. [2014], Bhattacharya et al. [2015]), however no studies have been carried out using internal combustion engines. Whilst the work by Metghalchi and Keck [1982], Rhodes and Keck [1985], Fu et al. [2014] and Bhattacharya et al. [2015] explicitly suggest correlations to model the effect of EGR on the laminar burning velocity, this section will describe the general trends. The details of the EGR correlations shall be described in Chapter 4. Only the results of Middleton et al. [2012] were at significant pressure and temperature to replicate engine conditions ( $T_u = 900\text{K}$ ,  $P = 1.5\text{ MPa}$ ).

Metghalchi and Keck [1982], Rhodes and Keck [1985], Marshall et al. [2011], Galmiche et al. [2012], Fu et al. [2014], Bhattacharya et al. [2015] and Mannaa et al. [2017] all conclude that the addition of EGR reduces the laminar burning velocity. This reduction is typically modelled as a correction factor to the laminar burning velocity:

$$\text{EGR correction factor} = \frac{u_l(f)}{u_l(f=0)} \quad (2.40)$$

where  $f$  is the fraction/percentage of EGR. Certain studies have used simulated EGR that is composed of either N<sub>2</sub> or a mixture of N<sub>2</sub> and CO<sub>2</sub>, however Mannaa et al. [2017] concluded that using simulated residuals lead to a greater reduction in laminar flame speed compared to using real EGR. Although these correlations have been suggested in the literature none have been compared under engine conditions to determine which models, if any, can be utilised for a predictive engine model.

There was therefore a need to investigate pre-existing correlations at engine conditions, comparing which is best suited to produce realistic in-cylinder trends, such as crank-resolved pressure profiles and flame radii at increasing levels of EGR. A correlation derived under engine conditions using a real exhaust gas composition

was also included in this comparison.

# Chapter 3

## Combustion code & Engine Description

---

### 3.1 Introduction

Two quasi-dimensional thermodynamic codes for spark ignition engines have been developed at The University of Leeds for the past 30 years. The two codes run in opposite directions, with one predicting pressure traces and combustion parameters for a set of running conditions, with the reverse thermodynamic code calculating combustion parameters from experimental combustion data. These codes are referred to by the acronyms LUSIE (Leeds University Spark Ignition Engine [code]) and LUSIEDA (Leeds University Spark Ignition Engine Data Analysis [code]).

The predictive code originated as an equilibrium cycle code for single and divided chamber engines, developed by Desoky [1981] and Al-Mamar [1983], before the combustion-rate and heat transfer processes were included by Hynes [1986], setting the foundations for the existing LUSIE code. Since then the LUSIE code has been developed significantly, splitting the combustion chamber into multiple zones and including an expression for the flame development. A number of supplementary routines have been included to increase the accuracy of modelling the combustion process. These include accounting for: turbulence, auto-ignition, crevice effects (blow-by), multiple ignition sources and flame geometry (Abdi Aghdam [2003], Hat-trell [2007], Conway [2013], Khan [2014])

This chapter describes the engine combustion codes, LUSIE and LUSIEDA, and the single cylinder research engine used to obtain validation data and combustion

parameters.

## 3.2 LUSIE Simulation Software

### 3.2.1 Overview

The primary application of LUSIE is to predict the thermodynamic processes in two and four-stroke spark ignition engines. The code itself iteratively models the closed part of engine cycle which includes compression, combustion and expansion. The intake and exhaust processes are modelled in terms of inducted mass, with a constant mass flow rate assumed during the intake and exhaust period. The mass flow rate is included to determine the initial conditions for the 0-D  $k$ - $\epsilon$  turbulence model.

LUSIE falls within the category of a thermodynamic code as opposed to a fluid dynamic code. It can be categorised further as a quasi-dimensional model when ran in either the two or three-zone modelling modes (see section 3.2.3.2 and 3.2.3.3). The model is classed as quasi-dimensional rather than zero-dimensional as it separates the burned and unburned gas regions, as opposed to treating the entire charge as a homogeneous mass. The division of the gas into burned and unburned zones allows the code to utilise the flame geometry and apply it to the relevant calculations. When the LUSIE code uses the Wiebe model (see section 3.2.3.1) it becomes 0-D where no attempt is made to physically quantify the physical processes<sup>1</sup> that occur during combustion.

The functionality of the LUSIE code is to separate a ‘real’<sup>2</sup> combustion process into smaller sub-processes that are solved for at discrete time steps. The sum of these sub-processes account for the engine cycle as a whole. Examples of some of these processes include: heat transfer, gas properties such as burned and unburned gas density, burning velocity calculations and adiabatic flame temperature. Although the code solves these processes consecutively, in the actual engine cycle they occur simultaneously.

Recent updates to the code have included a 0-D  $k$ - $\epsilon$  turbulence model and a cyclic variability model (Conway [2013]), as well as a comprehensive kinetic autoignition model (Khan [2014]).

---

<sup>1</sup>Physical processes such as flame propagation, burning velocities and the effect of turbulence are not calculated in 0-D model.

<sup>2</sup>A full account of the numerous thermodynamic, fluid dynamic and dynamic processes occurring within an engine cycle is beyond even the most detailed simulation techniques.

The current version of LUSIE is written in Fortran 90 and is typically compiled with either the Intel or Gfortran compilers. Initially the code was written in Fortran 77 but was migrated to take advantage of the modular programming framework that Fortran 90 offers (Hattrell [2007]). Another advantage is that the potentially problematic ‘COMMON’ statement, which requires careful tracking through large codes, can be avoided. Later versions of Fortran were considered, however it was felt that effort to migrate the code for a second time would far outweigh any benefits the new features provide.

### 3.2.2 Model assumptions

The assumptions in LUSIE are common for all quasi-dimensional models and are summarised below.

- In the two-zone model the reaction front is infinitely thin.
- Gases are ideal and not perfect.
- The process of combustion is the only occurrence of mass transfer between the fresh and burnt gas.
- Heat transfer does not occur between the two zones.
- The pressure within the cylinder is uniform.
- The temperature and chemical composition is homogeneous in each zone.
- The chemical composition of the unburned gas is “frozen”.
- The burnt gas is maintained at a chemical equilibrium.

### 3.2.3 Zonal modelling

LUSIE can be ran in either single or multi-zone modelling modes. The multi-zone models can be divided further into either two or three zone modelling. A schematic for the multi-zonal modelling is shown in Figure 3.1 where  $P_b, T_b, m_b$  is the pressure, temperature and mass of burned gas respectively. The pressure, temperature and mass of the unburned gas is  $P_u, T_u, m_u$  respectively. Finally  $m_e$  is the mass entrained into the flame front,  $u_{tr}$  is the turbulent mass burning velocity and  $u_{te}$  is the entrainment burning velocity. Each of the zonal models is described in the following sections.

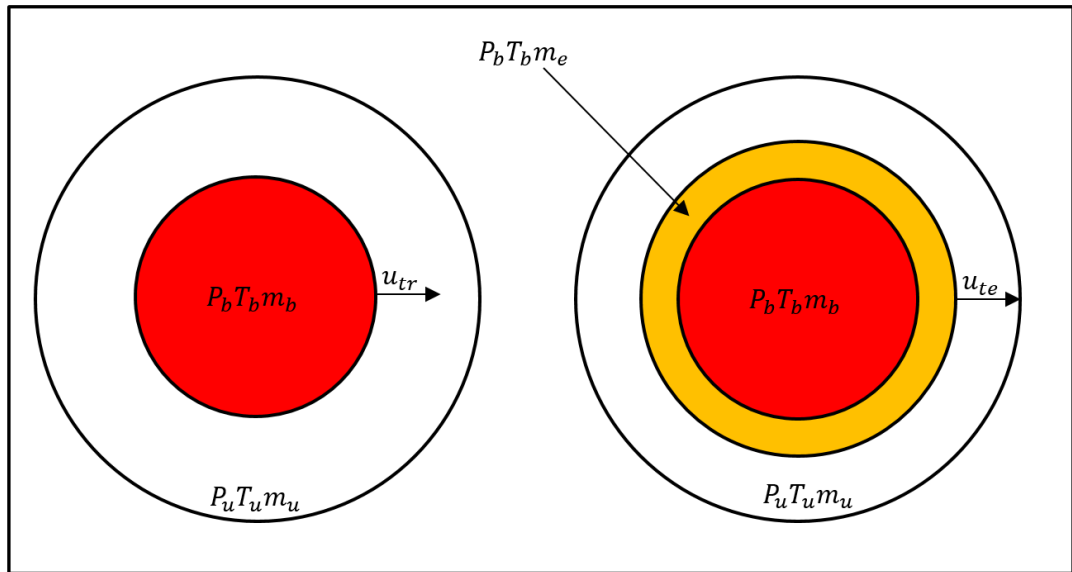


Figure 3.1: Two and Three-zone models including definitions used within LUSIE

### 3.2.3.1 Single zone model

The single zone model is 0-dimensional and does not resolve the physical processes that occur within an engine. Instead the burned mass fraction is calculated with a single function. This function is known as the Wiebe function (Vibe [1964]) and is described by:

$$x_b = 1 - \exp \left[ -a \left( \frac{\theta - \theta_{ign}}{\Delta\theta} \right)^{m+1} \right] \quad (3.1)$$

where  $x_b$  is the cumulative mass fraction burned of the charge,  $\theta_{ign}$  is the start of combustion, and  $\Delta\theta$  is the duration of combustion. The parameters  $a$  and  $m$  are adjustable constants. The function produces an ‘S’ shaped profile typical of the mass fraction burned, however to match experimental data the user defined constants need tuning for each instance. The typical curve profile is shown in Fig. 3.2.

Due to requiring prior knowledge of the burn profile to match experimental results it is worth stating that as a predictive modelling tool this simple approach falls short. However because of its simplicity the computational time is minimal, an advantage that commercial codes such as Ricardo WAVE and AVL Boost™ exploit<sup>3</sup>. The Wiebe function was one of the early modifications incorporated into LUSIE by Hynes [1986]. Although it is still an available option in LUSIE, the multi-zone models are often preferred as they calculate a larger number of combustion parameters, such as turbulent burning velocities and flame surface areas (see sections 3.2.3.2 and

<sup>3</sup>Disclaimer: While the two codes mentioned here utilise these models (see respective websites) they may also include other modelling options and are not necessarily limited to this simple combustion model.

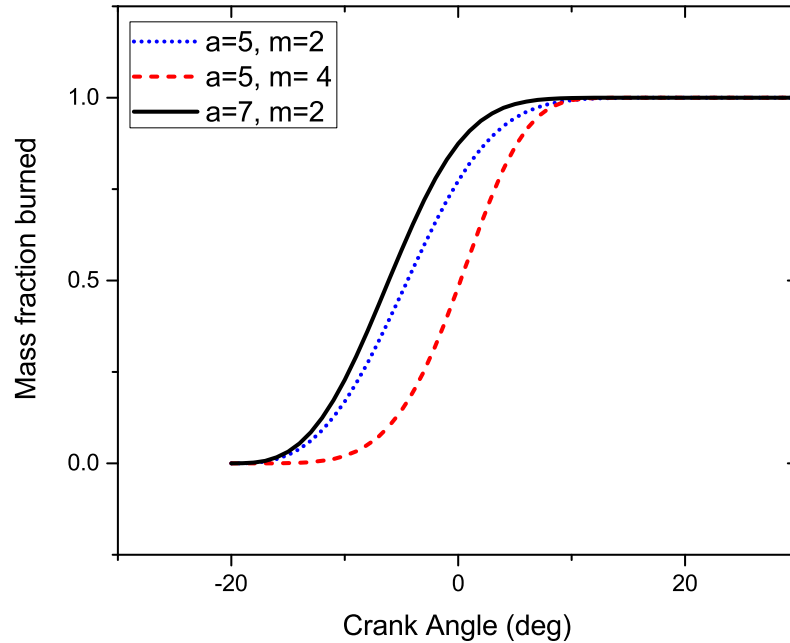


Figure 3.2: Wiebe function of the cumulative mass fraction burned for different values of  $a$  and  $m$ .

3.2.3.3).

### 3.2.3.2 Two-zone model

The two zone model is the simpler multi-zone combustion model dividing the combustion chamber into two zones, one containing the burned gas and the second zone containing the unburned air-fuel mixture. Combustion is modelled as a single rate reaction and as such is heavily reliant on the expression for this rate of combustion. In the two-zone model this rate is given by the turbulent mass burning velocity  $u_{tr}$ . As previously mentioned in the model assumption section (3.2.2), the two-zone modelling assumes that the flame front is infinitely thin between the burned and unburned zones, as such an account of the physical properties of the flame itself is not made. The rate of fuel burned at a given time step,  $\Delta m_b$ , is given by:

$$\Delta m_b = \rho_u A_{fr} u_{tr} \quad (3.2)$$

where  $\rho_u$  is the unburned gas density and  $A_{fr}$  is the surface area of the burned gas zone. The turbulent mass burning velocity,  $u_{tr}$ , is calculated using a turbulent burning velocity model (see section 3.2.5).

### 3.2.3.3 Three-zone model

The three-zone model is an extension to the two-zone model which incorporates some of the physical processes of the flame. The model is based on the work by Blizard and Keck [1974]. The three-zone model distinguishes between the burned and unburned gas as before, further separated by a third zone. The bounds of the third zone are the entrainment radius and the burnt gas radius. Blizard and Keck [1974] proposed that the mass is entrained by the flame before being burnt. This assumed that the individual eddies of a fuel-air mixture are brought into the propagating flame which propagates at the rate  $u_{te}$ , also known as the entrainment burning velocity. This introduces a flame of finite thickness,  $\delta_t$ , to describe the physical process of the flame. Physically, the entrainment radius is the flame front determined from optical experiments as opposed to the burned gas front, which is typically determined from pressure traces (Gillespie et al. [2000]). The mass entrainment rate for a given time step is:

$$\Delta m_e = \rho_u A_{fe} u_{te} \quad (3.3)$$

After the mass is entrained it is then burned. The rate at which the mass is burned is controlled by the characteristic burn-up time,  $\tau_b$ . The rate at which the gas is burned for a given time-step is:

$$\frac{dm_b}{dt} = \frac{m_e - m_b}{\tau_b} \quad (3.4)$$

The characteristic burn-up time is given by:

$$\tau_b = C_{\tau_b} \frac{l_e}{u_l} \quad (3.5)$$

Where  $l_e$  is the size of the turbulent eddy,  $u_l$  is the laminar burning velocity and  $C_{\tau_b}$  is a constant. The choice of eddy size for Eq. (3.5) has been hotly debated in the combustion community. When the model was originally proposed it used a length scale that varied with valve lift, this was later adapted to use the integral length scale as the characteristic eddy size by Keck et al. [1987]. Research at The University of Leeds has previously used both the integral length scale (Hattrell [2007], Abdi Aghdam [2003]) and the Taylor scale (Conway [2013]). It was concluded from the work by Conway [2013] that using the Taylor scale gave the best prediction for the JLR engine geometries. The engine geometry used in the study by Conway is of a similar geometry and bulk turbulent motion to that of the AJ20-P4 engine used in this study. Due to these similarities the Taylor micro-scale was utilised in this study as the characteristic eddy size.

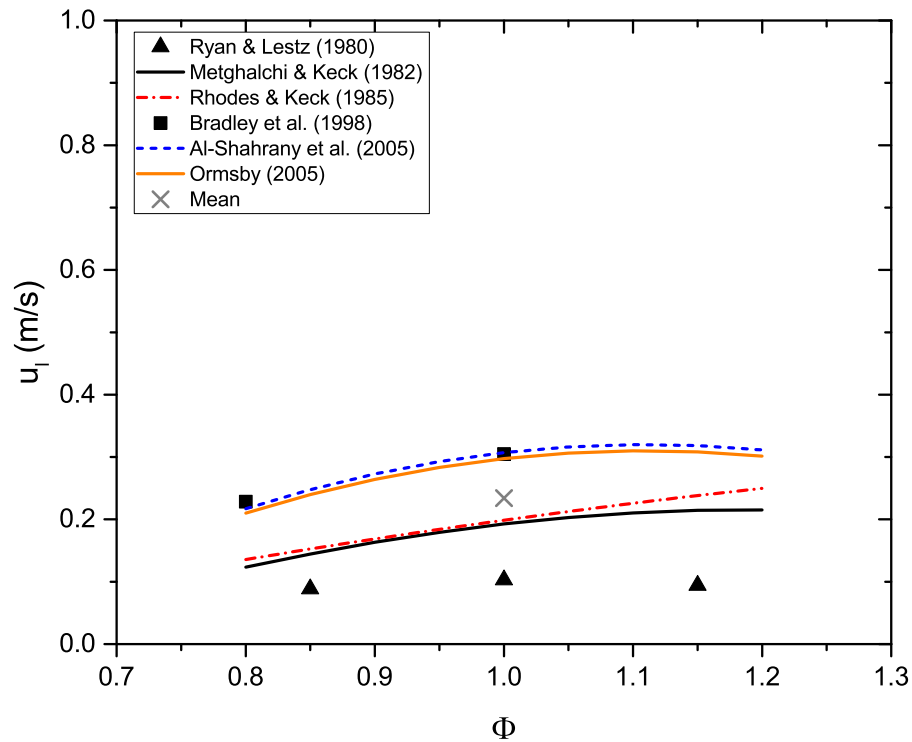


Figure 3.3: Comparison of laminar burning velocity models at varying equivalence ratio at pressure 5 bar and temperature 360 K.

### 3.2.4 Laminar burning velocity

The unstretched laminar burning velocity,  $u_l$ , is used in both zonal models for the calculation of the turbulent burning velocity as well as being used in Eq. (3.5) to control the rate of mass burn in the three-zone model. A number of studies using various fuels, techniques, and running conditions have been undertaken to determine unstretched laminar burning velocity correlations (Ryan and Lestz [1980], Metghalchi and Keck [1982], Rhodes and Keck [1985], Müller et al. [1997], Bradley et al. [1998], Al-Shahrany et al. [2005], Ormsby [2005]). These correlations are compared in Figs. 3.3 and 3.4 at both relatively low pressures and temperatures, and “engine like” conditions respectively.

Obtaining laminar burning velocities at “engine like” conditions is difficult experimentally due to relatively high pressures found within engines. At high pressures the Markstein number will become low (Bradley et al. [1998, 2009]) as it was found by Gillespie et al. [2000] that the laminar burning velocity was more susceptible to instability and cellularity. A number of the models extrapolated beyond experimental data to the temperature and pressure are presented in Fig. 3.4. Comparing the two figures shows that for the low temperature and low pressure case there is a much smaller relative difference between the models than at the high pressures and

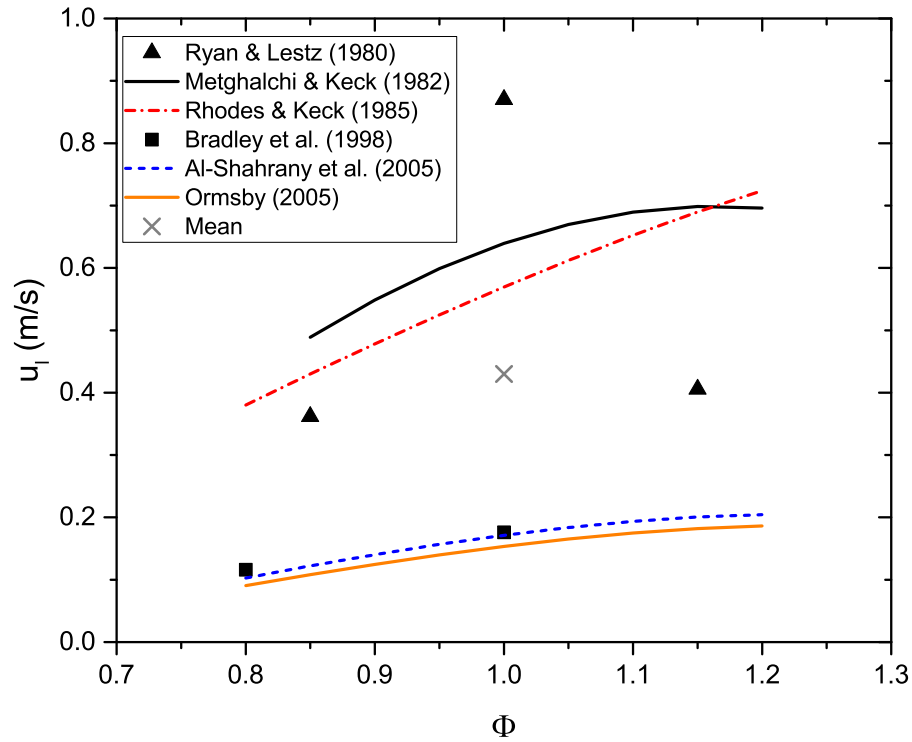


Figure 3.4: Comparison of laminar burning velocity models at varying equivalence ratio at pressure 35 bar and temperature 600 K.

temperatures associated with engines. The choice of model under engine conditions is therefore important to ensure accurate laminar burning velocities are predicted.

Hattrell [2007] investigated the validity of the aforementioned laminar burning velocity models, with no recommendation made on the most suitable model. Conway [2013] and Khan [2014] both used the Metghalchi and Keck [1982] model as the correlation was determined at pressures up to 50 atm and unburned gas temperatures up to 700K. However the model used pressure trace data, rather than optical data, meaning that it was impossible to tell if the laminar burning velocity was enhanced due to cellularity at high pressures. This study uses the Rhodes and Keck [1985] model. Although this correlation also uses pressure trace data, at  $\phi = 1$ , the model is the closest to the mean of all the available correlations for both low pressures and temperatures and “engine like” conditions. Another advantage is that the Rhodes and Keck [1985] model was determined using gasoline. The Rhodes and Keck [1985] model is described by:

$$u_{l0} = B_m + B_\phi \cdot (\phi - \phi_m)^2 \quad (3.6)$$

$$u_l(T, P) = u_{l0} \cdot \left(\frac{T}{T_0}\right)^\alpha \cdot \left(\frac{P}{P_0}\right)^\beta \quad (3.7)$$

For which the coefficients can be found in Table 3.1.

Table 3.1: Coefficients for Rhodes and Keck [1985] laminar burning velocity model.

| $\alpha$                 | $\beta$                    | $\phi_m$ | $B_m$ | $B_\phi$ | $T_0$ (K) | $P_0$ (atm) |
|--------------------------|----------------------------|----------|-------|----------|-----------|-------------|
| $2.4 - 0.271\phi^{3.51}$ | $-0.357 + 0.14\phi^{2.27}$ | 1.21     | 30.5  | -54.9    | 298       | 1           |

While the Rhodes and Keck [1985] model was developed using a type of gasoline, the composition of that gasoline will differ from modern day fuels. The addition of a set percentage of ethanol is typically required for fuels to meet current legislation. The effects of increased amounts of ethanol on the laminar burning velocity are therefore of importance. Compared in Figure 3.5 is the laminar burning velocity of a TRF blend that consists of 75.4% Toluene, 18.7% n-Heptane and 5.8% iso-octane (by liquid volume), at different pressures with increasing levels of ethanol (E0 =0% ethanol, E25 =25% ethanol, E50 = 50% ethanol, E100 = 100% ethanol).  $\Delta u_l$  is

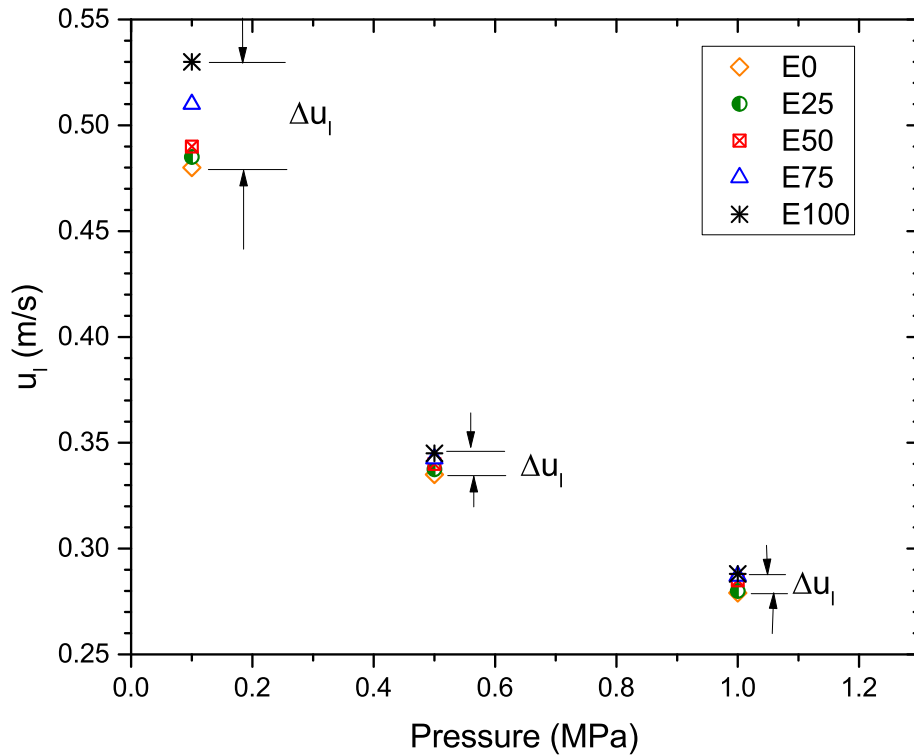


Figure 3.5: Laminar burning velocity for TRF gasoline surrogate with added ethanol at various pressures and  $T_u = 360\text{K}$ . Data taken from Mumby [2016].

the difference between the maximum and minimum laminar burning velocity of the different fuel compositions at each pressure interval. As the pressure increases the difference in laminar burning velocities is reduced, and at 1.0 MPa the difference in laminar burning velocity due to the effect of added ethanol is small. Due to engine combustion being at pressures typically equal to or greater than 1.0 MPa

the existing laminar burning velocity model for gasoline does not need updating to account for the inclusion of ethanol.

It is well established that diluting the mixture with EGR reduces the laminar burning velocity. LUSIE originally accounted for the dilution using either the expression by Metghalchi and Keck [1982] or Rhodes and Keck [1985]. However, due to the nature of fuels evolving and the possible cellularity associated with these correlations, a further two correlations were programmed into LUSIE by the author (Fu et al. [2014], Bhattacharya et al. [2015]). A novel approach to determine an EGR correction factor model from experimental engine data was adopted for this study. The engine data correlation has been compared to pre-existing correlations from the literature, none of which have been derived from engine data. The results from the investigation form Chapter 4 of this thesis.

### 3.2.5 Turbulent burning velocity

Unlike the laminar burning velocity, the turbulent burning velocity,  $u_t$ , is not a fundamental property of the mixture. The turbulent burning velocity also depends on the flow properties. LUSIE has a number of user defined models to calculate the turbulent burning velocity. The models available include the Leeds K and K-Le model developed by Abdel-Gayed et al. [1987] and Bradley et al. [1992] respectively, and the Zimont-Lipatnikov model (Lipatnikov and Chomiak [1997]). The Zimont-Lipatnikov model is a modified version of the original model suggested by Zimont [1979]. The modification includes a time based flame development factor and an additional laminar burning velocity term to account for the turbulence approaching zero. A comparison of these turbulent burning velocity models was made by Abdi Aghdam [2003] during his doctoral studies. It was concluded for variations in compression or equivalence ratio that the Zimont-Lipatnikov model was superior to the K or K-Le model, however predictions from all three were comparable at different engine speeds. For this reason the Zimont-Lipatnikov model is adopted for the present study. This choice is supported by Lipatnikov and Chomiak [2002], who analysed experimental  $u_t$  databases and found that the turbulent burning velocity is proportional to both the turbulent RMS velocity and Damköhler number. The study found that only four published models could predict all of the experimental trends observed in turbulent flame propagation. These four models were: the expression due to Zimont [1979], an expression based on the G-equation developed by Peters [1999], the coherent flame model by Duclos et al. [1993], and the pair exchange model by Kerstein [1988]. Another supporting argument for choosing the Zimont-Lipatnikov model is its recent use for modelling fuel stratification (Lipatnikov [2017]),

Huang et al. [2014a,b]) which forms a large part of this thesis.

Recent studies by Bradley et al. [2011] and Bradley et al. [2013] have suggested a new correlation that is similar to the expression suggested by Zimont [1979]. The new correlation is of the form:

$$\frac{u_t}{u'_k} = U = \alpha \cdot K^\beta \quad (3.8)$$

for positive Markstein numbers:

$$\alpha = 0.023(30 - \text{Ma}_{sr}) \quad (3.9a)$$

$$\beta = 0.0103(\text{Ma}_{sr} - 30) \quad (3.9b)$$

whereas for negative Markstein numbers:

$$\alpha = 0.085(7 - \text{Ma}_{sr}) \quad (3.10a)$$

$$\beta = -0.0075(\text{Ma}_{sr} + 30). \quad (3.10b)$$

The correlation was determined experimentally for a number of different fuels at various pressures and temperatures. The Karlovitz stretch factor is related to the Damköhler number by:

$$\text{Da} = K^{-1} \frac{L}{\lambda} \quad (3.11)$$

meaning that the model is comparable to those analysed by Lipatnikov and Chomiak [2002], and improves on this by physically constraining the constant  $\beta$ . The stretch rate Markstein number,  $\text{Ma}_{sr}$ , depends on mixture composition (fuel type, equivalence ratio and residuals), pressure and temperature. Unfortunately not enough information is currently published for the mixtures, pressures and temperatures which this study investigates. A plot of the Zimont model is compared to the newly suggested U/K correlation in Figure. 3.6.

Zimont [1979] proposed that the mechanism of turbulence effects on the turbulent burning velocity can be treated based on eddy size. The model assumed that large-scale turbulent eddies increase the burn rate by wrinkling the flamelet, thus increasing the area of the flame. Another assumption was that the small-scale turbulent eddies, on a scale smaller than the flame thickness ( $\eta < \delta_t$ ), penetrate the flame front and thicken it, enhancing the mixture and also increasing the burn rate. The turbulent burning velocity of a flame surface element is therefore given by the product of a local quasi-laminar burning velocity of a thickened flamelet, and the ratio of the wrinkled surface area of the thickened flamelet,  $u_{n,t}$ , to the projected

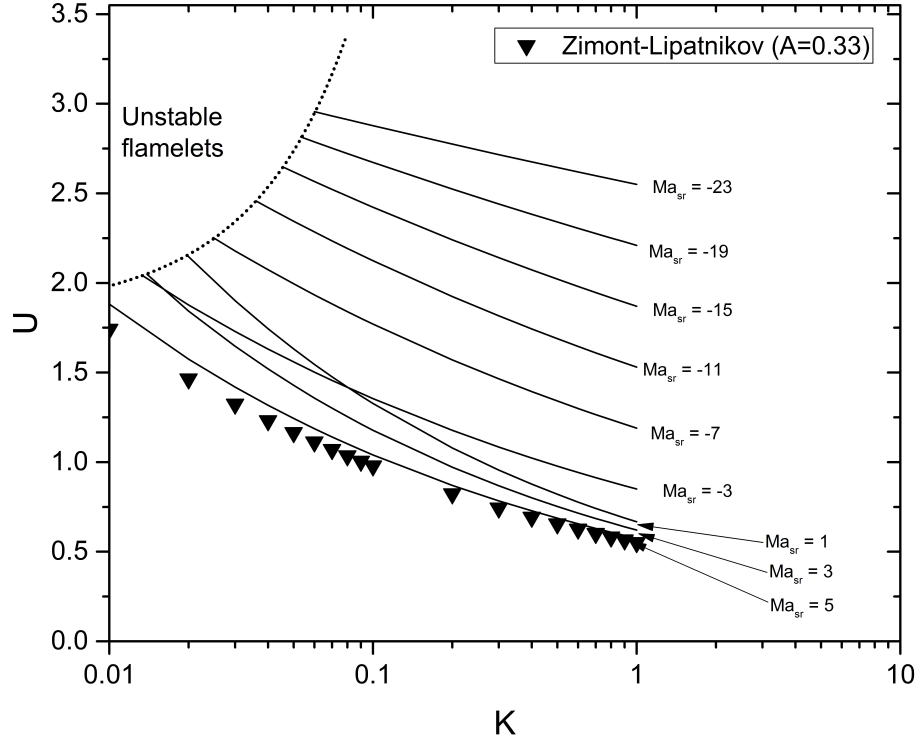


Figure 3.6: U/K diagram with Zimont-Lipatnikov model plotted.

surface area normal to the direction of propagation:

$$u_{t,\infty} = u_{n,t} \left( \frac{\bar{A}_t}{A_0} \right) \quad (3.12)$$

where  $A_t$  is the surface area of the thickened flame, and  $A_0$  is the area of the projection of this surface onto a plane normal to the direction of propagation. Zimont's assumptions result in a fully developed flame as the ratio  $\bar{A}_t/A_0$  is assumed to be independent of the flame development time. The fully developed turbulent burning velocity was expressed as:

$$u_{t,\infty} = C_{ut} u' Da^{1/4} \quad (3.13)$$

where  $u'$  is the turbulent RMS velocity. As well as the definition in Eq.(2.36) the Damköhler number can be defined as:

$$Da = \frac{L u_l^2}{u' \kappa} \quad (3.14)$$

where  $L$  is the integral length scale,  $\kappa$  is the thermal diffusivity and  $u_l$  is the unstretched laminar burning velocity. Therefore the fully developed turbulent burning velocity can be expressed in terms of the laminar burning velocity.

$$u_{t,\infty} = C_{ut} u'^{3/4} u_l^{1/2} L^{1/4} \kappa^{-1/4}. \quad (3.15)$$

The proportionality constant,  $C_{ut}$ , has traditionally required tuning depending on whether it is the two-zone or three-zone model being used (Abdi Aghdam [2003]). For the two-zone model the velocity is the turbulent mass burning velocity,  $u_{tr}$ , as originally intended by Zimont, whereas for the three-zone model it represents the turbulent entrainment velocity,  $u_{te}$ . An attempt has been made to align  $C_{ut}$  for both two and three zone models through the inclusion of a density ratio term to capture the thermal expansion effects of the flame. This saves time tuning constants when switching between two and three-zone combustion models.

$$u_{t,\infty} = C_{ut} u' \text{Da}^{1/4} \left( \frac{\rho_u}{\rho_b} \right) \quad (3.16)$$

Conway [2013] reported that a value of 0.35 for  $C_{ut}$  was reasonable for various naturally aspirated and turbo-charged engines. It was then adopted in the study by Khan [2014] and has again been adopted for this study.

Lipatnikov and Chomiak [1997] developed an expression for the developing turbulent burning velocity,  $u_t$ , to account for the fact that in a real engine the flame is not statistically stationary. The flame accelerates and the flame brush thickens as the flame front experiences different eddy sizes within the chamber. The flame development can be separated into two categories:

- When the unconstrained flame propagates into the unburned mixture it is largely governed by the turbulence scales encountered.
- When the flame approaches the system boundary, in the case of an engine, the piston, cylinder walls and cylinder head components.

The transient effects of the progressing flame are accounted for in the turbulent burning velocity model, with  $f_d$  modelling the unconstrained flame development and  $f_w$  modelling the flame wall interaction.

$$u_t = (u_l + u_{t,\infty} f_d) f_w \quad (3.17)$$

The extra laminar burning velocity term,  $u_l$ , was included by Lipatnikov and Chomiak [1997] to account for zero turbulence. A detailed discussion on how  $f_d$  and  $f_w$  are modelled can be found in sections 3.2.6 and 3.2.7 respectively.

### 3.2.6 Turbulent flame acceleration

Combustion within a SI engine is a transient process, which starts with a “laminar-like” flame kernel after ignition. The flame front is then wrinkled as it is subjected

to varying sizes of turbulent eddies, increasing surface area and resulting in an acceleration in the propagation velocity. The rate at which the flame front entrains across the combustion chamber is not necessarily aligned with the rate at which fuel burns, therefore the thickness of the flame brush is also a transient phenomena (Abdel-Gayed et al. [1987], Lipatnikov and Chomiak [2002], Ormsby [2005], Larsson [2009]).

Modelling the flame acceleration is particularly important when using quasi-dimensional modelling techniques to simulate SI engine combustion. To account for this behaviour the turbulent burning velocity model, Eq. (3.17), includes the term  $f_d$  to encapsulate the flame acceleration. The term can be interpreted as either being a multiplier to  $u_{t,\infty}$  or a ratio of effective turbulent RMS velocity divided by the actual RMS velocity,  $u'_k/u'$ .

A number of expressions to account for the development of flames in engines can be found in both LUSIE and the literature. Two of the models were developed at the University of Leeds and were based on experimental results by Abdel-Gayed et al. [1987] (time based model) and Scott [1992] (flame radius based model). Another four models were included by Hattrell [2007], three based on a literature review and one suggested by the author. The three models identified in the literature were the work of Wu et al. [1993], Dai et al. [1995] and Lipatnikov and Chomiak [1997]. Hattrell [2007] concluded that the Leeds based models and the Lipatnikov model produced similar trends, whilst the Dai and Wu models appear to over-predict the flame development in the early stages and go on to predict an infinitely accelerating flame, unless met by an infinitely increasing length scale. The model suggested by Hattrell is based on time and the dimensionless flame radius however, although the model is included in LUSIE, it has not been validated against any experimental data. The choice of model for the current study was the Lipatnikov model as it has been purposefully developed as an extension of the Zimont turbulent burning velocity model also chosen for this study.

The flame development factor proposed by Lipatnikov and Chomiak [1997] is based upon the time elapsed from spark,  $t$ , and is given by:

$$f_d = \left\{ 1 + \frac{\tau_L}{t} \left[ \exp\left( -\frac{t}{\tau_L} \right) - 1 \right] \right\}^{1/2} \quad (3.18)$$

where  $\tau_L$  is the turbulent time scale. Although the Lipatnikov model produces a decreasing flame acceleration it does not account for the deceleration experienced by the flame as it approaches the cylinder walls.

### 3.2.7 Flame-wall interaction

As the flame approaches the wall it decelerates. The deceleration is caused by a physiochemical phenomena that is difficult to measure even in full bore optical access engines due to the light reflecting off the cylinder walls. As the flame approaches the walls heat loss from the flame is increased, thus lowering reactant temperature, decreasing reaction rates. The wrinkled flame becomes truncated by the cylinder walls, reducing the surface area of the flame leading to a decrease in the propagation velocity. The flame extinguishes due to exhaustion of reactants, or radical termination at the walls (Verhelst and Sheppard [2009]).

The effect of the flame-wall interaction is encapsulated into the turbulent burning velocity model in Eq.(3.17) through the term  $f_w$ . There are two flame-wall interaction models within LUSIE, the first is based on a “Active” Perimeter Fraction (APF) developed by Abdi Aghdam [2003] and the second is based on the model by Lipatnikov and Chomiak [2000]. This was then converted to engine co-ordinates by Abdi Aghdam et al. [2007]. The second model has been the preference of the previous users of LUSIE (Conway [2013], Khan [2014]), and shall be described here. It must however be noted that upon comparison by the author, the models had a negligible difference on the predictive pressure traces, which are presented in Figure 3.7.

The flame-wall factor,  $f_w$ , for the Lipatnikov/Aghdam *et al.* model was based on experimental observations and is defined as:

$$f_w = \operatorname{erf}\left(\frac{r_b - f_{re}}{\delta_t(t)}\right) \quad (3.19)$$

where  $r_b$  is the bore radius,  $f_{re}$  is the flame radius and  $\delta_t$  is the flame thickness. The flame thickness is governed by diffusion and is given by Lipatnikov and Chomiak [2000] as:

$$\delta_t(t) = u' \tau_L \left\{ 2t' \left[ 1 - \frac{1}{t'} (1 - e^{-t'}) \right] \right\}^{1/2} \quad (3.20)$$

where  $t'$  is a dimensionless time given by  $t/\tau_L$ .

### 3.2.8 Flame geometry

The Generalised GEOMetry lookup table (GGEOM) is a stand alone command line application, which was created by Hattrell [2009]. The software creates flame lookup tables to be used by LUSIE. The flame lookup tables provide flame volumes

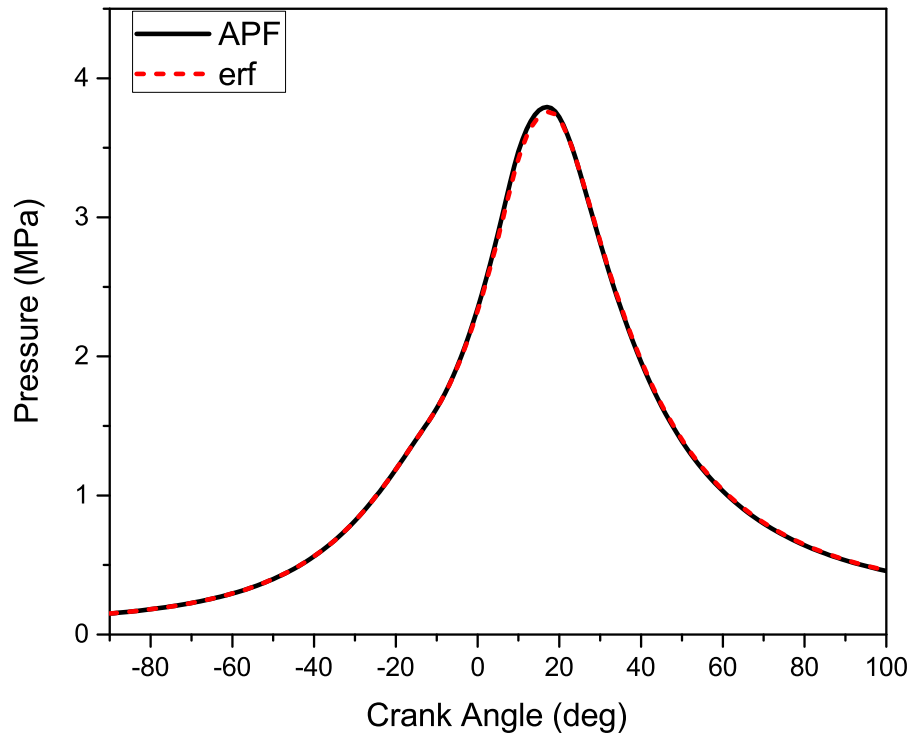


Figure 3.7: LUSIE pressure trace simulations for APF model developed by Abdi Aghdam [2003] and error function model proposed by Lipatnikov and Chomiak [2000], under arbitrary running conditions.

and areas, for a given flame radius, at a given discrete crank angle. There may be more than one flame geometry for any given crank angle due to the variations in combustion rate and the point of ignition. An assumption made by GGEOM is that the flame propagates as a sphere and is truncated by the cylinder walls.

The use of GGEOM allows actual engine geometry to be used, as opposed to idealised pent and disc shaped geometry. It incorporates CAD models of the engine geometry through the use of the GNU triangulated surface library. STereoLithography (STL) CAD files of the top surface of the piston and the cylinder head surface are easily converted into GNU Triangulated Surface (gts) files by invoking a single command in the terminal. GGEOM uses these geometries to create the flame lookup table. The flame geometry can be shown visually, an example of this is Figure 3.8, which shows the different flame radii at a given crank angle.

### 3.2.9 Heat transfer

Heat transfer in an engine strongly effects the combustion process (Ferguson and Kirkpatrick [2001]) with the dominant mode of heat transfer for a SI engine, between the combustion gases and cylinder walls, being convection. Two expressions

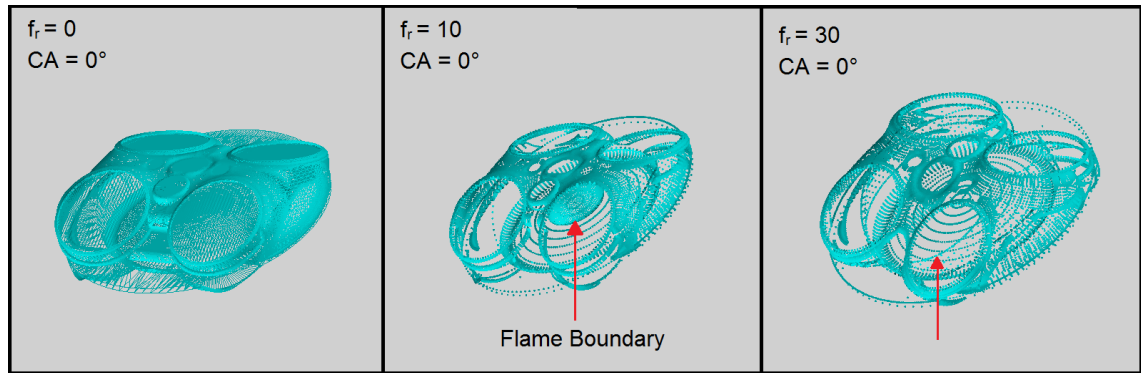


Figure 3.8: Visual output of GGEOM showing the Jaguar Land Rover single cylinder research engine geometry and flame radius for a given crank angle.

for predicting the heat transfer are programmed into LUSIE with both models based on Nusselt-Reynolds relations, which originate from turbulent flow in pipes. The two heat transfer correlations are the Annand [1963] model, which includes both convective and radiative terms, and the Woschni [1967] model which accounts for convection only. The models are reliant on the wetted surface areas of the combustion chamber, which changes with piston motion. These wetted surface areas are calculated using the flame geometry routines (see section 3.2.8). Another important parameter for the heat transfer routines are the temperatures of the cylinder head, piston and cylinder walls. Further details for the heat transfer routines can be found in Abdi Aghdam [2003], Liu [2004] and Hattrell [2007].

### 3.2.10 Blow-by

During both firing and motoring cycles the motion of the piston creates a pressure difference between the combustion chamber and the crankcase. The low pressure region is the crankcase which the mass inside the cylinder moves towards. This process for the most part is preventable in an engine due to the inclusion of piston rings which forms a seal between the combustion chamber and crankcase. However the seal is not perfect due to the need for lubricating the reciprocating engine parts to reduce wear. The small gap is enough for some of the mass from the combustion chamber to flow into the crankcase, this is known as blow-by.

Blow-by can be further divided into two categories, mass that escapes but is reintroduced on the expansion stroke of the engine, and mass that is lost to the crankcase. LUSIE makes several assumptions regarding the blow-by, these are:

- flow is isentropic and compressible

- the mass lost is considered to be unburned gas only.

The second assumption is valid for all cases for which the engine uses a centrally mounted spark-plug. The blow-by routines were incorporated into LUSIE by Abdi Aghdam [2003] whose thesis (and in the thesis by Hattrell [2007]), provides a detailed description of the blow-by routines.

### 3.2.11 Turbulence

The flow of the incoming gas at sensible engine speeds enters the combustion chamber at high velocities and is therefore in the turbulent regime. Turbulence is responsible for increasing the burning velocity to much greater values than a laminar system would be capable of, producing a greater rate of heat release. The importance of turbulence on SI combustion is well understood and is included in equations that govern the burning velocity, rate of fuel burned and flame development. LUSIE contains a number of turbulence sub models, including two with linear fit relationships and a 0-D  $k-\varepsilon$  model proposed by Lumley [1999]. A full description of these models can be found in Conway [2013].

LUSIE also allows for an external data file to be parsed in, which can include either experimental or CFD data. Turbulence parameters were determined using CFD before being parsed into LUSIE from the aforementioned external file. The turbulence parameters (crank resolved integral length scale and turbulent RMS velocity) were generated using CFD simulations at Imperial College London. The simulations of the Jaguar Land Rover Single Cylinder Research Engine (SCRE) were undertaken using the commercial STAR-CD/es-ice code. The code was used to simulate gas exchange and in-cylinder flow motion. The model consisted of 2.2 million cells at bottom dead centre (BDC) including the intake and exhaust ports. Time dependent pressure and constant temperature were applied at the intake and exhaust boundaries of the model for each operating point taken from the experimental data. The base timestep used for the simulations was  $0.05 \text{ CA}^\circ$  which was reduced by half during the opening and closing of the valves. Turbulence was modelled using the  $k-\varepsilon$  RNG model proposed and developed by Yakhot and Orszag [1986] and Yakhot et al. [1992]. The turbulence parameters provided for this study were timestep resolved. The complete methodology was validated using an extensive experimental database from an old specification Jaguar Land Rover AJ133 optical engine (Justham et al. [2006], Jarvis et al. [2006], Serras-Pereira et al. [2008, 2015], Williams et al. [2008, 2010], Serras-Pereira et al. [2013]) and the thermodynamic SCRE used in the current study, both of which have a comparable engine geometry.

Validation of the turbulence modelling is included in the thesis by Kountouriotis [2017] and has been utilised in the publication by Roberts et al. [2018]. An example of the CFD generated crank-resolved turbulence parameters are shown in Figure 3.9.

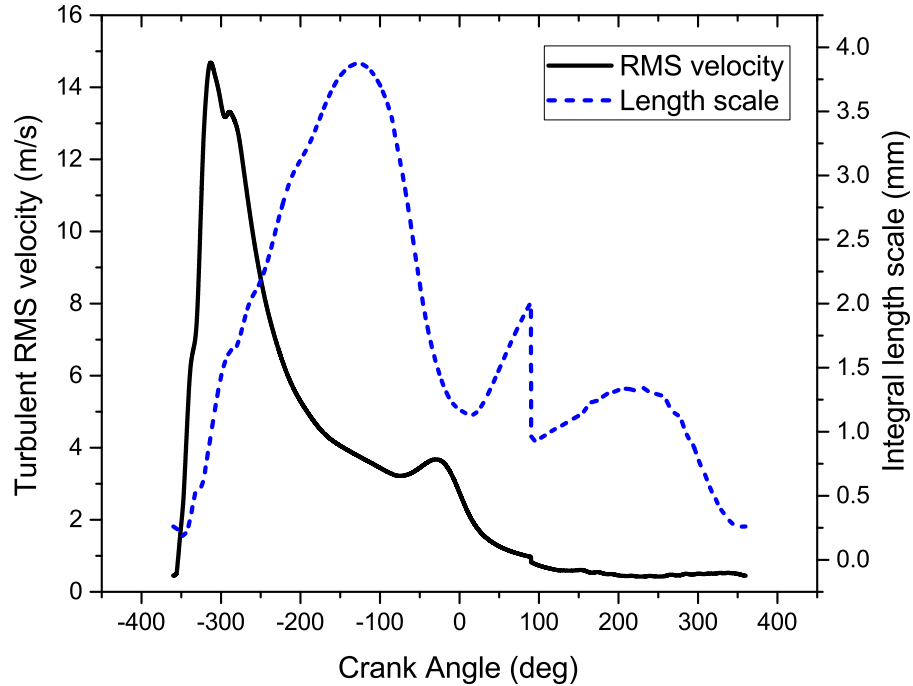


Figure 3.9: Crank resolved turbulent RMS velocity and integral length scale generated using CFD

### 3.3 LUSIEDA Reverse Analysis

LUSIEDA is a reverse thermodynamic code that back calculates combustion parameters, such as the mass fraction burned, turbulent mass burning velocity and burned gas radius, from experimentally obtained in-cylinder engine pressure data.

LUSIEDA calculates the pressure rise inside the combustion chamber incrementally during combustion:

$$P_{i+1} = P_i + \Delta P_m + \Delta P_{ht} + \Delta P_{bb} + \Delta P_{comb} \quad (3.21)$$

where  $P_i$  and  $P_{i+1}$  are experimental pressure data at two consecutive crank angles. The change in pressure due to isentropic compression/expansion is  $\Delta P_m$ .  $\Delta P_{ht}$  is the change in pressure due to heat transfer,  $\Delta P_{bb}$  is the change in pressure due to blow-by, and finally  $\Delta P_{comb}$  is the change in pressure due to combustion. The

heat transfer and blow-by is calculated using either of the heat transfer models found in section 3.2.9 and a “flow through orifice” model by Heywood [1988] (see section 3.2.10) respectively. An iterative method is used to determine the change in mass burned,  $\Delta m_b$ , required for  $\Delta P_{comb}$  to equal the measured value found from Eq. (3.21). The change in mass burned can then be used to calculate the turbulent mass burning velocity from Eq. (3.2). The reverse analysis approach adopted here has been widely used in engine modelling (Liu et al. [2013], Abdi Aghdam [2003], Conte and Boulouchos [2005], Verhelst and Sheppard [2009]).

### 3.4 SI combustion code validation

LUSIE has previously been validated for a wide range of engines at various running conditions, with the most recent validations found in Abdi Aghdam [2003], Hattrell [2007], Conway [2013] and Khan [2014]. The code has been validated here for both the motoring cycle and firing cycle to ensure that LUSIE is still valid for the latest development engines. Unfortunately the single cylinder research engine (SCRE) used for this study (see section 3.5) has no optical access, resulting in no validation for how the flame radius changes w.r.t time. The running conditions for both motoring and firing validation are presented in Table 3.2.

Table 3.2: Running conditions for LUSIE validation.

| <b>Parameter</b>         | <b>Value</b> |
|--------------------------|--------------|
| Engine Speed [rpm]       | 1500         |
| $P_{int}$ [MPa]          | 0.135        |
| $T_{int}$ [K]            | 382.0        |
| Spark advance [deg aTDC] | - 15.0       |
| $\phi$                   | 1.0          |
| Engine Load (GMEP) [MPa] | 0.79         |

#### 3.4.1 Motoring cycle validation

The motoring cycle is validated to ensure that LUSIE can accurately predict the pressure rise due to isentropic compression/expansion, and the effect blow-by has on said pressure trace. The blow-by parameters required updating to match those of the engine. These parameters were taken from measurements found in technical drawings provided by Jaguar Land Rover. The motoring cycle validation is presented in Figure 3.10. The motoring cycle has a good agreement with the compression part of the experimental firing cycle. The good alignment shows that the blow-by and

heat transfer routines are valid for the compression and expansion phases of the cycle. It also confirms that the initial conditions have been input correctly for a firing cycle.

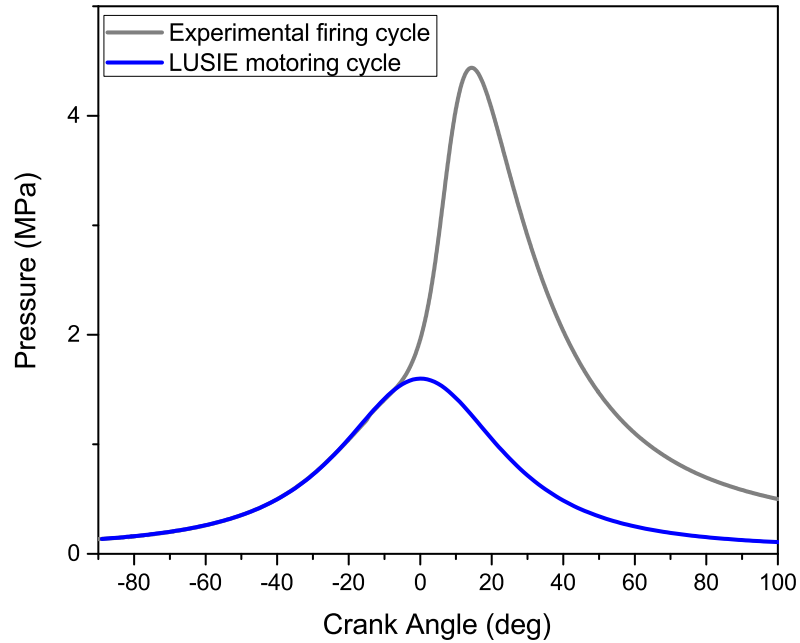


Figure 3.10: LUSIE simulated motoring pressure trace compared to experimental firing cycle.

### 3.4.2 Firing cycle validation

The firing cycle was validated against experimental data that had been split into fast, middle and slow combustion cycles, while the data in-between these regions was removed. This approach is commonly used when dealing with cyclic variability (Conway [2013], Burluka et al. [2012], Abdi Aghdam et al. [2007]). Fast, middle and slow cycle are determined by the peak pressure values, with the fast combustion cycles defined as  $P_{max} \geq \bar{P}_{max} + \sigma$ , where  $\bar{P}_{max}$  is the mean peak pressure value and  $\sigma$  is the standard deviation. The middle cycles are defined as  $\bar{P}_{max} - 0.25\sigma \leq P_{max} \leq \bar{P}_{max} + 0.25\sigma$ . Finally, slow cycles are defined as  $P_{max} \leq \bar{P}_{max} - \sigma$ . The pressure trace validation for the firing cycle is shown in Figure 3.11, where the LUSIE simulation corresponds to a middle combustion cycle. The tunable parameters,  $C_{ut}$  and  $C_{\tau b}$  (from Eqs. (3.15) and (3.5) ) were set to 0.35 and 16.5 respectively.

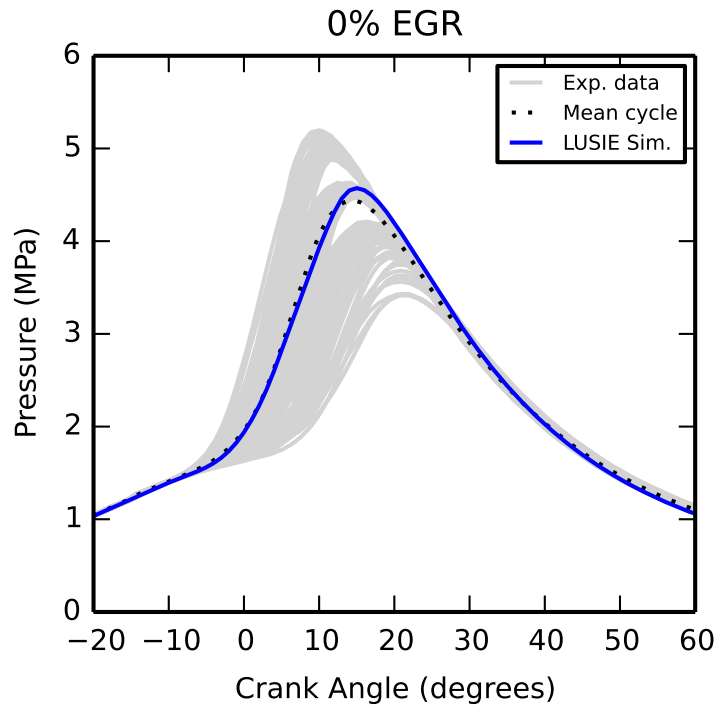


Figure 3.11: LUSIE simulated crank-resolved pressure trace with tuned constants and experimental data at 1500 rpm and GMEP of 0.79 MPa.

### 3.5 Description of Engine

The SCRE used throughout the study was a 1-cylinder version of the latest Jaguar Land Rover gasoline Ingenium engine (Fig. 3.12). The engine was installed at Imperial College London. A geometrical specification of the SCRE is shown in Table 3.3.

Table 3.3: Jaguar Land Rover SCRE specification

| Parameter  | Value      |
|--|------------|
| Displaced volume [cc]  | 499        |
| Compression ratio  | 10.9       |
| Number of cylinders  | 1          |
| Number of valves   | 4          |
| Fuel injection   | Central DI |
| Intake maximum opening point [ $^{\circ}$ CA aTDC <sub>gx</sub> ]  | 161        |
| Exhaust maximum opening point [ $^{\circ}$ CA bTDC <sub>gx</sub> ] | 121        |
| Intake phaser range [ $^{\circ}$ CA]                               | 50         |
| Exhaust phaser range [ $^{\circ}$ CA]                              | 50         |



Figure 3.12: Jaguar Land Rover test engine.

The crankcase and bottom end of this engine took the form of a Ricardo Hydra with the valvetrain consisting of a Continuously Variable Valve Lift (CVVL) electro-hydraulic system coupled with dual independent cam phasing on both intake and exhaust camshafts. The CVVL unit allowed for independent control of both intake valves therefore allowing for very different valve lift profiles including the ability to close one valve independent of the other. The engine load was controlled by a Bosch twin-track electronic throttle. However, for conditions utilising heavy dilution, an Eaton V250 supercharger driven by an electric motor was used to provide the additional air mass flow required to achieve the desired load (Roberts et al. [2018]).

The equipment and errors associated with engine data acquisition were outlined in Smith et al. [2018] and are quoted here “High speed, crank angle resolved data was recorded using AVL Indicom v2.6 as part of an AVL Indiset Advanced Gigabit unit utilising a 14-bit analogue to digital convertor (maximum error of  $\pm 0.95$  KPa,  $\pm 0.061$  KPa and  $\pm 0.122$  KPa for the in-cylinder, intake and exhaust pressure channels). A water-cooled Kistler 6041B piezo-electric sensor (accurate to  $<1\%$  of full scale), mounted flush with the combustion chamber surface, in combination with a Kistler 5064 charge amplifier were used to measure in-cylinder pressure. This ‘dynamic’ pressure was referenced to the intake manifold pressure (measured using a Kistler 4007 type sensor in conjunction with a Kistler 4665 signal conditioner) measured at the crank angle equidistant between the crank angles of maximum valve

lift and intake valve closure.”

The exhaust gas was recirculated back into the cylinder via a low pressure loop, resulting in the EGR being introduced upstream of a split in the intake system that was required to switch between the boosted and naturally aspirated modes. The hot EGR was cooled using a Ford DW12 water-cooled EGR cooler with the rate being controlled via a Ford DW12 EGR valve. The rate of EGR was calculated as the ratio of carbon dioxide content within the intake manifold to the carbon dioxide in the exhaust stream. The CO<sub>2</sub> levels for the EGR calculation were measured using a Horiba MEXA One emissions analyser. The emissions of other species, such as NO<sub>x</sub> and CO, were also measured using a Horiba MEXA One analyser.

# Chapter 4

## Exhaust Gas Recirculation in SI engines

---

### 4.1 Chapter Overview

The work presented in this chapter is focussed on determining a correction factor to the laminar burning velocity that models the effect of EGR from engine pressure data. Turbulent mass burning velocities,  $u_{tr}$ , were determined from pressure trace data using the LUSIEDA simulation code. A relation between the turbulent burning velocity and laminar burning velocity was required to calculate the EGR correction factor. A discussion on a suitable choice for the relation is presented in this chapter. Laminar burning velocities at various levels of EGR were utilised in calculating the EGR correction factor. Models from the literature provided a point of comparison for the correlation found in this study. Forward modelling using the LUSIE simulation code then compared the correlation found using engine data in this study to those found in the literature for engine pressure trace predictions and mass fraction burned profiles, at various speed and load points. The fuel used for this study was a EURO VI specification E10 gasoline (10% ethanol by volume). The full fuel specification can be found in Appendix A.

### 4.2 Pre-existing correlations

Cooled EGR leads to a decrease in laminar burning velocity, which is well documented in the literature. Therefore, in computer simulations of SI combustion

engines, the effect of EGR is typically modelled through a correction factor that reduces laminar burning velocity depending on the applied level of EGR. The correction factor is described by a ratio of laminar burning velocities:

$$\text{EGR correction factor} = \frac{u_l(f)}{u_l(f=0)} \quad (4.1)$$

where  $f$  is the mass fraction of EGR. A variety of different models have been suggested, but none of them are based on engine-like conditions. The study by Middleton et al. [2012] simulated the effect of EGR on the laminar burning velocity of isooctane air mixtures at high pressures (0.1 - 25 MPa) and high temperatures (400-1000K) typically associated with engine combustion, however the study was not validated against any experimental data. Furthermore, although the Metghalchi and Keck [1982] and Rhodes and Keck [1985] models were mentioned in the study no direct comparison of the EGR correction factors were made to assess their accuracy under the specified conditions.

The correction factor proposed by Metghalchi and Keck [1982] was found experimentally, using a diluent composition of 15% carbon dioxide and 85% nitrogen by volume to simulate combustion products. The experiments were carried out using a constant volume combustion chamber at an initial pressure of 0.1 MPa for a stoichiometric mixture of isooctane and air at an unburned gas temperature range of 340-440K.

Their model was later modified by Rhodes and Keck [1985] for a blended fuel similar to gasoline, known as indolene. The correction factor was determined for equivalence ratios of 0.7-1.2 and for initial pressures of 0.1 and 0.2 MPa. Due to the change in mixture, the composition of the combustion products acting as a diluent had to be modified with the products containing 20% carbon dioxide and 80% nitrogen by volume.

A correlation purely based on numerical simulations was determined by Fu et al. [2014] using the CHEMKIN-PRO software and the Frassoldati et al. [2012] model, which contains 7966 reactions and 249 species. The diluent composition is user defined and includes carbon dioxide, nitrogen and water. The laminar burning velocity simulations were carried out at pressures and temperatures of up to 0.5 MPa and 500K respectively for a stoichiometric mixture. However, the running conditions at which the EGR correction factor was determined are unclear.

The most recently suggested correction factor is based on a combination of simulations and experiments. Bhattacharya et al. [2015] used a commercial gasoline

Table 4.1: Summary of EGR correction factor correlations.

| Model                          | Method                        | Pressure (MPa) | Temperature (K) | $\phi$  |
|--------------------------------|-------------------------------|----------------|-----------------|---------|
| Metghalchi & Keck              | Combustion bomb               | 0.1            | 320-440         | 1.0     |
| Rhodes & Keck                  | Combustion bomb               | 0.1-0.2        | 350-550         | 0.7-1.2 |
| J.Fu <i>et al.</i> (isooctane) | Numerical simulation          | 0.5            | 500             | 1.0     |
| Bhattacharya <i>et al.</i>     | Burner & Numerical simulation | 0.1            | 423             | 0.7-1.3 |
| Present study                  | Engine                        | 3.0            | 768             | 1.0     |

(Shell V-Power as available in Germany) that, given the publication date of the paper, should be compliant with EURO VI regulations. For the experimental data Bhattacharya *et al.* used a heat flux burner to determine the stretch free laminar burning velocities with the diluent comprising of carbon dioxide and nitrogen. Simulations were performed using the CHEMKIN-PRO package with a chemical mechanism constituting 877 reactions and 171 species (Luong *et al.* [2013]). This mechanism had been derived from a more complex mechanism containing 3796 reactions and 874 species (Curran *et al.* [1998, 2002]). The chemical model was validated against the burner experimental data and a correlation for the EGR correction factor was proposed. Both experimental and numerical data was taken at a pressure of 0.1 MPa and unburned gas temperature of 432 K.

Mannaa *et al.* [2017] investigated the effect of exhaust gas recirculation on the laminar burning velocity of a fuel for a advanced combustion engine (FACE-C) gasoline. No correction factor was specified, although a quasi-linear decrease with increasing EGR was found.

No work exists that compares these models in terms of their accuracy under engine conditions. Therefore, it is not clear which models are useful to study EGR or whether any of them are predictive at all. A summary of the conditions at which published correlations were determined is presented in Table 4.1.

### 4.3 Engine data correlation

The processes of determining an EGR correction factor starts with collecting the in-cylinder pressure data at varying levels of EGR. To enable a comparison between the combustion parameters, the engine load was kept constant by increasing the engine boosting and advancing the spark timing as the levels of EGR increased. The running conditions for each case are summarised in Table 4.2. The correlation was derived at an engine speed of 1500 rpm at full load, with a GMEP of 0.79 MPa.

The percentage of EGR for each case in Table 4.2 includes the external EGR only

Table 4.2: Experimental running conditions for increasing levels of EGR to maintain a constant engine load of 0.79 MPa GMEP at 1500rpm.

| Case | $P_{IVC}$ (MPa) | Spark timing (deg bTDC) | EGR % (by mass) |
|------|-----------------|-------------------------|-----------------|
| 0    | 0.135           | 15                      | 0               |
| 1    | 0.14            | 17.5                    | 5               |
| 2    | 0.145           | 20                      | 10              |
| 3    | 0.152           | 22                      | 15              |
| 4    | 0.158           | 26.5                    | 20              |
| 5    | 0.163           | 29                      | 25              |

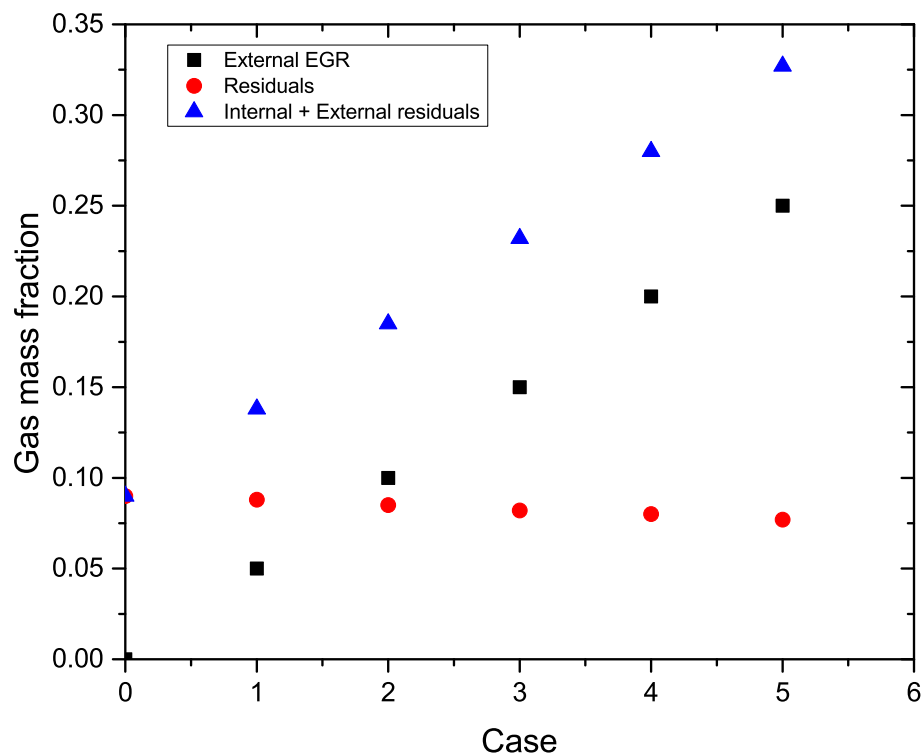


Figure 4.1: External EGR, post exhaust residual gas and total in-cylinder residuals for each case described in Table 4.2.

and does not account for the in-cylinder residuals that are trapped after each firing cycle. The mass fraction of residuals contributes to the in-cylinder temperature at IVC and alters the turbulent mass burning velocity as the density of the unburned gas is altered (see Eq. (3.2)) The residuals were calculated using the model developed by Cho et al. [2001]. The external EGR, residuals and total residuals are presented in Figure 4.1. The level of residuals were found to be approximately constant at around 8% by mass.

The experimental data was then analysed using the reverse thermodynamic code, LUSIEDA (see section 3.3). Turbulent burning velocities were calculated from the

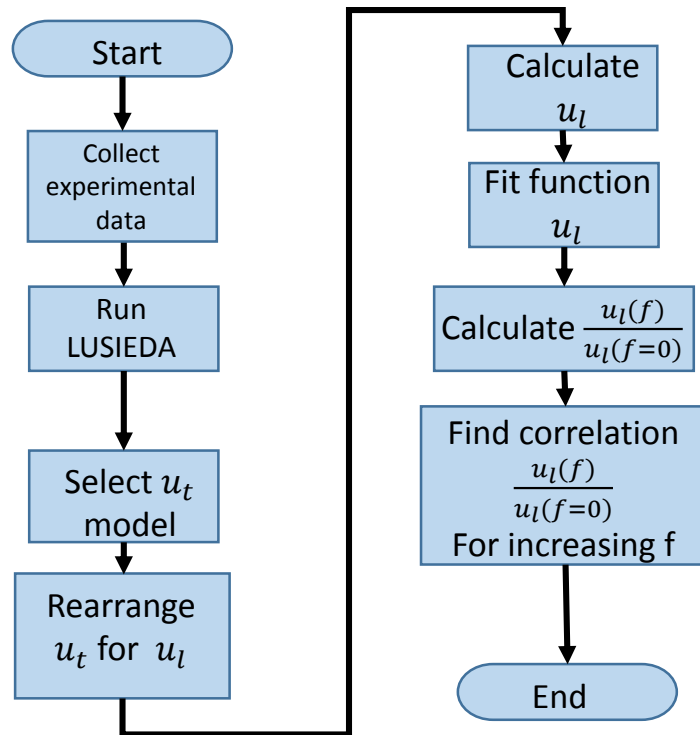


Figure 4.2: Flowchart describing process of obtaining EGR correction factor from engine pressure trace data.

experimental pressure trace data before a relation between turbulent burning velocity and laminar burning velocity was used to calculate the laminar burning velocity. Once the laminar burning velocity was known the EGR correction factor could be determined. A discussion on the choice of model to back-calculate the laminar burning velocity can be found in section 4.3.1. The process of obtaining the EGR correction factor from the experimental engine data is depicted as a flowchart in Figure 4.2.

In the back-calculation of the correction factor, for the sake of simplicity, the mean  $u_{tr}$  value over all experimental pressure traces was used, instead of running 300 instances of the backward model and averaging those. The mean cycle is calculated by averaging the pressure at every  $0.1 \text{ CA}^\circ$ . To ensure that the correction factor derived from data is not sensitive to the number of acquired pressure traces the correction factor using the first 100 and 200 cycles acquired were compared to the full 300 cycle data set. The correlations determined for 100, 200 and 300 cycles are presented in Figure 4.3. The 200 and 300 cycle correction factors are extremely

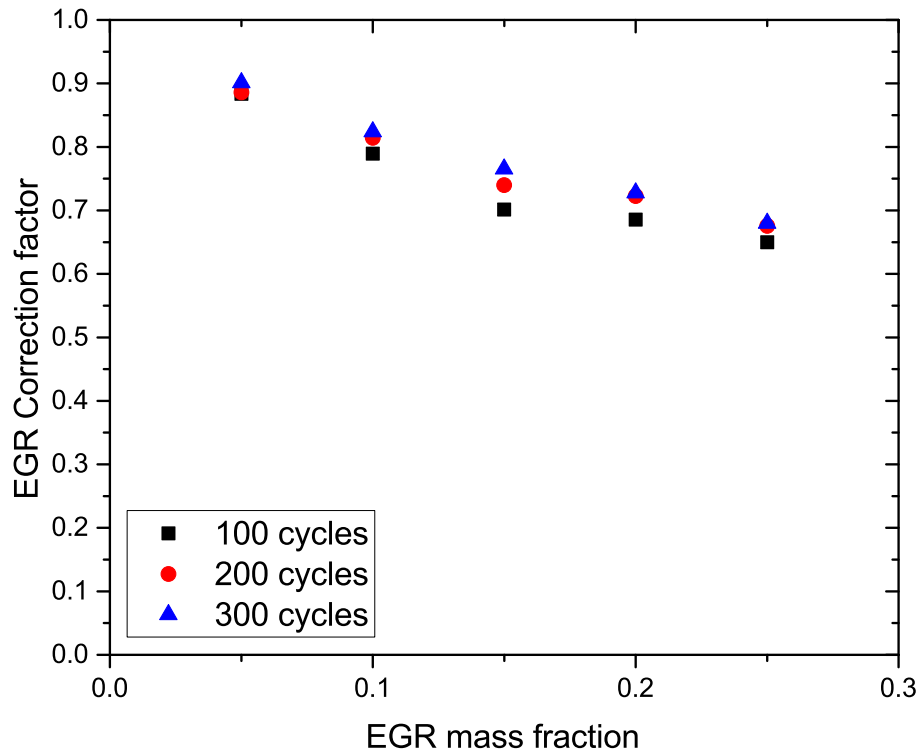


Figure 4.3: Correction factor resulting when considering data from different numbers of cycles. The average difference between the results is 1.5%.

close and have an average difference of 1.5%. As the number of cycles increases the difference between the correction factors decrease, showing that the 300 cycle is statistically stable.

### 4.3.1 Turbulent-laminar burning velocity relation

Once the turbulent mass burning velocity,  $u_{tr}$ , is calculated from engine pressure data, the laminar burning velocity can be derived. In predictive modelling, a laminar burning velocity model is usually an input to predict the turbulent burning velocity of the flame. In this case a model of the turbulent burning velocity is utilised to back-calculate the laminar burning velocity from the pressure trace data. This method relies on an accurate description of the turbulent burning velocity and its dependence upon the laminar burning velocity. The turbulent burning velocity model selected is the Zimont-Lipatnikov model. This model was selected as it provides reasonable predictive simulations. A full description of the model can be found in section 3.2.5. Rearranging the Zimont-Lipatnikov for the laminar burning velocity,  $u_l$ , gives:

$$u_l = 0.5 \cdot (Z^2 - (Z^4 + 4Z^2 \cdot u_{tr})^{0.5} + 2u_{tr}) \quad (4.2)$$

where  $Z$  is:

$$Z = C_{ut} u'_k \left( \frac{L}{u' \kappa} \right)^{0.25} \quad (4.3)$$

and  $u'_k$  is the turbulent RMS velocity multiplied by the Zimont-Lipatnikov flame development factor, stated in Eq. (3.18).

In predictive simulations using the forward model, the constant  $C_{ut}$  is fixed by tuning the model to measurements. The value of  $C_{ut}$  is tuned to model the turbulent mass burning velocity,  $u_{tr}$ , for the two-zone model and the turbulent entrainment velocity for the three-zone model. However, this tuning is not possible for the backward model. In theory, because the EGR correction factor divides two laminar burning velocity values, the model constant will cancel out. Although this should be the case an attempt to constrain the value has been made by utilising a similar turbulent burning velocity model from the literature.

It is discussed in section 3.2.5 that recent studies by Bradley et al. [2011] and Bradley et al. [2013] have determined a turbulent burning velocity model, referred to here as the U/K model, that is similar to the Zimont-Lipatnikov model. One advantage of the U/K correlation is that there is no model constant that requires tuning. However, the constant  $C_{ut}$  can be fixed in the Zimont-Lipatnikov model so that it closely aligns with the U/K correlation for a given Markstein number. The U/K correlation cannot be used directly as insufficient information in the literature exists to provide stretch rate Markstein numbers at the pressures and temperatures within an engine, as well as for a changing mixture composition (increasing EGR).

The Damköhler number is inversely proportional to the Karlovitz stretch factor, with an extra factor to account for the difference in turbulence length scales used:

$$\text{Da} = K^{-1} \cdot \frac{L}{\lambda} \quad (4.4)$$

where  $\lambda$  is the Taylor microscale. If we ignore the added laminar burning velocity term that accounts for  $u' \rightarrow 0$ , the Zimont-Lipatnikov model becomes:

$$U = C_{ut} \left( \frac{L}{\lambda} \right)^{1/4} K^{-1/4}. \quad (4.5)$$

To obtain  $\beta = -1/4$  in the U/K correlation (Eq. (3.8)), we need to set  $\text{Ma}_{sr} = 5.73$  in Equation (3.9b), which in turn means that  $\alpha = 0.558$  according to (3.9a). Note that there is no negative value of  $\text{Ma}_{sr}$  for which Equation (3.10b) gives  $\beta = -1/4$ .

The ratio between the integral length scale and Taylor microscale to the power of -1/4 is approximately constant with values varying between 0.61 and 0.59. The mean value is used, setting

$$\left(\frac{L}{\lambda}\right)^{-1/4} = 0.6. \quad (4.6)$$

Equating the U/K correlation (3.8) with  $\beta = -1/4$  and Eq. (4.5) gives, after cancelling  $K^{-1/4}$ ,

$$\alpha = C_{ut} \left(\frac{L}{\lambda}\right)^{1/4}. \quad (4.7)$$

From that, a value of  $C_{ut}$  that aligns the Zimont-Lipatnikov model with the U/K correlation can be determined:

$$C_{ut} = \alpha \left(\frac{L}{\lambda}\right)^{-1/4} = 0.558 \left(\frac{L}{\lambda}\right)^{-1/4} = 0.33. \quad (4.8)$$

Therefore a value of  $C_{ut} = 0.33$  is used for the backward model.

Note that the stretch rate Markstein number for isooctane was found to be around 6 at 0.1 MPa and 358K (Bradley et al. [1998]) with an error of  $\pm 1$ . While the measurements taken in this study were at a higher pressure and higher temperature, it has been shown that increases in pressure will lead to a decrease in  $\text{Ma}_{sr}$  (Bradley et al. [1998, 2009]) whereas an increase in temperature leads to an increase in  $\text{Ma}_{sr}$  (Bradley et al. [1998].) Therefore, the value of  $\text{Ma}_{sr} = 5.73$  used for gasoline in this study seems reasonable, but the lack of data in the literature prevents a more quantitative assessment. Experiments aiming to determine Markstein number at high temperatures and pressure would be an important area for future research.

It is worth stressing that the only free parameter in the backwards model is  $C_{ut}$  and that the resulting correction factor is not particularly sensitive to it: changing  $C_{ut}$  by  $\pm 10\%$  was found to have a negligible effect on the back-calculated EGR correction factor, with a maximum change of 1.5% over all EGR values. The EGR correction factors for the sensitivity study are presented in Figure 4.4.

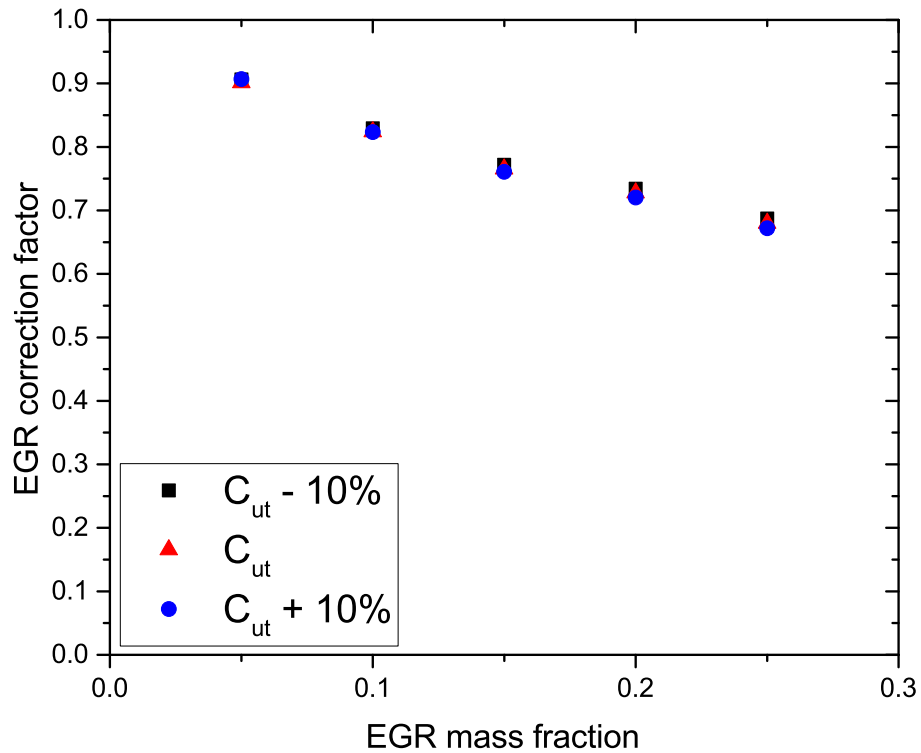


Figure 4.4: Correction factor resulting from sensitivity analysis of  $C_{ut}$  ( $C_{ut}=0.33$ ). The maximum difference over all points is 1.5%.

### 4.3.2 Final correlation

Laminar burning velocities were calculated, using Eq. (4.2), for a range of EGR values from the experimentally derived turbulent burning velocity. To avoid spark and flame deceleration effects, the burning velocity measurements were taken when the burned gas radius was 10-30mm. The back-calculated laminar burning velocity plotted against in-cylinder pressure is shown in Fig. 4.5. A logistic function was used to fit the data points and then to calculate the EGR correction factor for the varying levels of EGR shown in Fig. 4.6.

The calculated EGR correction changes as the flame develops over time. The flame has been found to develop in three stages: first initial acceleration, then propagation at an approximately constant speed, finally deceleration due to wall effects (Liu et al. [2013]). Presented in Figure 4.7 is the turbulent mass burning velocity plotted against burned gas radius for increasing external EGR values. The correction factor should account for the steady flame propagation phase as initial flame development and flame interaction with the cylinder walls is already accounted for in the forward modelling. The steady state phase in Figure 4.7 increases as the level of EGR increases, but is not very pronounced for the 0% case. The in-cylinder

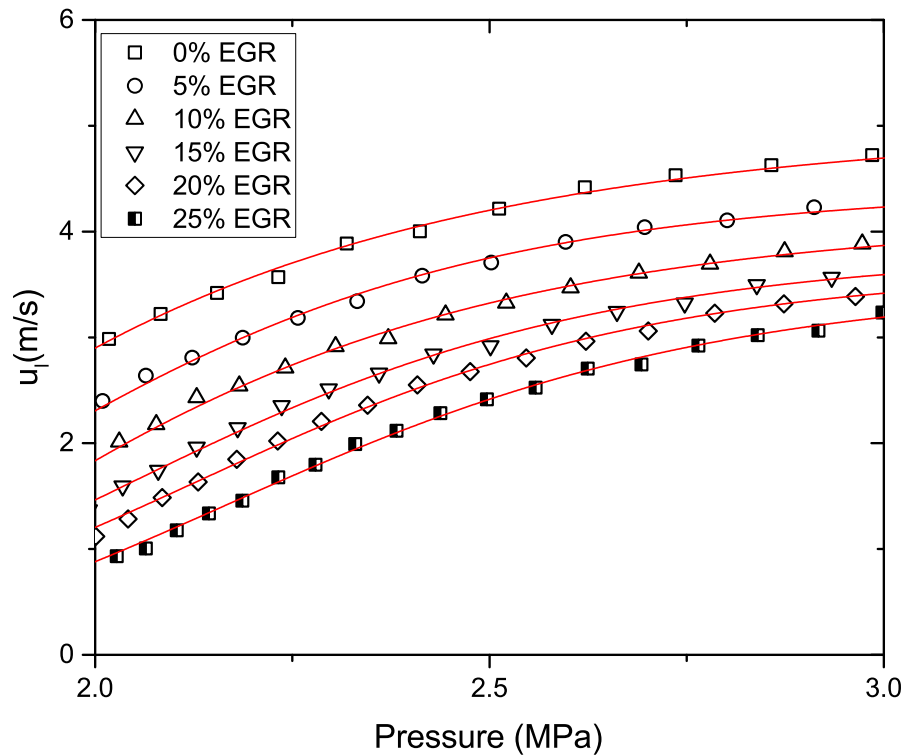


Figure 4.5: Back calculated laminar burning velocity plotted against the change in in-cylinder pressure (symbols) and curve fitting of  $u_l$  (lines).

pressure for when the turbulent mass burning velocity is propagating steadily for the 0% case is approximately 3.0 MPa. The values chosen correspond to those at an in-cylinder pressure of 3.0 MPa which lies well within the steady-state propagation phase for all EGR cases under these conditions. The pressure had to be equal for all EGR values due to the influence of pressure on the laminar burning velocity.

Obtained correction factors are plotted against EGR fraction in Fig. 4.8, together with models from the literature. All models show an approximately linear decrease of the correction factor with EGR. The models by Bhattacharaya *et al.* and Metghalchi & Keck are very closely aligned. The model described by the present study is similar to the Bhattacharya *et al.* and Metghalchi & Keck at lower levels of EGR however as the level of EGR increases the present study reduces the laminar burning velocity significantly less than all models from the literature. The model derived in the present study finds that the EGR correction factor is larger at high levels of EGR compared to the literature. This could be attributed to the composition of the EGR containing species like hydrogen which burn much faster than those included in the simulated EGR within the literature. This is supported by a study by Manna et al. [2017] who found that synthetic EGR reduced the laminar burning velocity more than real exhaust gas.

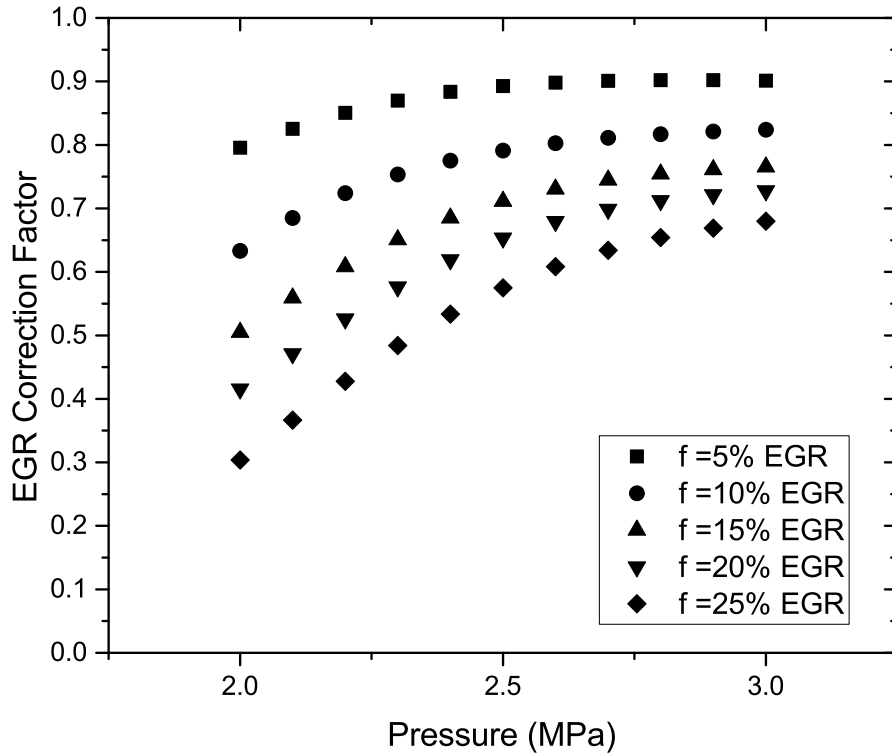


Figure 4.6: EGR correction factor plotted against the change in in-cylinder pressure for increasing levels of EGR.

A quasi-linear fit of the data from the present study found that the EGR correction factor changes with the mole fraction of EGR as:

$$\frac{u_i(f_{mole})}{u_i(f_{mole} = 0)} = 1 - 0.835 f_{mole}^{0.687} \quad (4.9)$$

where  $f_{mole}$  is the mole fraction of EGR diluent. The mole fraction of EGR was calculated experimentally as the ratio of  $\text{CO}_2$  in the intake manifold to the ratio of  $\text{CO}_2$  in the exhaust stream. The correlation by Bhattacharya *et al.* is of a similar form and is given by (for  $\phi = 1.0$ ):

$$\frac{u_i(f)}{u_i(f = 0)} = 1 - 1.68 f^{0.84}. \quad (4.10)$$

where  $f$  is the mass fraction of EGR diluent. The model by Rhodes & Keck is given by:

$$\frac{u_i(f_{mole})}{u_i(f_{mole} = 0)} = 1 - 2.06 f_{mole}^{0.773} \quad (4.11)$$

The Rhodes and Keck [1985] model has the same functional form as the Bhat-

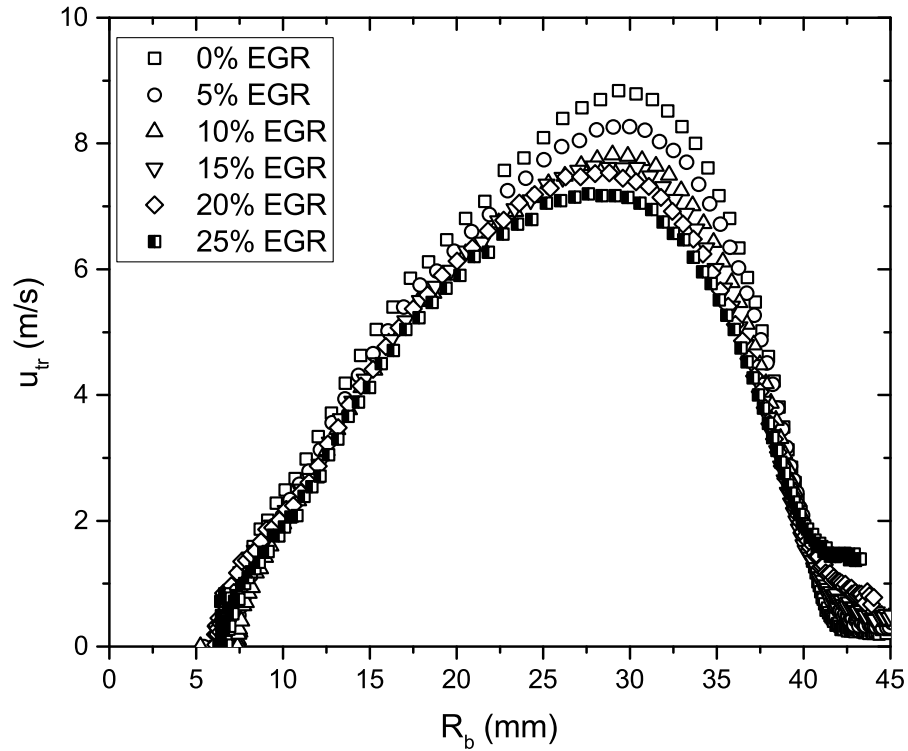


Figure 4.7: Turbulent mass burning velocity plotted against burned gas radius for increasing levels of EGR.

tacharya et al. [2015] model but due to different parameters leads to significant differences in the obtained correction factors at higher levels of EGR.

The oldest model by Metghalchi & Keck suggests a linear correlation:

$$\frac{u_l(f)}{u_l(f=0)} = 1 - 2.1 f. \quad (4.12)$$

The model suggested by Fu *et al.* is slightly different than the others as it models the components of the diluent individually

$$\frac{u_l(f_{mole})}{u_l(f_{mole}=0)} = 1 - \sum_{i=1}^n X_i \mu_{1,i} f_{mole,i}^{(\mu_{2,i} + \mu_{3,i}(\phi - \phi_{m,i}) + \mu_{4,i}(\phi - \phi_{m,i})^2)} \quad (4.13)$$

where  $X_i$  is the mole fraction of a single component in total diluents,  $n$  is the total number of diluents,  $\mu_1 - \mu_4$  and  $\phi_m$  are correlation coefficients. For our case ( $\phi=1$ )

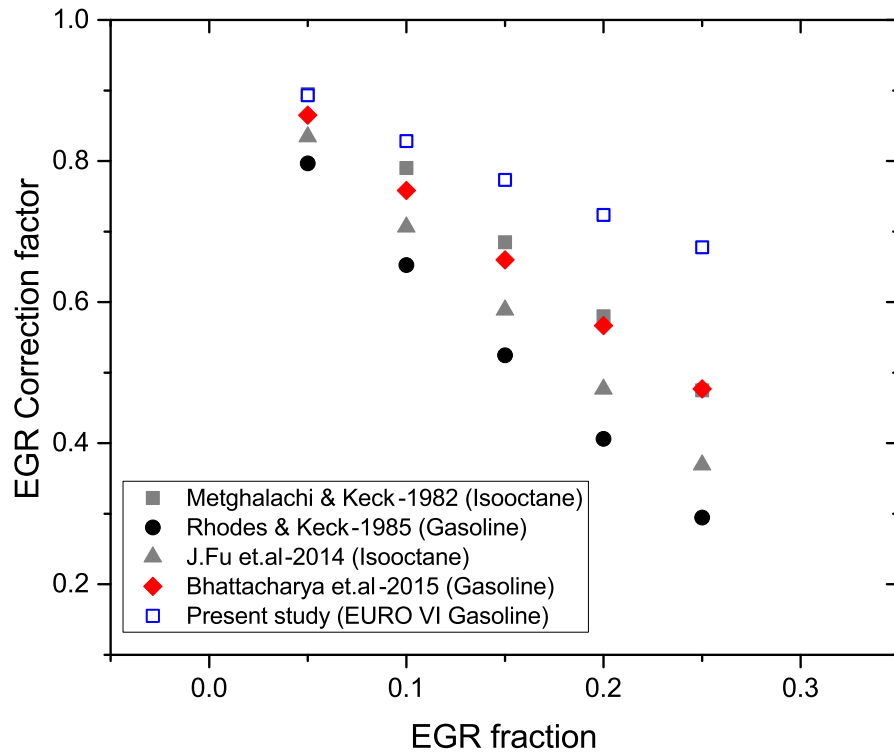


Figure 4.8: EGR correction factor plotted against mass fraction of residuals. The plot compares results from the present study to correction factors found within the literature.

the correlation is given by:

$$\frac{u_l(f)}{u_l(f=0)} = 1 - (0.25 f_{mole}^{0.63} + 0.3 f_{mole}^{0.8} + 1.5 f_{mole}^{0.9}) \quad (4.14)$$

where the mole fraction of each diluent was calculated using the isooctane balance equation



While this back-calculating approach comes with challenges regarding the proper choice of model parameters, by relying on engine data it captures the effects of the full composition of the exhaust gas.

## 4.4 Predictive modelling

The predictive modelling utilised the LUSIE code described in section 3.2 to predict the pressure traces and mass fraction burned profiles for the various EGR correction factor models, at a number of test points. The predictive modelling was carried out under three test points. Two test points at 1500 rpm with engine loads of 0.36 MPa GMEP and 0.79 MPa GMEP and one test point at 2000 rpm and an engine load of 0.98 MPa GMEP. The different test conditions were to validate the correlation derived by this study at different engine speed/load points than which it was derived. As the levels of external EGR increased the spark was advanced and intake manifold pressure increased to ensure engine load was kept constant and to maintain MBT spark timing.

The total number of experimental cycles logged for each case was 300. The experimental pressure trace data used for validating the EGR correction factors was divided into fast, middle and slow combustion cycles. The method utilised to group the different combustion cycles is described in section 3.4.2. The number of fast, middle and slow combustion cycles included in each plot can be found in the respective figure captions.

### 4.4.1 1500 rpm, 0.79 MPa GMEP

#### 4.4.1.1 Pressure traces

The pressure traces were simulated for increasing levels of EGR, ranging from 5% to 25% (by mass) in increments of 5%. Figs. 4.9-4.13 show the simulated pressure traces for the different correlations at varying levels of diluent. For the correlations derived using the mole fraction of diluent (Rhodes and Keck [1985], Fu et al. [2014]) the mass fraction user input was converted to mole fraction within the LUSIE code. To avoid clutter, results from the Metghalchi & Keck and Fu et al. model are not shown, but they are relatively close to those from the Bhattacharya *et al.* and Rhodes & Keck respectively. Fig. 4.14 shows the root mean square error between simulated and experimental pressure values plotted against level of EGR for all models.

At the lowest level of EGR simulated (5%) all of the correlations provide a reasonable fit to the experimental data. This is somewhat unsurprising as the difference between EGR correction factor values is smallest at lower values of EGR, as shown in Fig. 4.8.

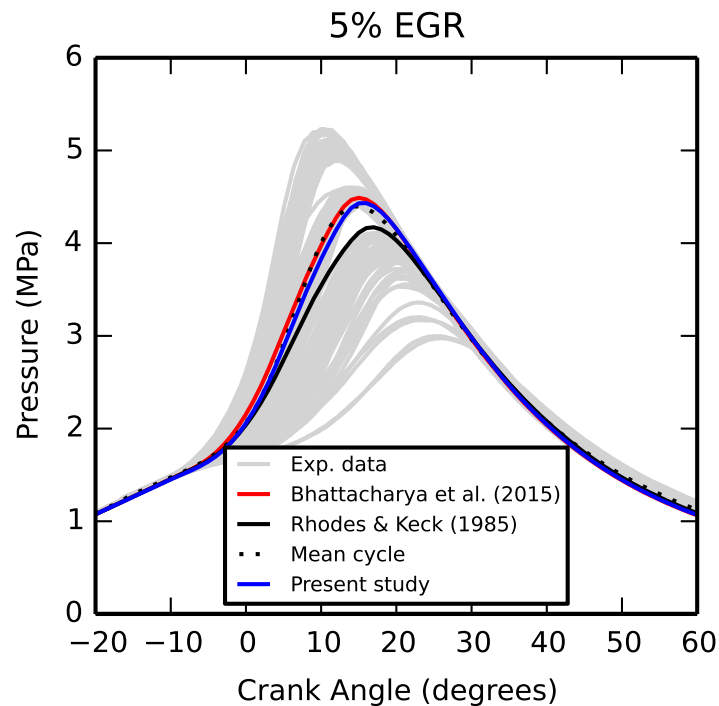


Figure 4.9: Predicted engine pressure traces comparing the correlation found in the present study to models found in the literature, at 5% EGR. Experimental data is comprised of 36 fast, 77 middle and 47 slow combustion cycles.

Substantial differences between models arise as the level of EGR increases to values between 15% and 25%. Both the models by Rhodes & Keck and Fu et al. simulate an increasingly poor match with experimental data, with RMS errors increasing roughly linearly with EGR mass fraction. The Bhattacharya *et al.* and Metghalchi & Keck model give reasonable simulations up to 15% EGR. While the simulations fall within the experimental bounds up to 15% the predicted cycles are not always closely aligned with the mean cycle and model faster combustion for the 5 and 10% cases but slower combustion from 15 to 25%. The new correlation from the present study improves on these two models for both the 20% and 25% EGR cases predicting pressure trace much closer to the mean than any of the models from the literature. The difference at higher levels of EGR is possibly attributed to the diluent composition itself, with the current study recirculating actual exhaust gas, which would include species such as:  $\text{CO}_2$ ,  $\text{N}_2$ ,  $\text{H}_2\text{O}$  and  $\text{NO}_x$ , as opposed to using a simulated EGR containing only  $\text{CO}_2$  and  $\text{N}_2$ .

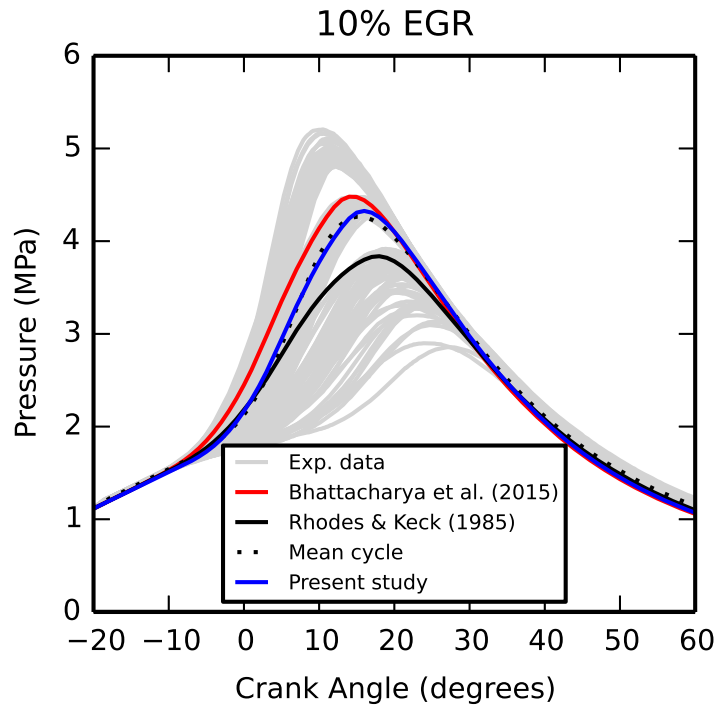


Figure 4.10: Predicted engine pressure traces comparing the correlation found in the present study to models found in the literature, at 10% EGR. Experimental data is comprised of 41 fast, 51 middle and 45 slow combustion cycles.

#### 4.4.1.2 Mass fraction burned

The mass fraction burned was utilised as a second metric to validate the EGR correction factors previously described. The heat released from the experimental engine data was calculated from the first law of thermodynamics. The net heat release is given by (Stone [2012]):

$$\frac{dQ_n}{d\theta} = \frac{\gamma}{\gamma - 1} P \frac{dV}{d\theta} + \frac{1}{\gamma - 1} V \frac{dP}{d\theta}. \quad (4.16)$$

The heat release is simply proportional to the mass fraction burned and is therefore comparable to the LUSIE output.

The predictive models were compared to all 300 experimental cycles as well as the mean mass fraction burned profile. Presented in Figs. 4.15-4.19 are the crank resolved mass fraction burned profiles at increasing levels of EGR.

Like the pressure trace profiles the RMS error between the simulated and mean cycles was calculated for each model, the results of which are shown in Figure 4.21. As the levels of EGR increases the Rhodes and Keck [1985] model becomes less

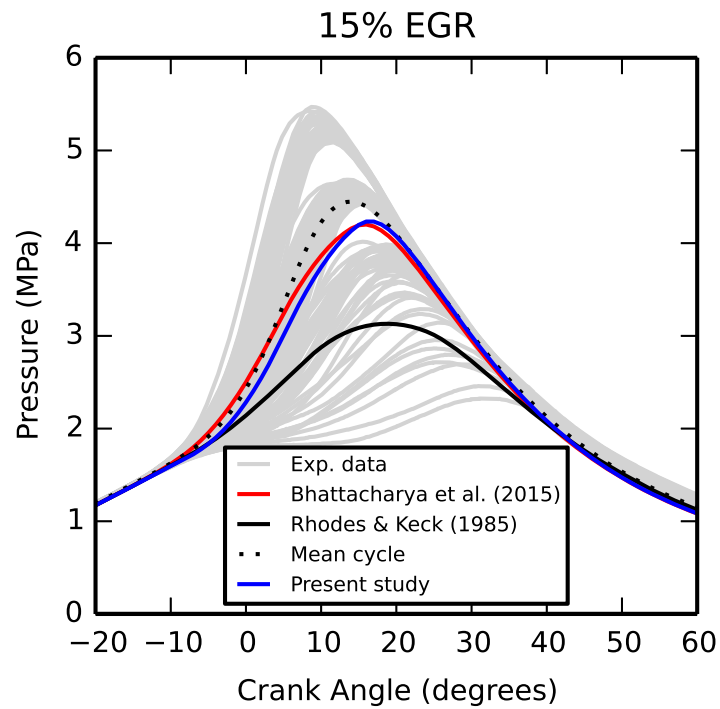


Figure 4.11: Predicted engine pressure traces comparing the correlation found in the present study to models found in the literature, at 15% EGR. Experimental data is comprised of 37 fast, 63 middle and 41 slow combustion cycles.

accurate in predicting the mass fraction burned. The reason for this is that at high levels of EGR the reduction in laminar burning velocity by the model is greater than observed, just like for the pressure trace simulations. Comparing the RMS errors for the pressure trace data and mass fraction burned, Figures 4.14 and 4.21 respectively, the greater the model reduces the laminar burning velocity with increasing EGR the less well it is able to predict combustion parameters. The RMS errors for both pressure trace and mass fraction burned follow the same trends.

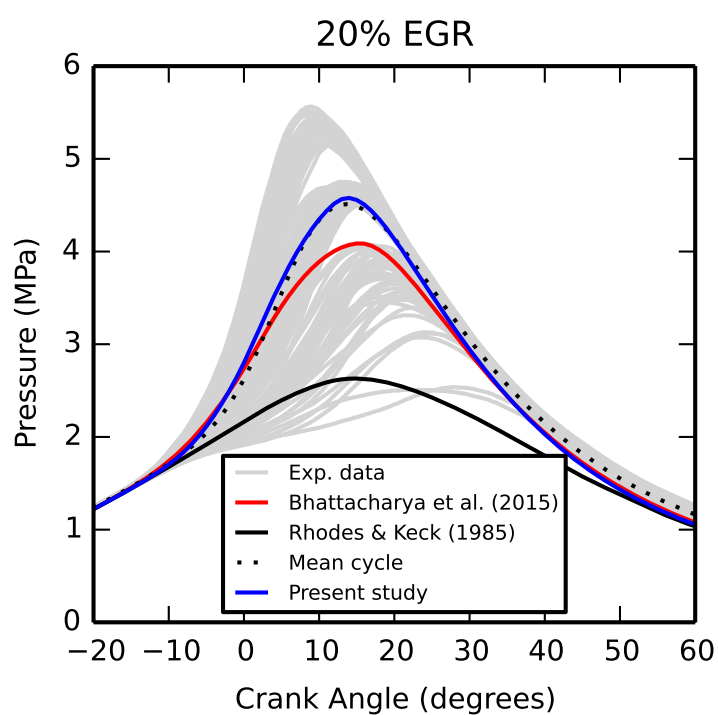


Figure 4.12: Predicted engine pressure traces comparing the correlation found in the present study to models found in the literature, at 20% EGR. Experimental data is comprised of 46 fast, 63 middle and 44 slow combustion cycles.

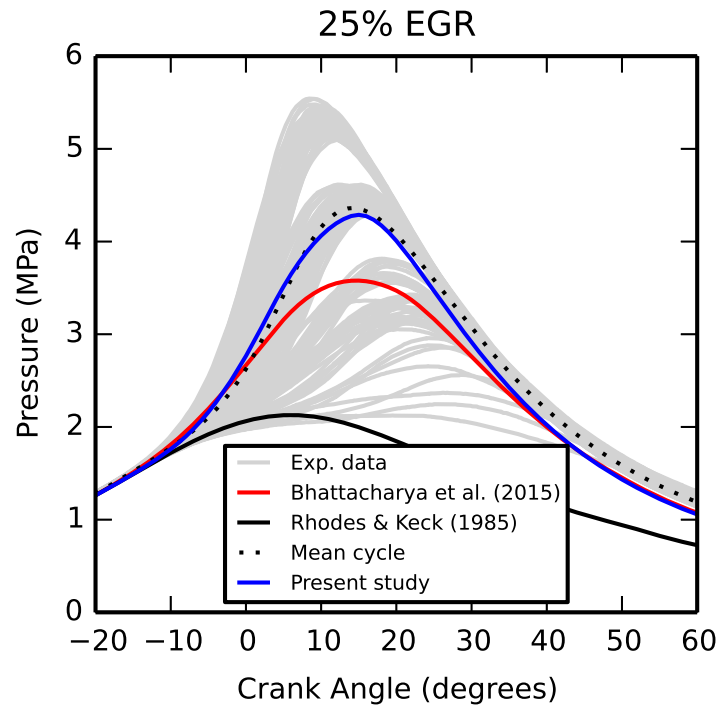


Figure 4.13: Predicted engine pressure traces comparing the correlation found in the present study to models found in the literature, at 25% EGR. Experimental data is comprised of 44 fast, 65 middle and 44 slow combustion cycles.

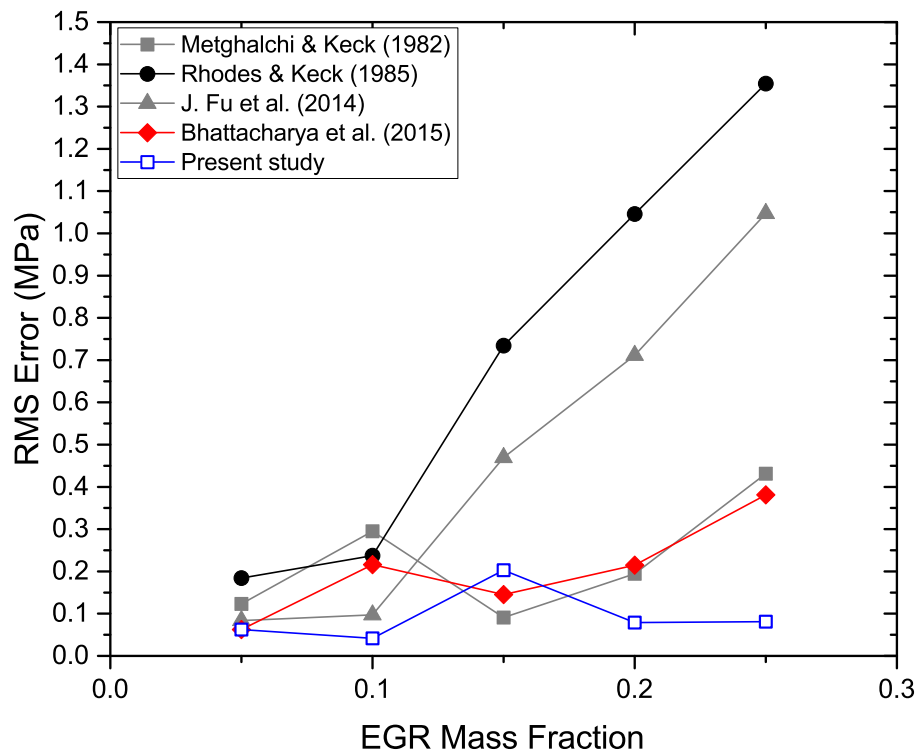


Figure 4.14: RMS error against measured pressure trace for varying levels of EGR for simulations at 1500 rpm and GMEP of 0.79 MPa.

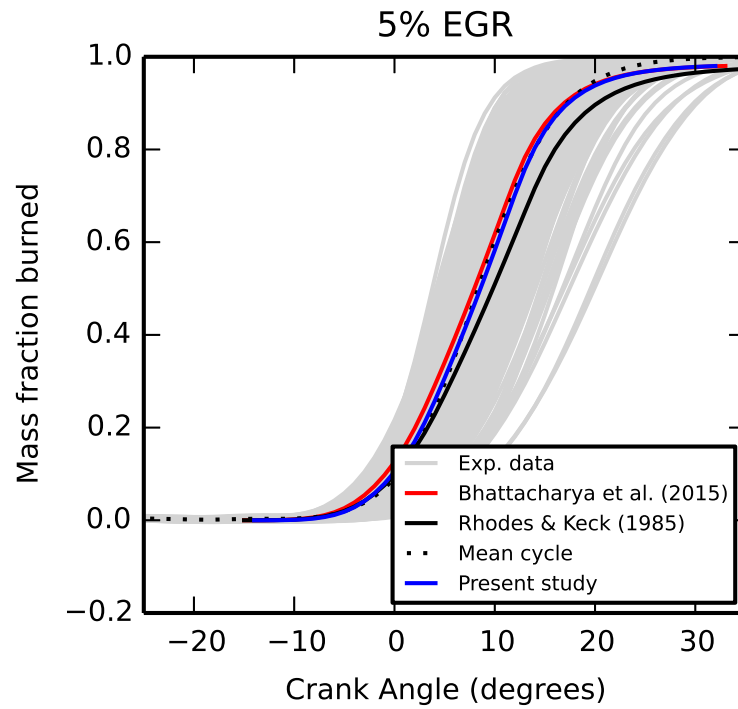


Figure 4.15: Predicted mass fraction burned comparing the correlation found in the present study to models found in the literature, at 5% EGR.

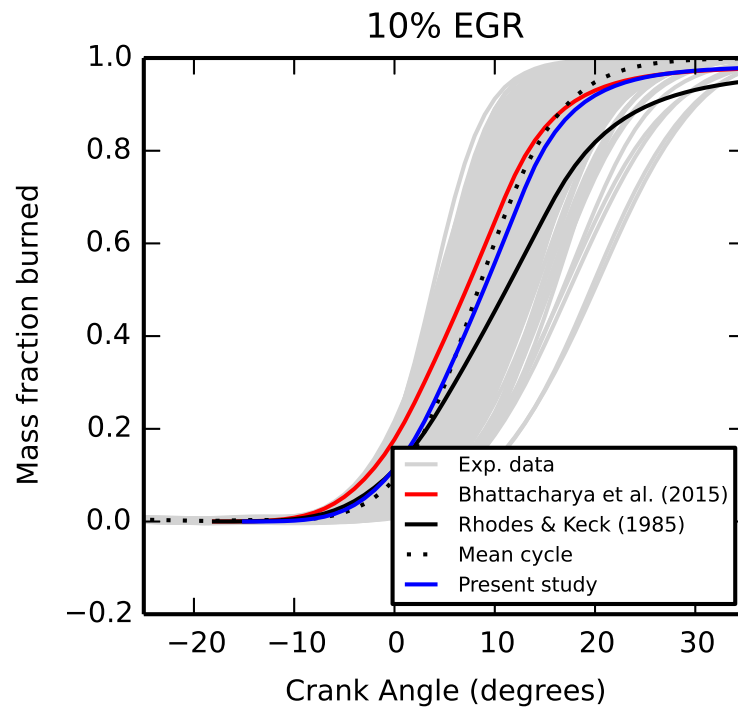


Figure 4.16: Predicted mass fraction burned comparing the correlation found in the present study and in the literature to experimental data, at 10% EGR.

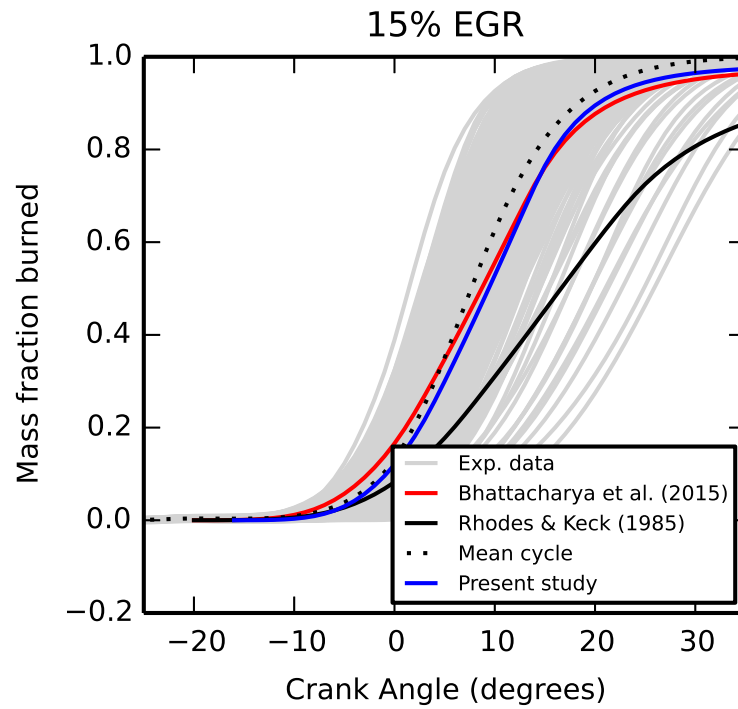


Figure 4.17: Predicted mass fraction burned comparing the correlation found in the present study to models found in the literature, at 15% EGR.

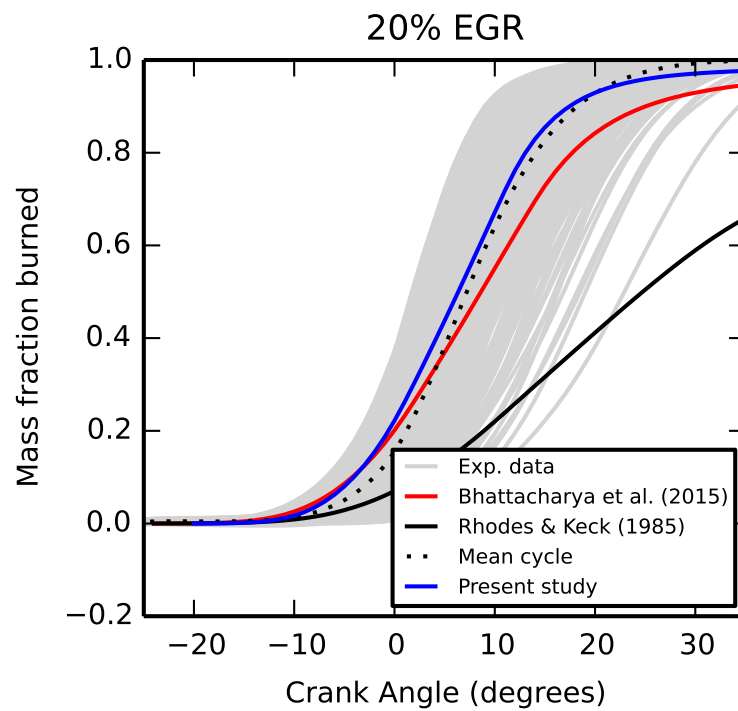


Figure 4.18: Predicted mass fraction burned comparing the correlation found in the present study to models found in the literature, at 20% EGR.

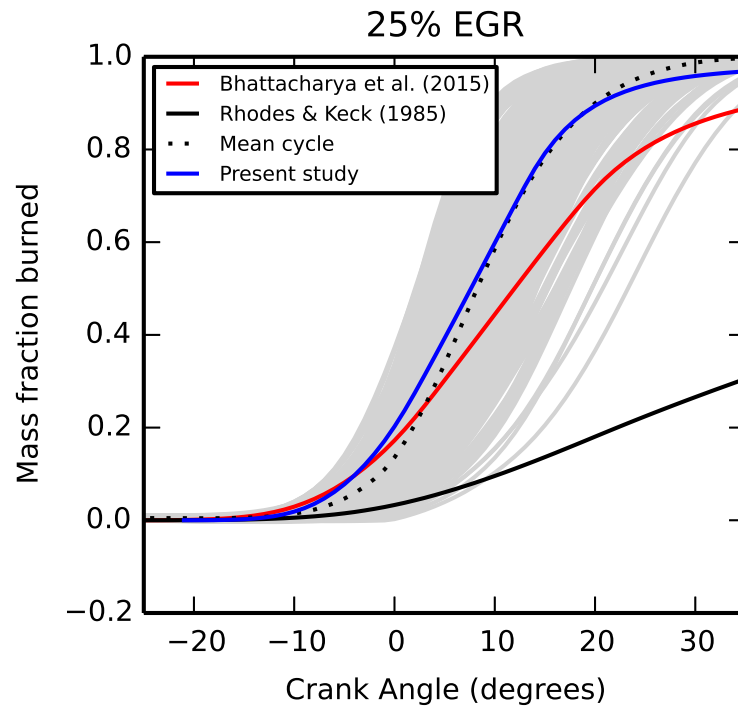


Figure 4.19: Predicted mass fraction comparing the correlation found in the present study to models found in the literature, at 25% EGR.

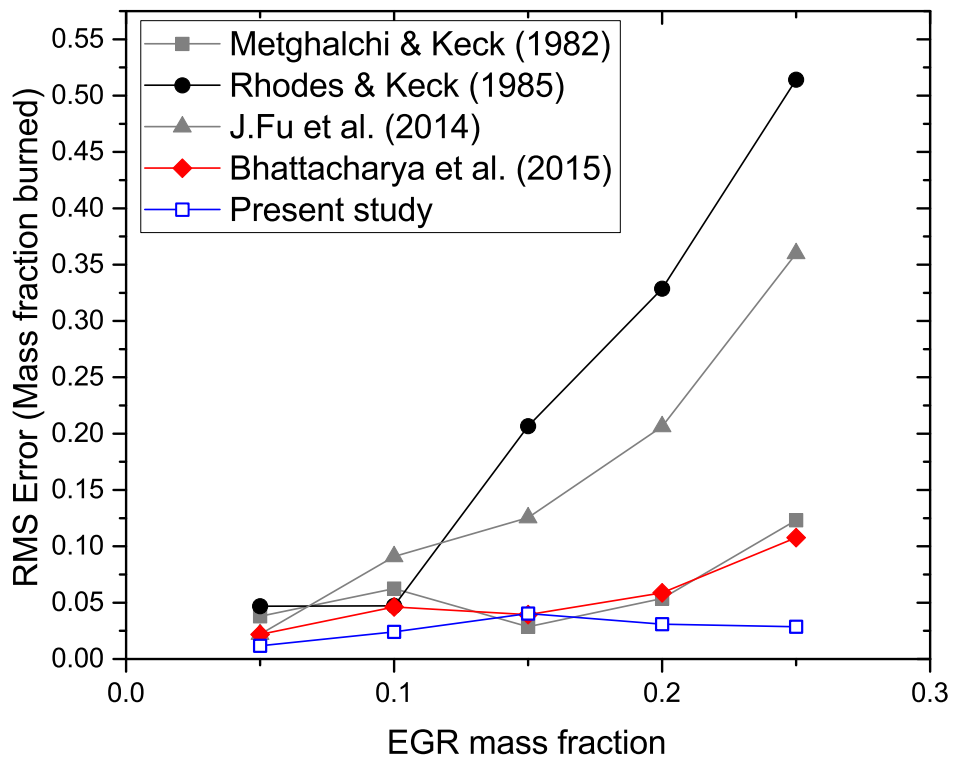


Figure 4.20: RMS error for predicted mass fraction burned for varying levels of EGR for simulations at 1500 rpm and GMEP of 0.79 MPa.

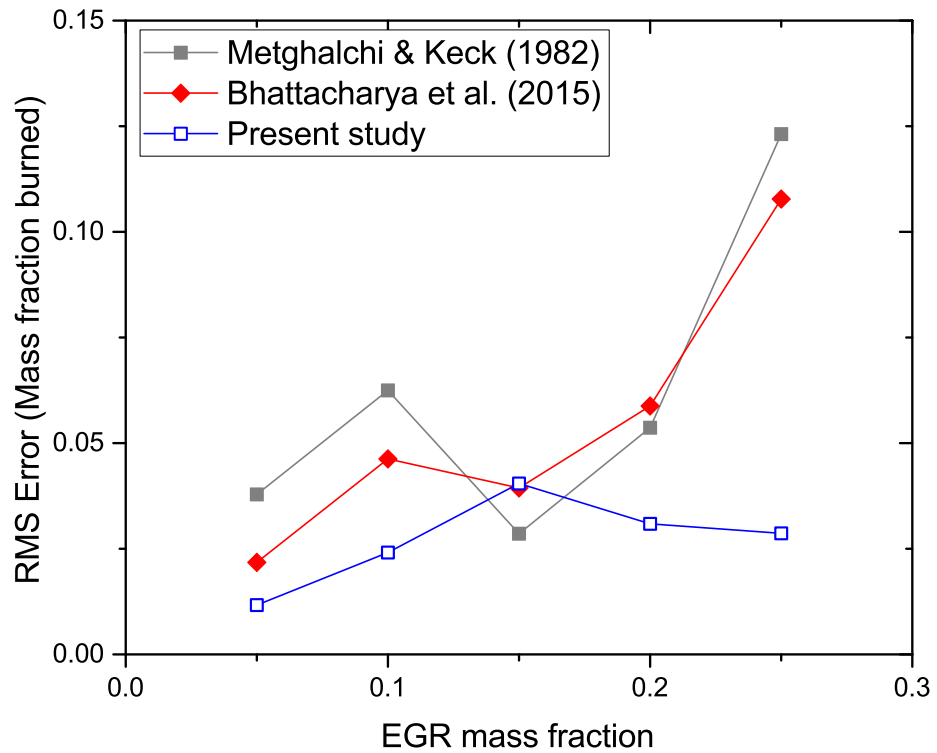


Figure 4.21: RMS error for predicted mass fraction burned for varying levels of EGR for simulations at 1500 rpm and GMEP of 0.79 MPa showing the three best performing models only.

#### 4.4.2 1500 rpm, 0.36 MPa GMEP

The pressure trace data was once again validated at 0% EGR for the selected load/speed. While the tuning of constants may not have been necessary to match experimental data, it was necessary to match with a middle cycle. It is important to model a middle cycle close to the mean cycle at 0% EGR. This helps ensure that the RMS error for the EGR simulations is truly representative. Once the 0% case had been tuned predictive simulations were ran for the same correlations in section 4.4.1. The tuning parameters for the characteristic burn-up time was set to  $C_{\tau_b} = 25$  while the turbulent burning velocity constant was set to  $C_{ut} = 0.35$ . The forward simulations were once again compared to experimental pressure trace data, with the EGR level varying from 5-20% (by mass), the results of which were presented in Figures 4.23-4.26. The upper limit for EGR was reduced for this case due to an increase in cyclic variability at the part-load condition.

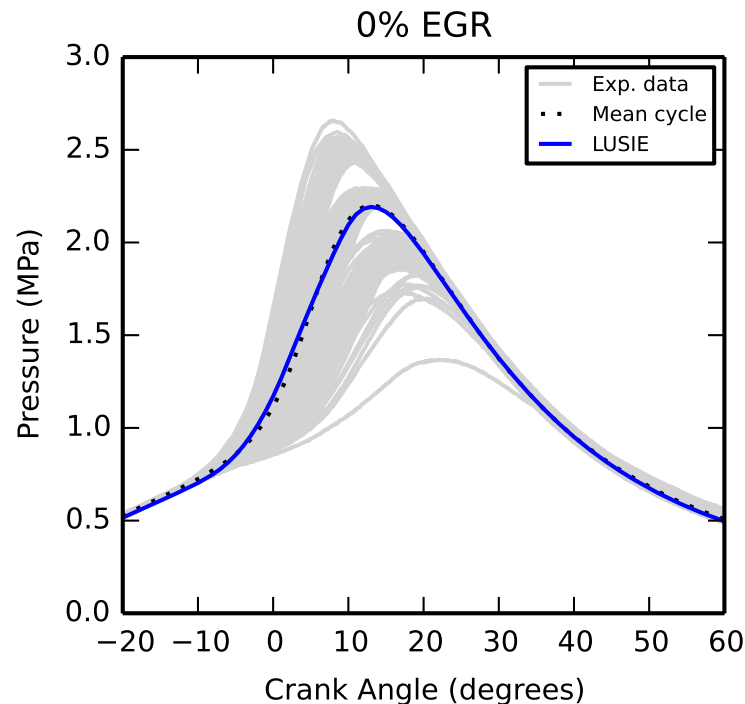


Figure 4.22: LUSIE simulated crank-resolved pressure trace with tuned constants and experimental data at 1500 rpm and GMEP of 0.36 MPa. Experimental data is comprised of 31 fast, 66 middle and 46 slow combustion cycles.

At 5% EGR the correlation presented in this study models a middle cycle with a lower peak pressure than the experimental mean. The model proposed by Bhattacharya *et al.* models a middle-slow cycle with the Rhodes & Keck model modelling

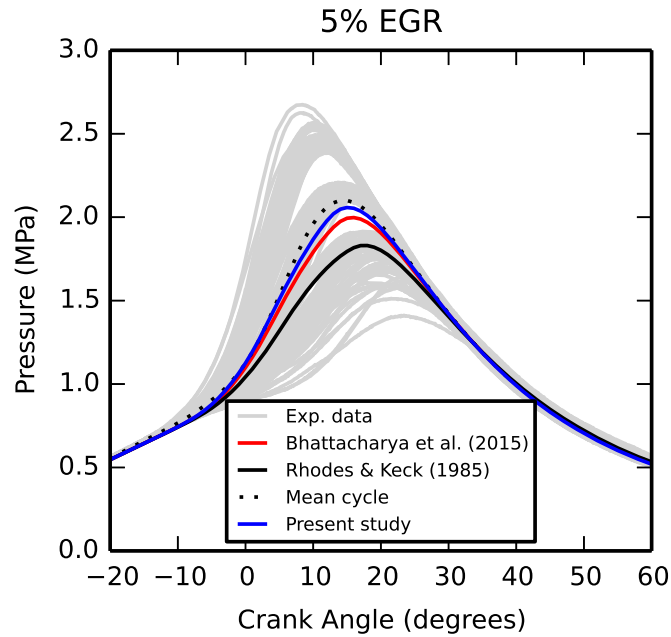


Figure 4.23: Simulated crank-resolved pressure trace comparing the correlation determined in the present study and models from the literature to experimental data at 5% EGR, 1500 rpm and GMEP of 0.36 MPa. Experimental data is comprised of 42 fast, 46 middle and 51 slow combustion cycles.

data within the slow combustion region of experimental data. From 10-20% EGR all models under-predict the peak pressure of the mean cycle, with the engine data correlation and Bhattacharya *et al.* model still predicting values that fall within experimental bounds. More precisely the Bhattacharya correlation models slow combustion cycles and the engine data correlation models middle-slow cycles. The Rhodes & Keck model is poor at predicting normal firing pressure traces, predicting instead the combustion instability zones.

Simulations for all the models have been undertaken and the RMS error calculated for the in-cylinder pressure values. The RMS error of in-cylinder pressure for the various models, at increasing levels of EGR, is presented in Figure 4.27. Once again the correction factor, determined under engine conditions, from this study has the lowest RMS error for most cases and performs the best overall. The Metghalchi & Keck model once again produces errors similar to those found within the present study at 5% EGR. However, the performance at increased levels of diluent is much poorer than the model derived in this study. The Bhattacharya *et al.* model simulates a slow combustion cycle throughout. The Rhodes & Keck and Fu *et al.* model perform poorly at any level of EGR beyond 5%.

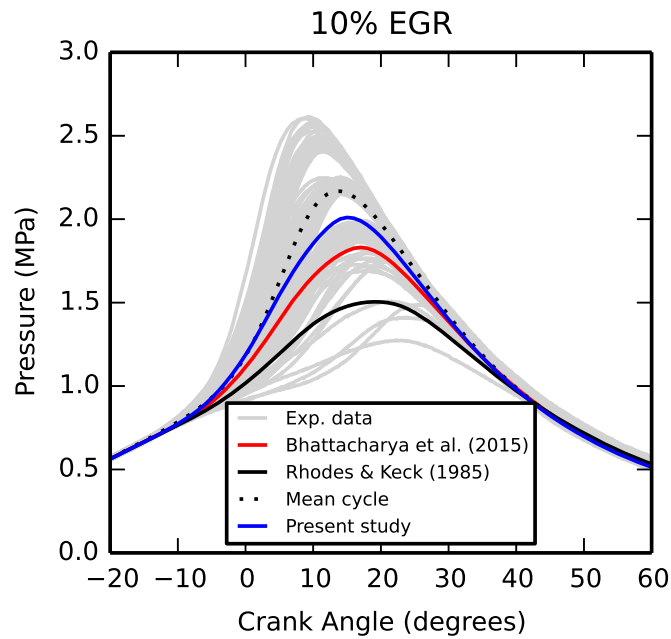


Figure 4.24: Simulated crank-resolved pressure trace comparing the correlation determined in the present study and models from the literature to experimental data at 10% EGR, 1500 rpm and GMEP of 0.36 MPa. Experimental data is comprised of 44 fast, 65 middle and 39 slow combustion cycles.

The model derived from the present study performs worse for the part-load case at 1500 rpm than the 0.79 MPa GMEP case. Analysis of the pressure traces shows that the early stages of combustion match or slightly over-predict the in-cylinder pressure. The pressure trace is then under-predicted as we approach the peak value. Therefore the rate at which mass is burned is slower than is experimentally observed. Although the tuned 0% EGR case in Figure 4.22 looks close to the mean cycle the same trend can be observed. A possible conclusion to be drawn from this is that if the rate of mass burned isn't correctly tuned for the 0% EGR case then any differences look to be exacerbated as the percentage of EGR increases.

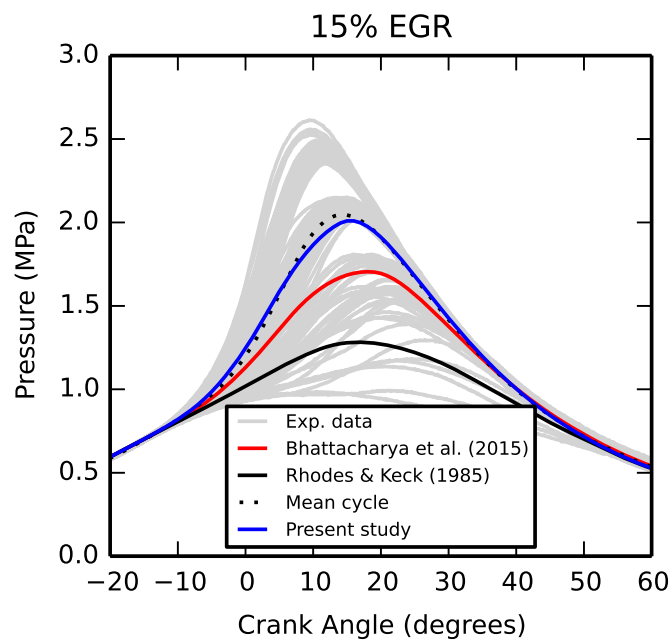


Figure 4.25: Simulated crank-resolved pressure trace comparing the correlation determined in the present study and models from the literature to experimental data at 15% EGR, 1500 rpm and GMEP of 0.36 MPa. Experimental data is comprised of 42 fast, 74 middle and 39 slow combustion cycles.

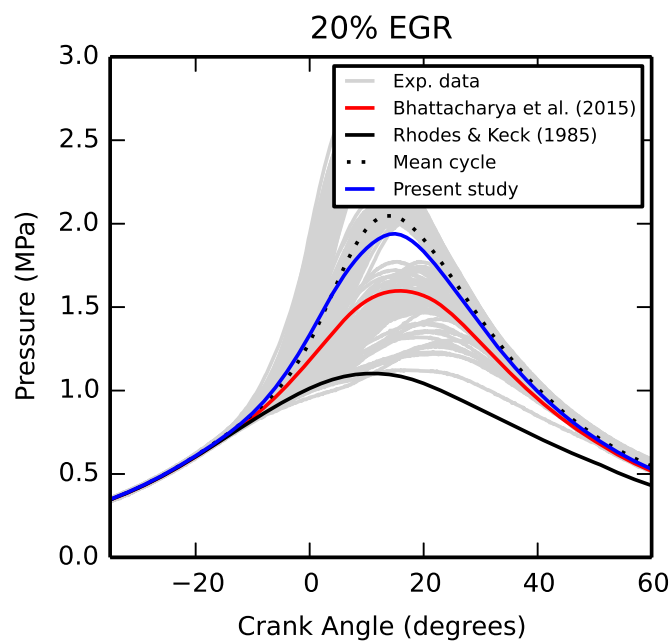


Figure 4.26: Simulated crank-resolved pressure trace comparing the correlation determined in the present study and models from the literature to experimental data at 20% EGR, 1500 rpm and GMEP of 0.36 MPa. Experimental data is comprised of 44 fast, 64 middle and 48 slow combustion cycles.

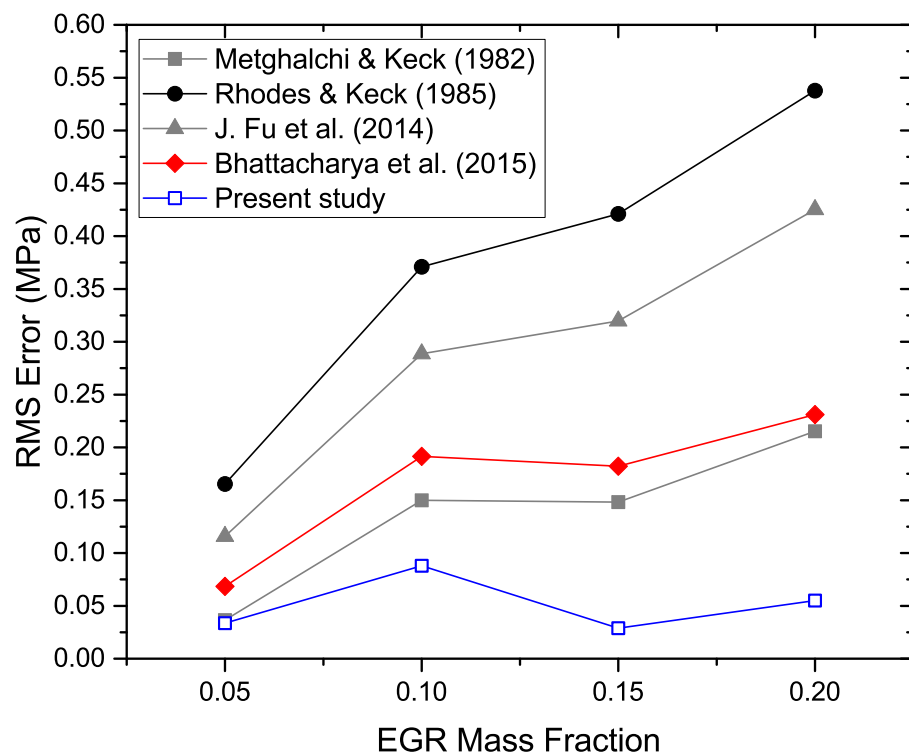


Figure 4.27: RMS error against measured pressure trace for varying levels of EGR for simulations at 1500 rpm and GMEP of 0.36 MPa.

### 4.4.3 2000 rpm, 0.98 MPa GMEP

A final comparison of the predictive capabilities of the correction factor proposed by this study and those found within the literature was investigated. The comparison was undertaken at an increased engine speed and load from which the correlation was back calculated. Like the two loads at an engine speed of 1500 rpm the 0% EGR case was tuned so that it would predict a mean combustion cycle. The tuned simulation, mean experimental pressure trace and pre-processed experimental data is presented in Figure 4.28. The pre-processed experimental data is divided into fast, medium and slow combustion cycles. The turbulent burning velocity constant was set to  $C_{ut} = 0.4$  and the characteristic burn up time constant was found to be  $C_{\tau_b} = 15$ . The tuned case shows a good agreement with the mean experimental cycle, with a small over prediction after peak pressure has been achieved. Most importantly the gradient of pressure increase matches that of the experimental mean cycle.

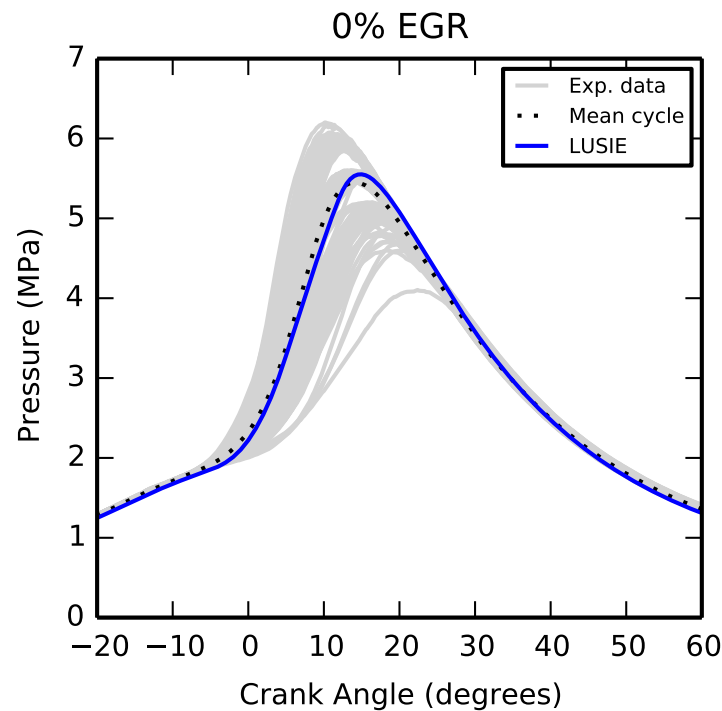


Figure 4.28: LUSIE simulated crank-resolved pressure trace with tuned constants and experimental data at 2000 rpm and GMEP of 0.98 MPa. Experimental data is comprised of 44 fast, 55 middle and 48 slow combustion cycles.

The predictive simulations were ran for an EGR sweep (5-20%) for each model from the literature as well as the correlation derived in this study. As with the the 1500 rpm cases the spark timing and intake pressure has been advanced and increased respectively to maintain engine load and MBT timing. Presented in Fig-

ure 4.29 are the forward simulations for the Bhattacharya et al. [2015] model, Rhodes and Keck [1985] model and the model described by Eq. (4.9) at 5% EGR. All three simulations fall within the experimental spread with the Rhodes and Keck [1985] correlation modelling the slowest combustion cycle. The Bhattacharya et al. [2015] model also models a marginally slow combustion cycle, improving on the Rhodes and Keck [1985] model. The model derived in the present study models a middle cycle and produces the closest simulated pressure trace to the mean.

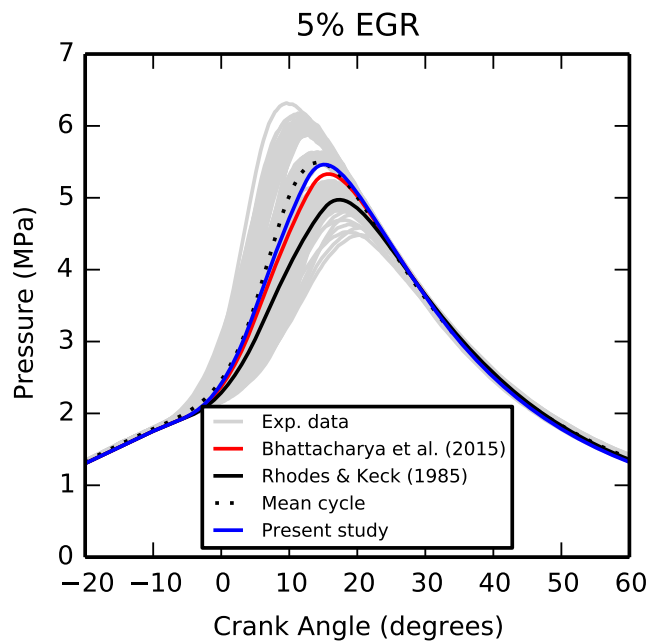


Figure 4.29: Simulated crank-resolved pressure trace comparing the correlation determined in the present study and models from the literature to experimental data at 5% EGR, 2000 rpm and GMEP of 0.98 MPa. Experimental data is comprised of 41 fast, 67 middle and 46 slow combustion cycles.

Presented in Figures 4.30 to 4.32 are the pressure trace simulations at 10, 15 and 20% EGR. The engine data correlation predicts the most accurate simulations for each level of EGR investigated. The pressure trace RMS errors for the models at 2000 rpm and 0.98 MPa GMEP is plotted in Figure 4.33. The smallest RMS errors occur at 10 and 15% EGR using the correlation derived here with only the Metghalchi & Keck model being close to matching the error values, and only for the 5% EGR case. Once again the engine data correlation performs best as it has done for the other two test points. These multiple validation points should therefore inspire some confidence in the model.

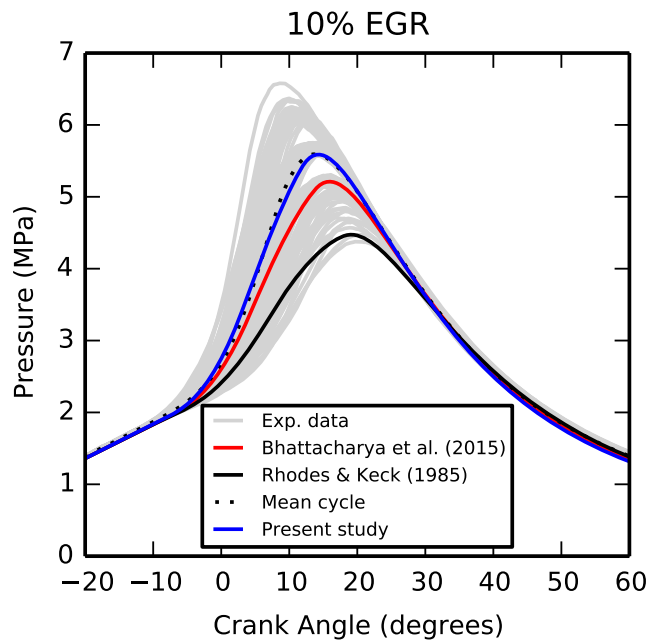


Figure 4.30: Simulated crank-resolved pressure trace comparing the correlation determined in the present study and models from the literature to experimental data at 10% EGR, 2000 rpm and GMEP of 0.98 MPa. Experimental data is comprised of 41 fast, 60 middle and 45 slow combustion cycles.

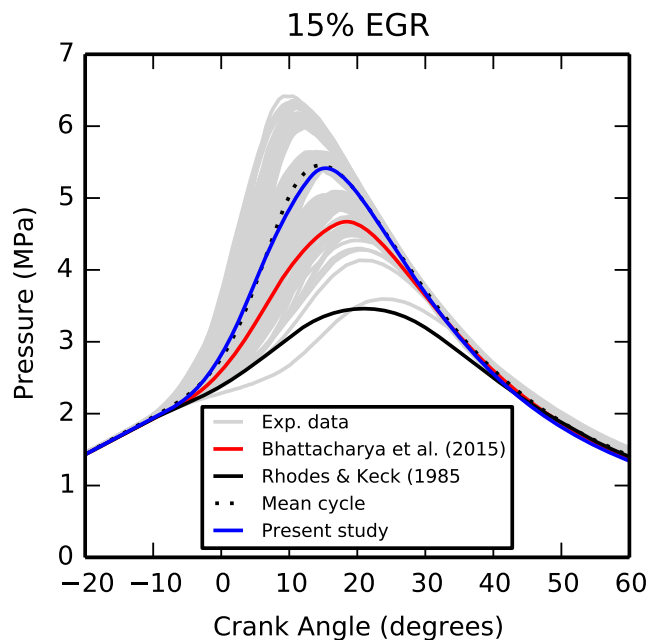


Figure 4.31: Simulated crank-resolved pressure trace comparing the correlation determined in the present study and models from the literature to experimental data at 15% EGR, 2000 rpm and GMEP of 0.98 MPa. Experimental data is comprised of 39 fast, 71 middle and 46 slow combustion cycles.

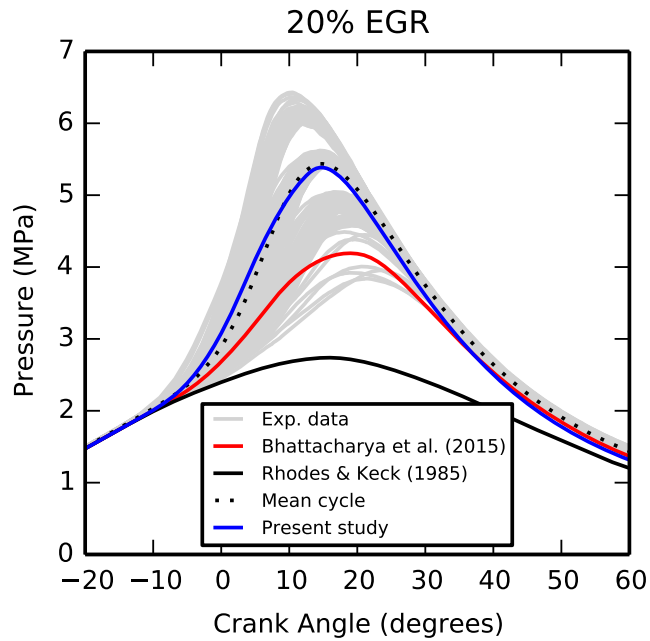


Figure 4.32: Simulated crank-resolved pressure trace comparing the correlation determined in the present study and models from the literature to experimental data at 20% EGR, 2000 rpm and GMEP of 0.98 MPa. Experimental data is comprised of 48 fast, 54 middle and 49 slow combustion cycles.

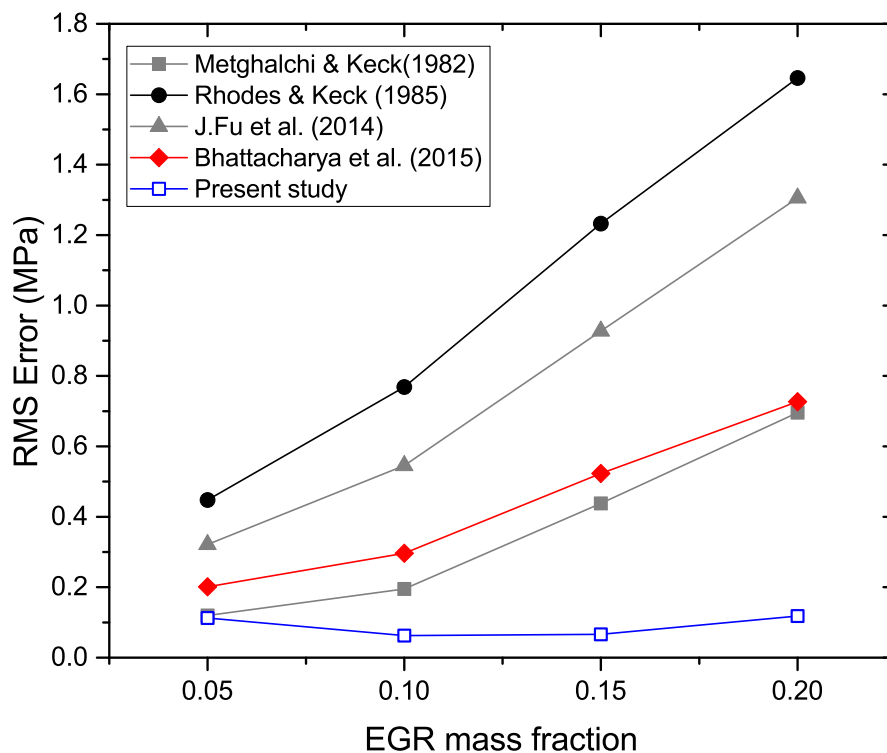


Figure 4.33: RMS errors for simulated pressure traces with respect to experimental mean cycle at 2000 rpm and GMEP of 0.98 MPa.

#### 4.4.4 Spark kernel delay time

Two user defined constants, the turbulent burning velocity constant,  $C_{ut}$ , and characteristic burn up time constant,  $C_{\tau_b}$ , have been tuned for the zero EGR case at the three speed/load conditions tested in this chapter. The EGR correction factor derived in this study prevented any further tuning of these parameters as the EGR mass fraction increased for each test point. However, one user defined parameter did require changing and that was the spark kernel delay time. The spark kernel delay is a user defined time taken for the spark kernel to reach a specified diameter. While this tuning is required to match the early flame development (0-2% mass fraction burned) the parameter has no effect on  $\frac{dm_b}{d\theta}$  and thus does not interact with burning velocities like  $C_{ut}$  and  $C_{\tau_b}$  do. Presented in Figure 4.34 is the kernel delay times plotted against EGR mass fraction.

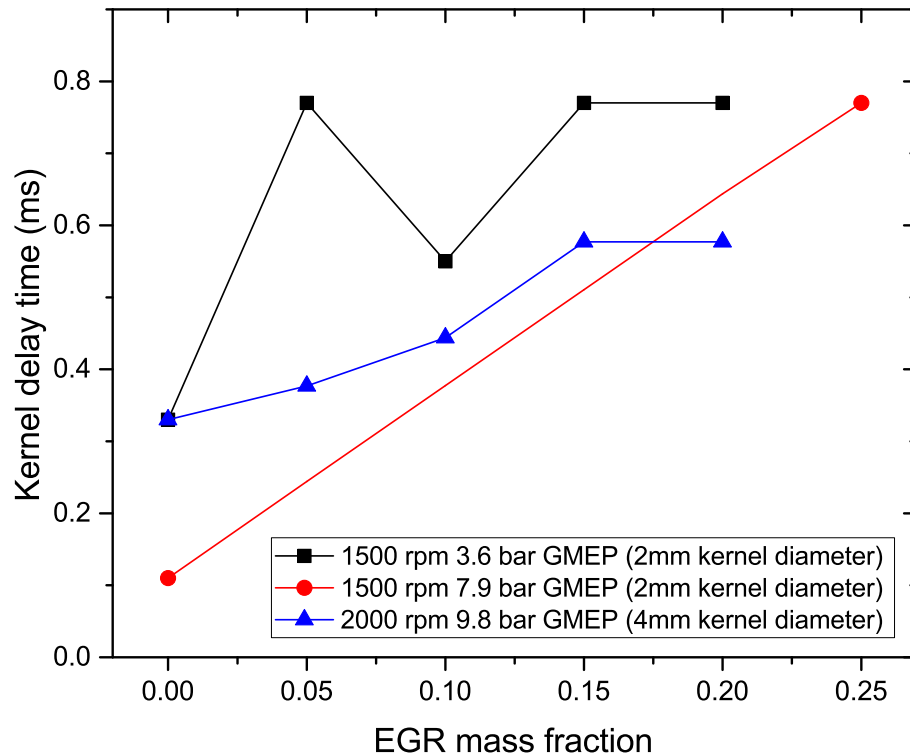


Figure 4.34: Spark kernel delay time at increasing mass fractions of EGR for three engine speed/load conditions.

It must be noted that for the 1500 rpm 0.79 MPa GMEP case that only the 0 and 0.25 mass fraction of EGR case was tuned, with the remaining values taken as a linear increase between the two. This reduced the amount of tuning done for that set of running conditions. For both the 1500 rpm 0.36 MPa GMEP and the 2000 rpm 0.98 MPa GMEP case each increment of EGR mass fraction was tuned. While the

two completely tuned cases did not increase linearly the general trend was an overall increase in spark kernel delay time with increasing EGR mass fraction. This is in agreement with the study by Robertson et al. [2018] who modelled the 0-2% mass fraction burned using a flame growth multiplier (FGM) which is analogous to the kernel delay time. Robertson et al. [2018] found that the FGM decreased as the level of EGR increased, which relates to an increase in kernel delay time. As the early flame development can be described as a laminar-like flame, and that the laminar burning velocity is reduced with EGR, it is unsurprising that the kernel delay time increases with increasing EGR and therefore a decreasing laminar burning velocity. The increase in spark kernel diameter for the 2000 rpm case to 4mm (from 2mm) was required by the code to enable it to calculate chemical equilibrium.

## 4.5 Chapter Summary

This chapter introduced a new method to determine correction factors for EGR from engine pressure trace data by using a reverse thermodynamic model. One advantage of using this technique to determine a correlation is that all exhaust gas species present in-cylinder can be accounted for. Using this approach, a new correlation for the effects of exhaust gas diluent on the laminar burning velocity of a EURO VI specification gasoline is derived and compared against existing models. The reduction in laminar burning velocity was found to be much less when compared to other published work. The correlation and models from the literature were then implemented into a predictive combustion code to compare their predictive modelling capabilities. The newly suggested correlation derived under engine conditions shows a good agreement to experimental pressure trace data over the full range of EGR (5-25% by mass) for the conditions upon which it was derived.

Bhattacharya *et al.* and Metghalchi & Keck models are the better performing models from the literature. In contrast, the models by Rhodes & Keck and Fu *et al.* give reasonable agreement at 5% EGR but suffer from rapidly rising errors for higher EGR levels. All models from the literature tend toward modelling slower cycles as levels of EGR increase, but for the Rhodes & Keck and Fu *et al.* model, this effect is much more pronounced.

The mass fraction burned simulations at 1500 rpm and 0.79 MPa GMEP correlated well to the experimentally derived mass fraction burned for the engine data correlation derived in this study. The RMS errors for the mass fraction burned simulations mirrored the pressure trace RMS error at these conditions. This is unsurprising as the pressure rise due to combustion is proportional to the heat re-

leased and the heat released is proportional to the mass burned. Like the pressure trace data the model derived in the present study performed the best at predicting the rate of mass burned. The best performing models from the literature were the Bhattacharya *et al.* and Metghalchi & Keck models.

Predictive simulations were ran under different load and speed conditions to confirm that the correlation presented here was robust and did not only provide reasonable predictions for the conditions upon which it was derived. The additional load and speed points were 0.36 MPa GMEP at 1500 rpm and 0.98 MPa GMEP at 2000 rpm. The model derived from engine data out-performed those from the literature for both of these running conditions, with once again models from the literature overestimating the effect of EGR on the laminar burning velocity. This is most likely associated to the fact that none of the models from the literature accounted for the full range of chemical species present in exhaust gas. This is in agreement with the study by Manna et al. [2017] who found that synthetic EGR leads to too great a reduction in laminar burning velocity compared to real exhaust gas.

# Chapter 5

## Stratified Fuel Model

---

### 5.1 Chapter Overview

The work presented in this chapter focussed on implementing a stratified fuel model into a pre-existing quasi-dimensional thermodynamic engine code. A radially varying equivalence ratio function, a turbulent mixing model and the effect of burned gas expansion were incorporated into the code. The model was then validated at an engine speed of 1500 rpm and engine load of 0.36 MPa GMEP for both the in-cylinder pressure and heat release. A homogeneous case under the same speed and load conditions acted as a comparison for the stratified model. Predictive modelling using the LUSIE simulation code then investigated the effect of increasing stratification for the same running conditions. Further to this both a centrally rich and centrally lean equivalence ratio profile was studied for both the weakly and strongly stratified case. The stratified fuel model was found to reproduce the qualitative trends found from experimental results within the literature.

### 5.2 Stratified charge

Due to the nature of the quasi-dimensional thermodynamic code the only point resolved in space is the location of the flame radius at the current time step. It is therefore not possible to incorporate a full 3-D fuel injection model, that accounts for a spatially and temporally varying equivalence ratio, as is the standard approach for CFD modelling. The stratification model makes two assumptions regarding the fuel injection process, these are:

1. At the end of injection (EOI), the fuel stratification has some initial profile given by a function  $\phi(r, 0)$ .
2. Turbulence mixes the charge, making it more homogeneous over time.

The effect of turbulent mixing in GDI engines is well established, with early injection timings utilised for the homogeneous operating mode. The rate of mixing is governed by turbulence as molecular diffusion on its own would not act sufficiently fast enough to create a homogeneous mixture. Using a distribution like this allows for the modelling of air, spray and wall-guided stratification processes. However, the effects of wall wetting are neglected for the wall guided case, which is the less favourable strategy for this reason.

It is important to control the fuel injected for the stratified case. Under homogeneous running conditions the in-cylinder mass is calculated by:

$$\text{mass} = \frac{PV}{R_0T} \cdot \sum_{i=1}^3 \text{mole fraction}(i) \cdot \text{molecular weight}(i) \quad (5.1)$$

where  $R_0$  is the molar gas constant, and the 3 species are oxygen, nitrogen and the fuel. The mole fraction of each species is governed by the fuel/air equivalence ratio. For the spatially varying mixture in the stratified operating mode the mean equivalence ratio is utilised and is calculated by:

$$\bar{\phi} = \frac{1}{R} \int_0^R \phi(r, 0) dr \quad (5.2)$$

where  $R$  is the cylinder radius.

The instability of combustion in a stratified charge is governed by convective flow fluctuations, preventing the flame kernel from propagating into the main stratified fuel cloud. This allows the fuel cloud to lean out due to transport and mixing effects (Fansler et al. [2015]). This leaning out then causes flame quenching at the edges of the fuel cloud (Zhao et al. [1999], Fansler and Drake [2008]). While lean quenching was not directly modelled here a possible solution suggested by the author would be to use the Karlovitz number as a threshold at which quenching occurs. For fuels with positive stretch rate Markstein number, quenching typically occurs at  $K \approx 0.8$  (Bradley et al. [2013]). The Karlovitz factor is inversely proportional to the square of the laminar burning velocity:

$$K \propto \frac{1}{u_l^2(\phi)} \quad (5.3)$$

with the laminar burning velocity a function of  $\phi$ . Therefore as the fuel mixture leans out, the laminar burning velocity decreases thus increasing the Karlovitz number.

### 5.3 Equivalence ratio distribution

To accurately model the fuel stratification the equivalence ratio must use a realistic mixture distribution function. As previously mentioned only the flame radii can be observed. Therefore, the model uses an initial distribution that is a function of the flame radius. Because of the radial distribution the model assumes that the flame propagates from a central point of ignition, where the mixture is rich, towards the cylinder walls, where the mixture becomes leaner.

The model by Abdi Aghdam [2003] investigated the use of arbitrary linear,

$$\phi = \phi_{max} - \left( \frac{\phi_{max} - \phi_{min}}{R} \right) \cdot r \quad (5.4)$$

and parabolic functions:

$$\phi = \phi_{max} - \left( \frac{\phi_{max} - \phi_{min}}{R^2} \right) \cdot r^2 \quad (5.5)$$

where  $\phi_{max}$  and  $\phi_{min}$  are the user defined maximum and minimum equivalence ratios respectively. These arbitrary functions have neither been validated through the use of predictive modelling nor has either distribution been established within the literature.

Moriyoshi et al. [1996] used a partitioned combustion chamber to achieve fuel stratification. The fuel was injected into one of the three partitions, creating a fuel rich zone. The partitions were then removed and after a set amount of time to allow some mixing the fuel was ignited. Shi et al. [2016] and Pires Da Cruz et al. [2000] conducted numerical studies into 1-D laminar stratified flames, with the former looking at hydrogen-air flames and the latter a methane-air flame. The equivalence ratio profiles looked remarkably similar for the three studies. Compared in Figure 5.1 is the spatial mixture distribution.

Figure 5.11 (b) and (c) also give some indication that the profile changes with respect to time, with (c) showing clearly how the maximum equivalence ratio and gradient of the equivalence ratio reduces with increasing time. It also shows how

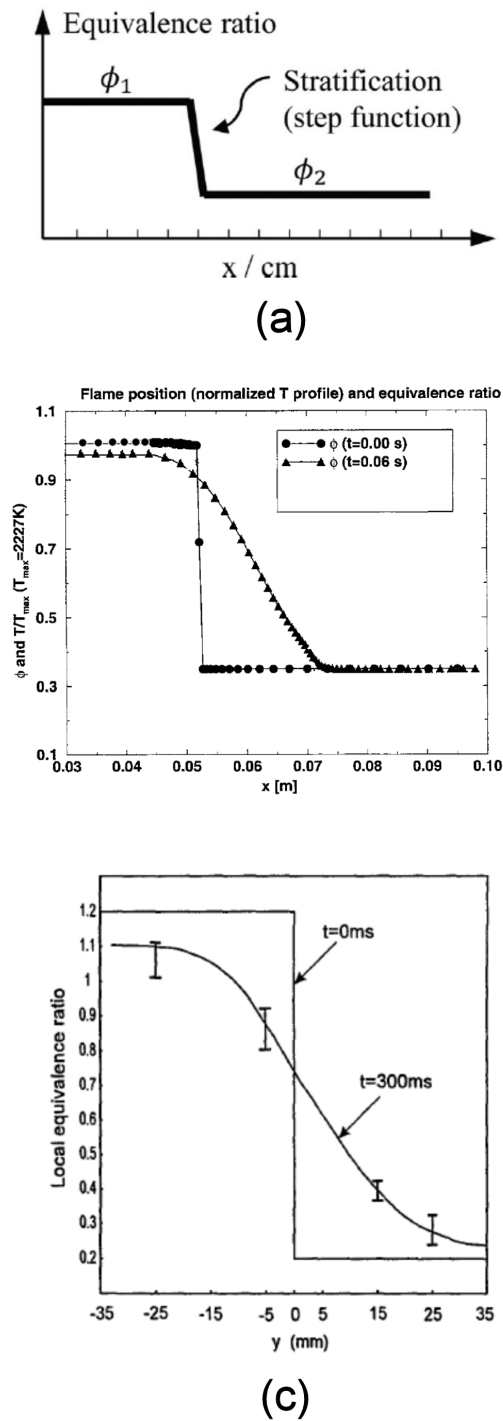


Figure 5.1: (a) Equivalence ratio profile taken from (a) Shi et al. [2016] (b) Pires Da Cruz et al. [2000] (c) Moriyoshi et al. [1996].

the minimum equivalence ratio increases over time.

Moriyoshi et al. [2003] again used a partitioned combustion chamber to achieve a stratified charge. The equivalence ratio profile data was recorded. The experimental

data was extracted and replotted as points. A function was fitted to best match the data points. The fitted function and data points extracted from Moriyoshi et al. [2003] are presented in Figure 5.2. The function describing the distribution of local

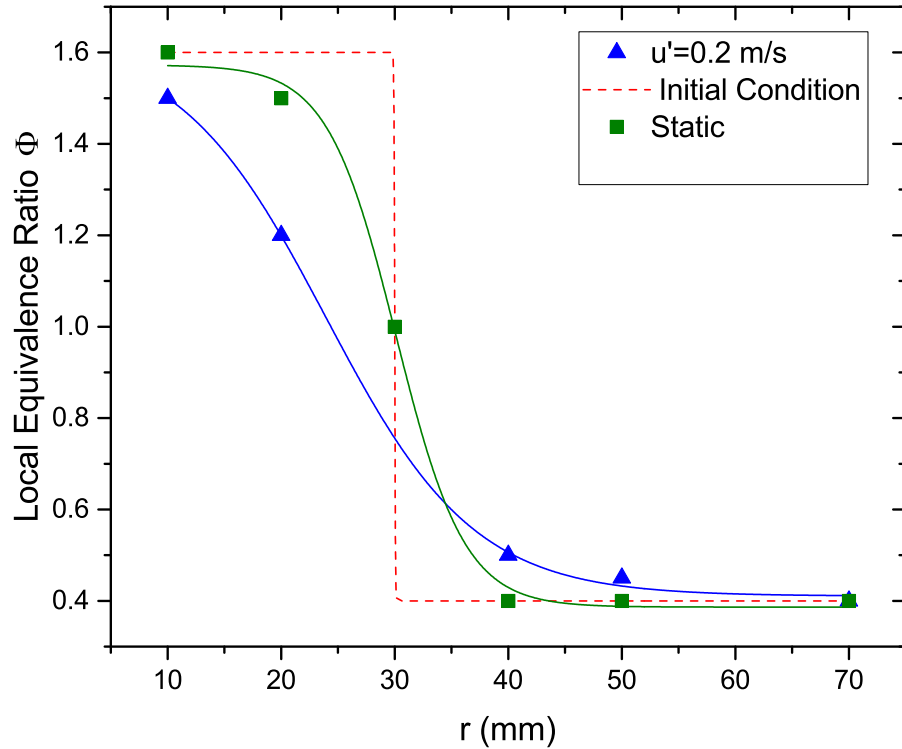


Figure 5.2: Data points taken from Moriyoshi et al. [2003] with fitted function.

equivalence ratio was found to be:

$$\phi = \phi_{min} + \frac{\phi_{max} - \phi_{min}}{1 + \exp\left(\frac{r+r_0}{dr}\right)} \quad (5.6)$$

where  $r_0$  and  $dr$  are constants for the time independent case.

While the equivalence ratio is significant, how it is utilised within the code is equally important. The stratified fuel model makes use of the three-zone burn up entrainment model based on the seminal work of Blizard and Keck [1974], which is described in section 3.2.3.3. The three-zone model requires updating to deal with the effects of fuel stratification. For example the rate of mass entrained is calculated using the unburned gas density, as the density of the gas in the entrainment zone is the same as the unburned gas for the homogeneous case. For the stratified case the mean equivalence ratio in the entrainment zone is utilised to calculate the entrained

gas density. The mean equivalence ratio of the entrainment zone is calculated by:

$$\bar{\phi}_e = \frac{1}{f_{re} - f_{rb}} \int_{f_{rb}}^{f_{re}} \phi(r, t) dr. \quad (5.7)$$

The mean equivalence ratio of the unburned gas zone also needs updating at each time step, and is calculated by:

$$\bar{\phi}_u = \frac{1}{R - f_{re}} \int_{f_{re}}^R \phi(r, t) dr \quad (5.8)$$

A schematic depicting how Eqs. (5.7) and (5.8) are incorporated into the three-zone combustion model is shown in Figure 5.3. The gradient of the unburned zone is is

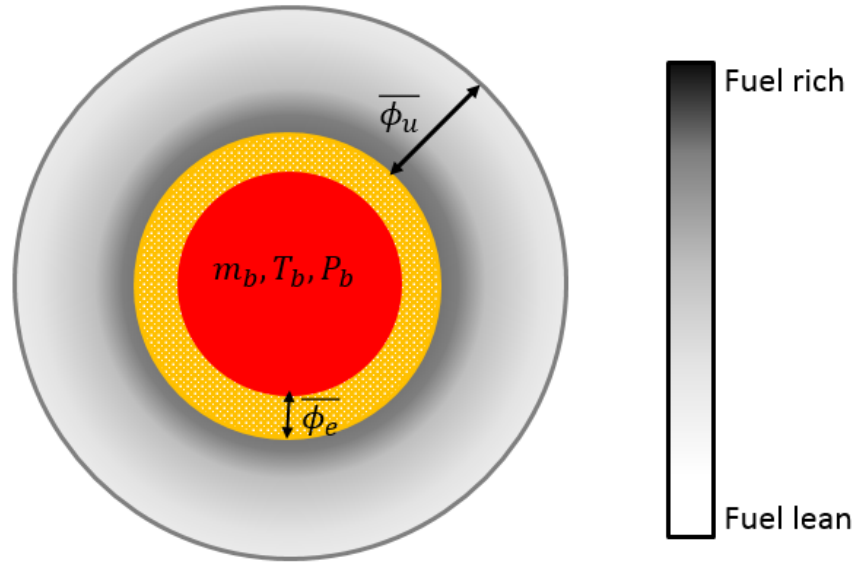


Figure 5.3: Graphical representation of adapted three-zone model for stratified case.

representative of the spatially varying fuel-air mixture. The equivalence ratio is also important in correctly modelling burning velocities. The laminar burning velocity is directly dependent on  $\phi$  and is updated within the code at each time step. However, combustion within an SI engine is predominantly turbulent. The equivalence ratio alters the predicted turbulent burning velocity using the following relation:

$$u_t \left( u_l(\phi(r, t)) \right) \quad (5.9)$$

## 5.4 Burned gas expansion

As the volume of the burned gas increases, the expansion of this gas pushes the unburned gas of a given equivalence ratio closer to the cylinder walls. This means that the initial equivalence ratio profile is altered by this expansion effect at each time step. How far the gas is translated in space can be expressed as:

$$\text{Translation} = r' - r \quad (5.10)$$

where  $r'$  is the location of an infinitesimal annular mass element of unburned gas after the burned gas expansion and  $r$  is the location of the annular element before displacement. A memory effect of stratification, which allows for a lean mixture to burn past the lean limit when it followed the burning of a rich mixture, has been observed experimentally (Balusamy et al. [2014]). The effect of burned gas expansion offers a possible explanation into the observed memory effect.

In a previous study by Abdi Aghdam [2003] the burned gas is assumed to expand cylindrically. However, in this study the flame was assumed to propagate spherically as it does for the homogeneous case. This assumption is supported by works of Drake and Haworth [2007] and Sementa et al. [2012], who found that the assumption of a spherically propagating flame holds for the stratified case. The volume of the unburned gas before expansion is:

$$V_{u1} = \pi r^2 h - V_{b1} \quad (5.11)$$

where  $V_{u1}$  is the volume of unburned gas between the burned gas radius and an arbitrary point in the unburned gas at radius  $r$ . The subscript one denotes before expansion.  $V_{b1}$  is the volume of burned gas before expansion and  $h$  is the swept height of the cylinder. The volume of unburned gas after expansion is:

$$V_{u2} = \pi r'^2 h - V_{b2} \quad (5.12)$$

where  $V_{u2}$  is the volume of unburned gas between the burned gas radius and a point in the unburned gas at radius,  $r'$ . The subscript two denotes after expansion, where  $V_{b2}$  is the volume of burned gas after expansion. By using the assumption that pressure and temperature of the unburned gas are spatially uniform and applying

the ideal gas law, a relation between the volumes can be derived:

$$\frac{V_{t2u}}{V_{t1u}} = \frac{V_{u2}(r')}{V_{u1}(r)} \quad (5.13)$$

where  $V_{t1u}$  is the total volume of unburned gas before expansion and  $V_{t2u}$  is the total volume of unburned gas after expansion. The unburned gas as a function of the radius then reads:

$$\frac{\pi R^2 h - V_{b2}}{\pi R^2 h - V_{b1}} = \frac{\pi r'^2 h - V_{b2}}{\pi r^2 h - V_{b1}} \quad (5.14)$$

where  $R$  is the cylinder radius. Rearranging for  $r$  and  $r'$  yields:

$$r = \left[ \frac{V_{b1}}{\pi \cdot h} + \frac{(\pi r'^2 h - V_{b2}) \cdot (\pi R^2 h - V_{b1})}{\pi h (\pi R^2 h - V_{b2})} \right]^{\frac{1}{2}} \quad (5.15)$$

and:

$$r' = \left[ \frac{V_{b2}}{\pi \cdot h} + \frac{(\pi r^2 h - V_{b1}) \cdot (\pi R^2 h - V_{b2})}{\pi h (\pi R^2 h - V_{b2})} \right]^{\frac{1}{2}} \quad (5.16)$$

The various radii and volumes defined here are shown schematically in Figures 5.4 and 5.5.

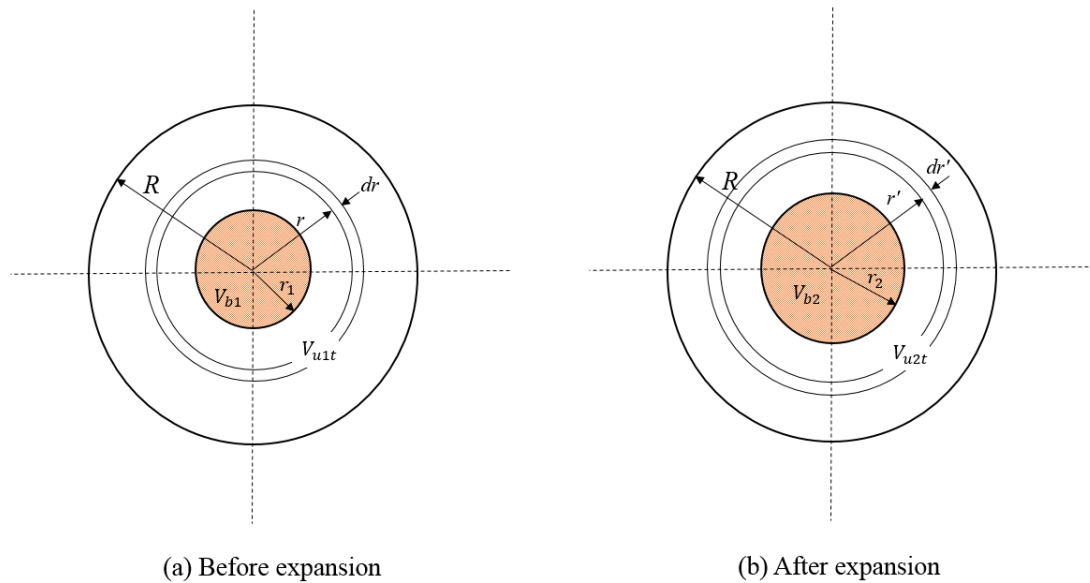


Figure 5.4: Unburned and burned zones before and after the burned gas expansion. Reproduced from Abdi Aghdam [2003].

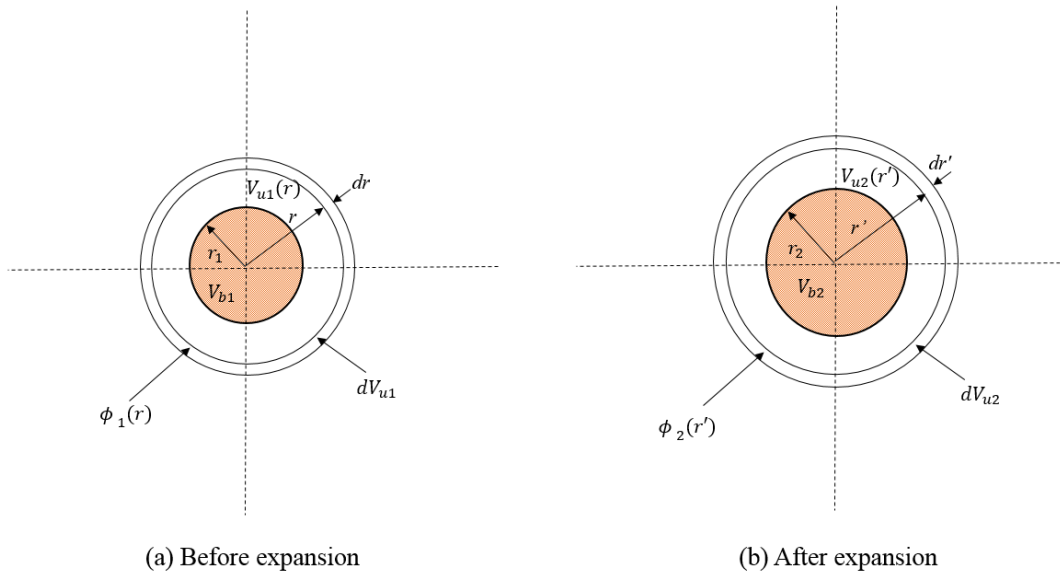


Figure 5.5: Infinitesimal elective annular element in the unburned zone before and after the burned gas expansion. Reproduced from Abdi Aghdam [2003].

## 5.5 Turbulent mixing

The fuel-air mixture for stratified charge varies temporally as well as spatially. After the point of injection, the fuel and air are mixing together due to diffusion. Molecular diffusion occurs too slowly to mix the in-cylinder charge. However, the time scale of mixing due to turbulent diffusion has been found to be comparable to the time scale of the combustion event (Serras-Pereira et al. [2015]). A dimensional argument comparing the typical rates of diffusion for both the molecular and turbulent case can be found in Tennekes and Lumley [1972].

The simplest way to model the effect of turbulent mixing was to use the one-dimensional diffusion equation using a turbulent diffusivity value  $D_t$ :

$$\frac{\partial \phi(r, t)}{\partial t} = D_t \frac{\partial^2 \phi(r, t)}{\partial r^2}. \quad (5.17)$$

The following boundary conditions were used to determine a solution to Eq. (5.17):

$$0 \leq r \leq L \quad (5.18a)$$

$$\frac{\partial \phi(0, t)}{\partial r} = 0 \quad (5.18b)$$

$$\frac{\partial \phi(L, t)}{\partial r} = 0. \quad (5.18c)$$

These boundary conditions were determined from experimental equivalence ratio profiles (Moriyoshi et al. [2003, 1996]). Eq.(5.18a) is derived from the charge varying radially outward from a central point at  $x = 0$ , to the cylinder walls at  $x = L$ . These boundary conditions for the mixture distribution are also met by the 1-D numerical models in the studies by Shi et al. [2016] and Pires Da Cruz et al. [2000]. The boundary conditions allow for an analytical solution to be determined:

$$\phi(r, t) = \phi_{eq} + A_n \cdot e^{-D_t k_n^2 t} \cdot \cos(k_n \cdot r) \quad (5.19)$$

where  $k_n$  is:

$$k_n = \frac{\pi}{L} \quad (5.20)$$

the equilibrium equivalence ratio  $\phi_{eq}$  is:

$$\phi_{eq} = \frac{\phi_{max} + \phi_{min}}{2} \quad (5.21)$$

and the parameter  $A_n$  is:

$$A_n = \phi_{max} - \phi_{eq} = \phi_{eq} - \phi_{min}. \quad (5.22)$$

The solution found in Eq. 5.19 is compared to the function derived from fitting the experimental data points found in Moriyoshi et al. [2003] (Eq. (5.6)). The two functions are compared in Figure 5.6. The initial distributions of the Fermi function and the turbulent mixing model show good agreement. The analytical solution derived therefore holds up to experimental results found within the literature.

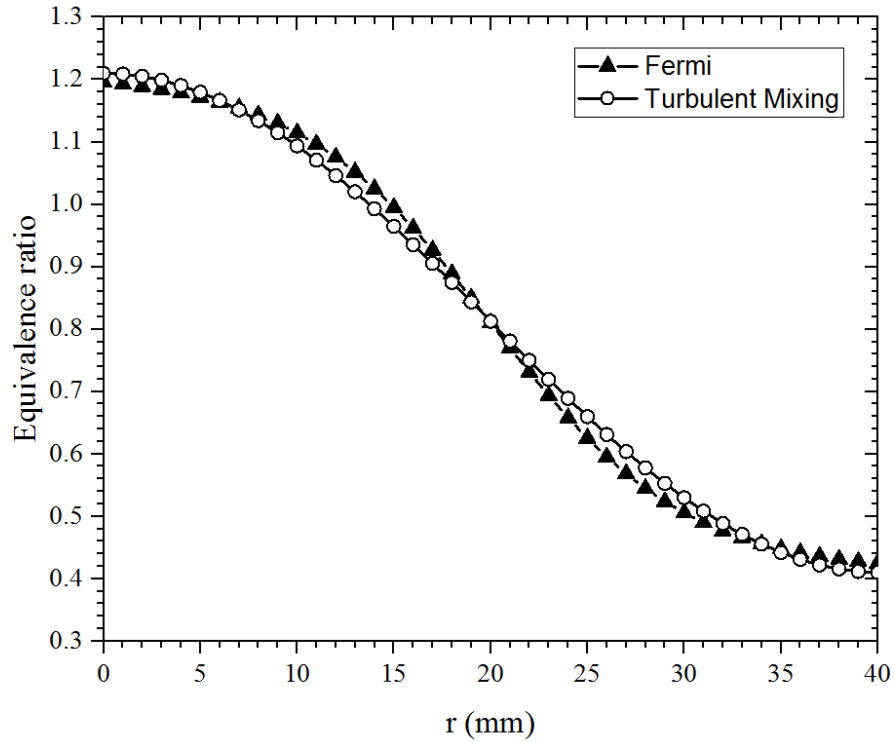


Figure 5.6: Initial equivalence ratio distributions ( $t=0$ ) for experimentally fitted Fermi function (Eq. (5.6)), with  $dr = 20$  and  $r_0 = 5$  and turbulent mixing model (Eq. (5.19)).

### 5.5.1 Turbulent diffusivity

While the initial spatial distribution matches experimental data, the turbulent diffusivity,  $D_t$ , must also be realistic to correctly model how the distribution changes in time. The turbulent diffusivity is given by Spalding and Launder [1972], Hill and Zhang [1994]:

$$D_{t,\infty} = \frac{C_\mu}{Sc_t} \cdot \frac{k^2}{\varepsilon} \quad (5.23)$$

where  $k$  and  $\varepsilon$  are the kinetic energy and turbulent dissipation, and  $Sc_t$  and  $C_\mu$  are the turbulent Schmidt number and a user defined constant, respectively. The diffusivity in Eq. (5.23) is taken from the Flame Speed Closure model of turbulent combustion. Like the Zimont-Lipatnikov turbulent burning velocity, the diffusivity has a flame development factor. The flame development factor models the influence of the different turbulent length scales on a propagating flame, with the concept being referred to as the effective turbulent RMS velocity in other models (Abdel-Gayed et al. [1984], Bradley et al. [2011]). The developing turbulent diffusivity is

given by:

$$D_t = D_{t,\infty} \left[ 1 - \exp\left(\frac{-t}{\tau_L}\right) \right] \quad (5.24)$$

where  $t$  is the time elapsed from spark and  $\tau_L$  is the integral time scale. The FSC model aims to capture the effects of the flame brush thickness. The magnitude of turbulent length scales relative to the flame brush thickness are therefore important. However, for this case all length scales on the turbulent spectrum will contribute to mixing the in-cylinder charge. Therefore, the developing turbulent diffusivity can be neglected and only the fully developed case need be utilised.

The parameters in Eq.(5.23) need to be linked to values that are obtainable in the LUSIE model. The turbulent kinetic energy can be expressed in terms of the turbulent RMS velocity:

$$k = \frac{1}{2} \left( u_x'^2 + u_y'^2 + u_z'^2 \right). \quad (5.25)$$

Due to the constraints of the quasi-dimensional model, isotropic turbulence is assumed so that

$$k = \frac{3}{2} u'^2. \quad (5.26)$$

Consequently the model cannot directly account for the coherent motions, swirl and tumble, that can prohibit or encourage mixing respectively (Berckmüller et al. [1996]). However, the user defined constant,  $C_\mu$ , in Eq. (5.23) may allow for this to be incorporated into the model at a later date.

The turbulent dissipation can be written in terms of the turbulent kinetic energy and therefore is also a function of the turbulent RMS velocity:

$$\varepsilon = C_\mu^{\frac{3}{4}} \cdot \left(\frac{3}{2} u'^2\right)^{\frac{3}{2}} \cdot L^{-1}. \quad (5.27)$$

Substituting Eqns. (5.26) and (5.27) into Eq.(5.23) gives:

$$D_{t,\infty} = \frac{\sqrt{6}}{2} \cdot \frac{C_\mu^{\frac{1}{4}}}{S_{c_t}} \cdot u' \cdot L \quad (5.28)$$

where  $L$  is integral length scale when applied to the flame brush thickness in the FSC model (Huang et al. [2014a]). Here, the length scale used for  $L$  is the cylinder radius,  $R$ .

Figure 5.7 highlights the difference in computed equivalence ratio using both the turbulent mixing and burned gas expansion models (red circles) and just the turbulent mixing model (green triangles). The grey lines demonstrate how the equivalence ratio profile reaches an equilibrium as time increases due to the effect of turbulent mixing.

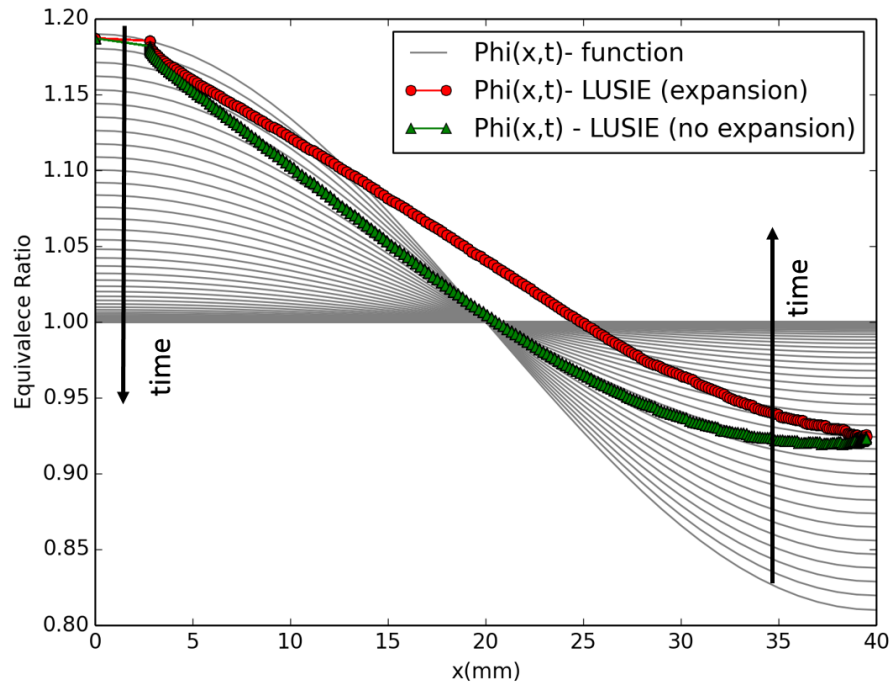


Figure 5.7: Equivalence ratio distributions calculated by LUSIE for turbulent mixing with and without burned gas expansion.

### 5.5.2 Fuel injection timing

The stratified mode of operation utilises a late injection timing strategy. Although this late timing is typical for all stratified charge SI engines, the exact point for the start and end of injection is variable. It is important to incorporate the injection timing to model the mixing that occurs between the end of injection and ignition timing, giving an accurate fuel distribution at the start of the combustion process. Therefore while the start of injection (SOI) is important with regards to injection duration, the parameter of interest is the in-cylinder charge distribution at the end of injection, and how this is altered in the lead up to ignition.

Due to the nature of the LUSIE code, the mixing between injection and ignition has to be modelled using the mean turbulent diffusivity between the two events.

The change in mixture distribution between the end of injection and ignition timing can be expressed as:

$$\phi(r, t) = \phi_{eq} + A_n \cdot e^{-D_t(\bar{u}')k_n^2(t_{ign}-t_{EOI})} \cdot \cos(k_n \cdot r) \quad (5.29)$$

where  $t_{ign}$  is the ignition time and  $t_{EOI}$  is the time at the end of injection. The turbulent diffusivity is based on the mean turbulent RMS velocity during the time interval.

While this model simulates the mixing between the EOI and ignition it was not used in this study to allow for greater user control of the equivalence ratio distribution at the point of ignition.

## 5.6 Stratified model validation

The stratified fuel model was validated against experimental data for both pressure trace and heat release at an engine speed of 1500 rpm, engine load of 0.36 MPa GMEP and an overall stoichiometric fuel:air equivalence ratio. This speed and load is a typical operating point for stratified combustion (see Figure 2.13.). To confirm that the experimental data was stratified the exhaust gas temperatures and emissions were compared to the homogeneous case for the same speed and load conditions, as no optical data was available. The exhaust gas data for both the homogeneous and stratified case is presented in Table 5.1.

Table 5.1: Exhaust gas data at 1500rpm and 0.36 MPa GMEP

| Parameter                   | Homogeneous | Stratified |
|-----------------------------|-------------|------------|
| Exhaust temperature (°C)    | 461         | 507        |
| NOx flow (g/hr)             | 23          | 12.5       |
| CO flow (g/hr)              | 56          | 130        |
| CO <sub>2</sub> flow (g/hr) | 1800        | 1822       |
| O <sub>2</sub> flow (g/hr)  | 51.5        | 118        |

The increase in CO when compared to the homogeneous case is indicative of incomplete combustion associated with a stratified charge (Lumley [1999]). This poor combustion occurs in the presence of a rich mixture where the fuel:air equivalence ratio  $> 1$ . It also leads to the excess O<sub>2</sub> found in the exhaust. The NOx flow decreased for the stratified case, which could be attributed to operating at near

stoichiometric conditions. The mixture was also likely to be weakly stratified due to having a high activity combustion chamber, resulting in a relatively lean mixture as opposed to an extremely lean mixture/air near the walls.

Simulations for both the stratified case and homogeneous case were run for the same engine speed and load. The purpose of running homogeneous and stratified was to see if the model captured any qualitative differences between the two modes of operation. The initial conditions for the experimental cycles can be found in Table 5.2.

Table 5.2: Running conditions for homogenous and stratified experimental data.

| Parameter                                  | Homogeneous | Stratified |
|--|-------------|------------|
| $P_{int}$ (MPa)                            | 0.07        | 0.073      |
| $T_{int}$ (K)                              | 403.2       | 403.2      |
| Spark advance ( $^{\circ}$ bTDC)           | 20          | 20         |
| Start of fuel injection ( $^{\circ}$ bTDC) | 300         | 50         |
| End of fuel injection ( $^{\circ}$ bTDC)   | 293         | 43         |

For the simulated stratified case, the maximum equivalence ratio was set to 1.28 and the minimum equivalence ratio set to 0.68. The minimum equivalence ratio was chosen as 0.68 as the engine has a high activity chamber, meaning that the charge near the walls would not be as lean as is usually associated with a stratified charge. The maximum equivalence ratio was selected to ensure that the average equivalence ratio was equal to the average experimental equivalence ratio for the stratified case. Due to a lack of any optical data, both the minimum and maximum equivalence ratios are weakly constrained and subject to substantial uncertainty. However, results were relatively robust, with variations of  $\pm 10\%$  still being well within experimental bounds. A study into various stratification profiles is presented in Section 5.7.

The crank resolved pressure trace for the homogeneous case simulation is presented in Figure 5.8. This was to prove the predictability of the model under different running conditions. The simulation is compared to the experimental mean cycle and a 95% confidence interval that is generated utilising the standard deviation of the maximum pressure trace value. The homogeneous simulation predicts a fast combustion cycle and predominantly falls within the 95% confidence interval. The simulation does fall within the experimental cycles for the whole cycle (see Smith et al. [2018]).

Compared in Figure 5.9 are the crank resolved pressure profiles for the simulated and experimental mean cases under stratified running conditions.

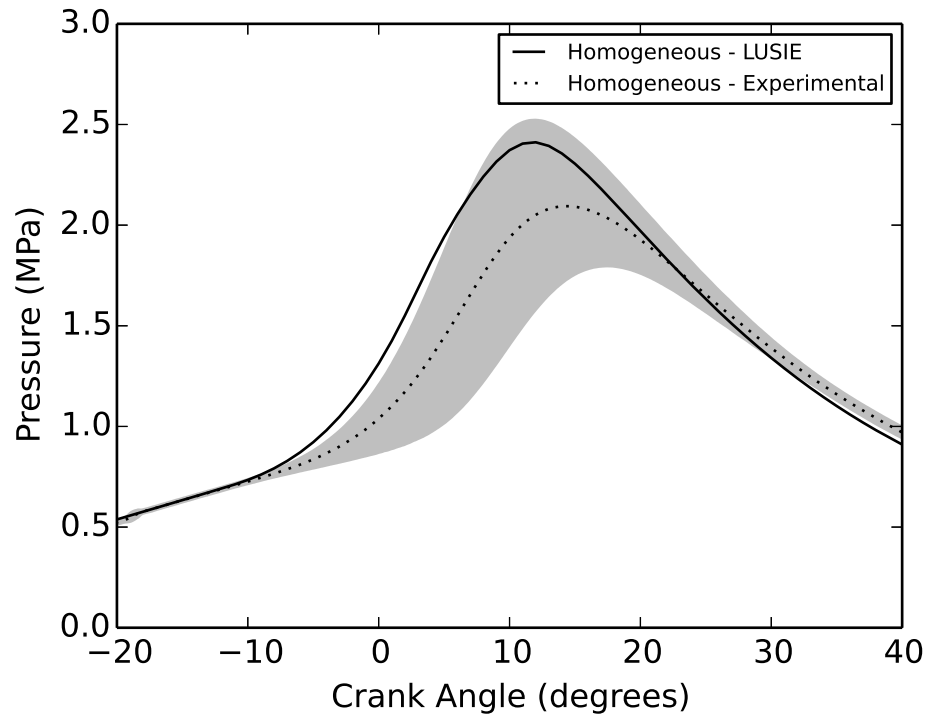


Figure 5.8: LUSIE simulated crank-resolved pressure trace, mean experimental cycle and 95% confidence interval at 1500 rpm and GMEP of 0.36 MPa.

The stratified simulation had a reasonable agreement with the experimental data, falling within the 95% confidence interval. The simulation represents a fast combustion cycle just as the homogeneous case does for the same engine speed and load in Figure 5.8. The difference in peak pressure,  $\Delta P_{max}$ , and peak pressure location,  $\Delta P_{\theta}$ , between the stratified and homogeneous simulated cycles is 0.113 MPa and  $-1^{\circ}$ , respectively. For the experimental mean cycles  $\Delta P_{max}$  equals 0.118 MPa and  $\Delta P_{\theta}$  equals  $-2.2^{\circ}$ . The model therefore captures the small increase in peak pressure due to stratification to a good degree of accuracy. The point at which the peak pressure value occurs is less well predicted by the model, the cause of which is attributed to a slower burning velocity most likely due to the weakly constrained fuel/air mixture distribution.

The effect of turbulent mixing on the equivalence ratio profile was investigated. Stratified simulations were undertaken with the mixing model switched off. The results for the non mixing case led to a  $\Delta P_{max}$  value of 0.173 MPa and a  $\Delta P_{\theta}$  value of  $0^{\circ}$ , compared to the homogeneous case. The decrease in peak pressure and same peak pressure location does not follow the experimental trend when comparing the stratified and homogeneous cases. It could therefore be concluded that turbulent mixing plays an important role in modelling stratified combustion.

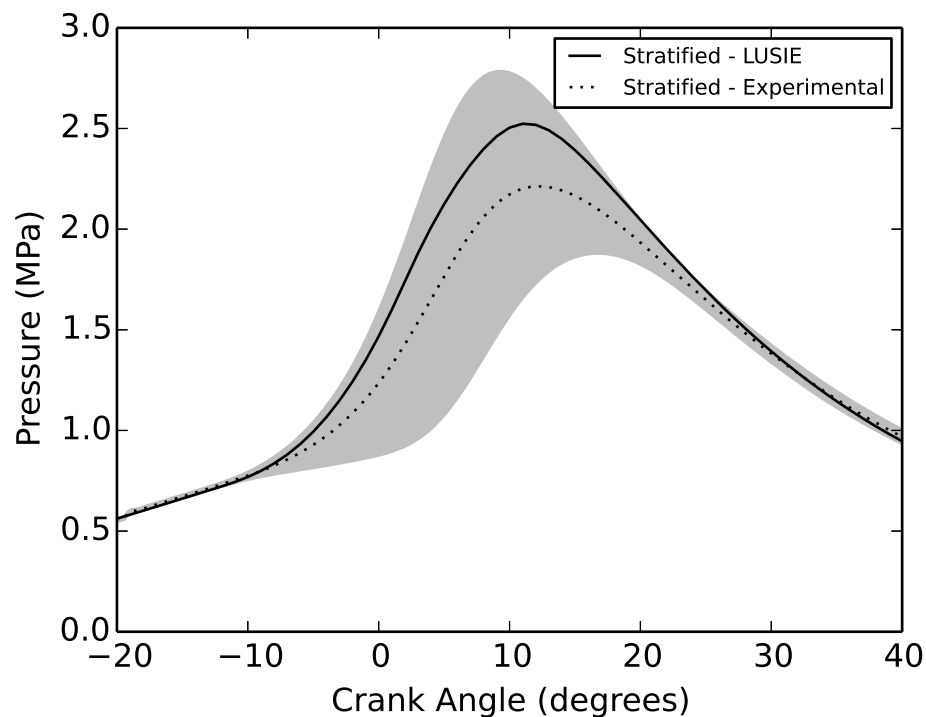


Figure 5.9: LUSIE simulated crank-resolved pressure trace, mean experimental cycle and 95% confidence interval for the stratified case at 1500 rpm and GMEP of 0.36 MPa.

A second point of validation for the model was the crank-resolved heat release. The heat release for the simulated case was calculated using a normalised mass fraction burned. The parameter was normalised due to the incomplete combustion of the mixture for the stratified case. The heat release for the experimental case is derived from the pressure trace data and is calculated using Eq. (4.16). Compared in Figure 5.10 are the crank-resolved heat release profiles for the modelled and experimental cases under stratified conditions. The predicted heat release falls well within the experimental bounds, and like the pressure trace profile show in Figure 5.9, represents a fast combustion cycle. It is worth stressing that the model constants  $C_{\tau_b}$  and  $C_{ut}$  from Eqs. (3.5) and (3.13), respectively, have required no further tuning from the initial homogeneous case.

## 5.7 Predictive stratified modelling

Predictive studies using the LUSIE code were carried out once the stratified fuel model had been validated. This section describes the predictive stratified simulations. Two investigations were carried out using predictive stratified simulations.

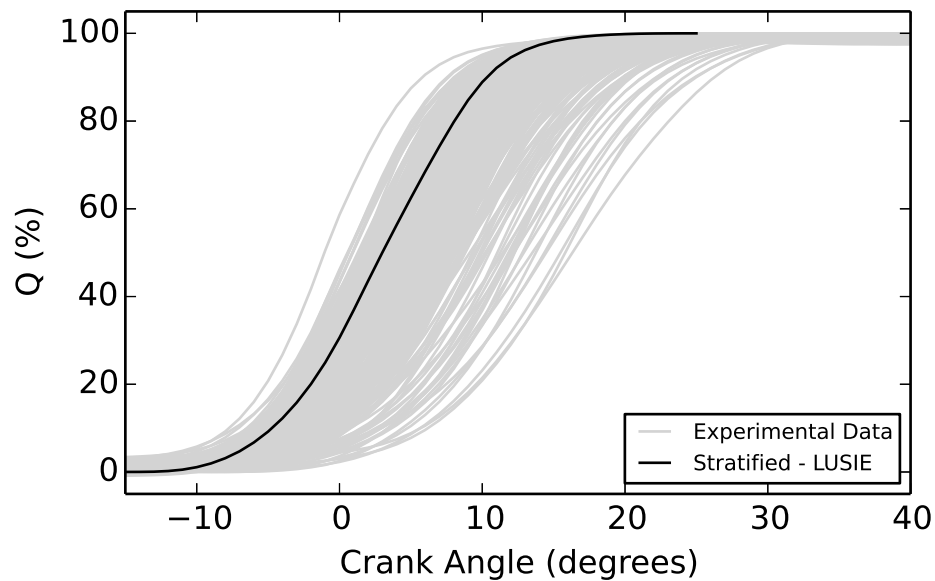


Figure 5.10: Percentage heat release for the simulated and experimental case under stratified conditions at 1500 rpm and GMEP of 0.36 MPa.

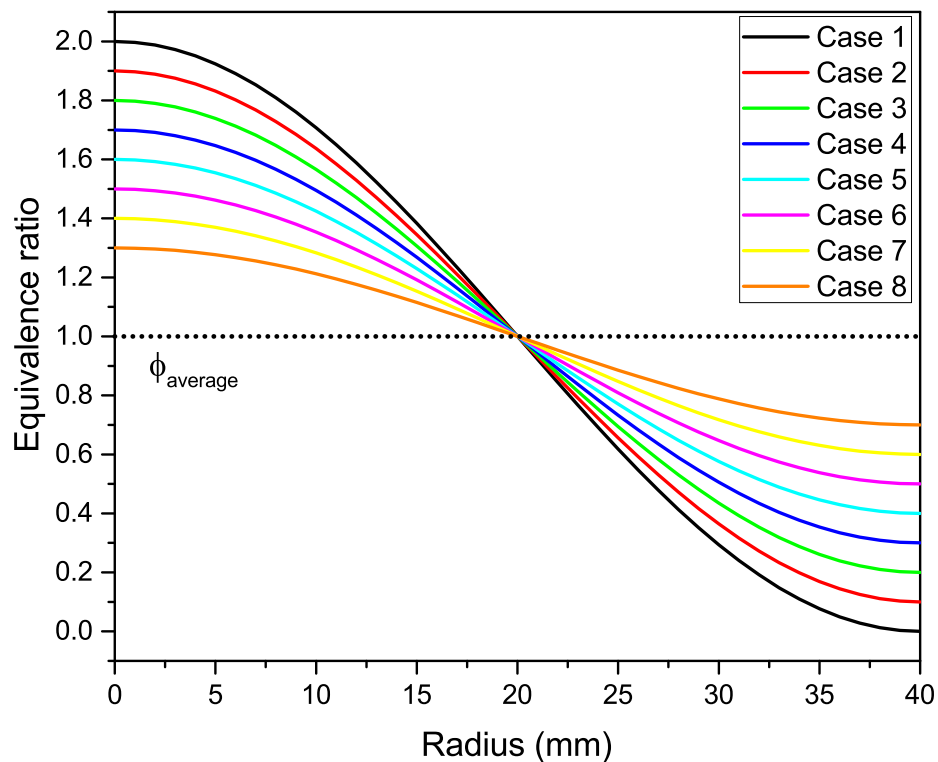
The first study focussed on the effect of increasing stratification levels on combustion parameters. The second study looked to compare the differences between a centrally rich and a centrally lean stratified mixture.

### 5.7.1 Varying stratification level

The effect of varying levels of stratification on in-cylinder combustion parameters was analysed for 8 different cases. The average equivalence ratio,  $\phi_{av}$ , for this parametric study was kept at a constant stoichiometric value with the minimum and maximum equivalence ratios varied for each case. The maximum and minimum equivalence ratio for each of the cases investigated in this study is presented in Table 5.3. The initial radial distributions of these cases are shown graphically in Figure 5.11. The in-cylinder combustion parameters analysed for the increasing stratification were: pressure, mass fraction burned, mean laminar burning velocity, mean entrainment burning velocity and maximum burned gas temperature. The crank resolved in-cylinder pressure for a selection of the cases are presented in Figure 5.12. Increasing the level of stratification reduced the in-cylinder pressure for the same running conditions. It was found that peak pressure occurs later for greater stratification. Overall the greater the stratification the slower the combustion cycle. In the validation of the stratified model the pressure profile represented a fast cycle. It therefore seems possible that the arbitrary equivalence ratio profile chosen could be tuned to find a pressure profile that better reflects the mean cycle. Presented

Table 5.3: Cases for varying stratification

| Case no. | $\phi_{max}$ | $\phi_{min}$ |
|----------|--------------|--------------|
| 1        | 2.0          | 0.0          |
| 2        | 1.9          | 0.1          |
| 3        | 1.8          | 0.2          |
| 4        | 1.7          | 0.3          |
| 5        | 1.6          | 0.4          |
| 6        | 1.5          | 0.5          |
| 7        | 1.4          | 0.6          |
| 8        | 1.3          | 0.7          |

Figure 5.11: Radially varying initial ( $t=0$ ) equivalence ratio for cases 1-8.

in Figure 5.13 is the crank resolved pressure traces for cases 3 and 8 compared to experimental mean cycle, with case 8 being almost identical to the distribution used in the model validation. Although more information would be required on the initial distribution, and possibly further validation, for the model to be fully predictive Figure 5.13 shows that the stratified fuel model is capable of predicting a pressure trace close to the mean experimental cycle.

The crank resolved mass fraction burned, presented in Figure 5.14, provides some insight into the lower peak pressures associated with the highly stratified cases. The stronger stratification appears to result in less of the gas being burned, which is

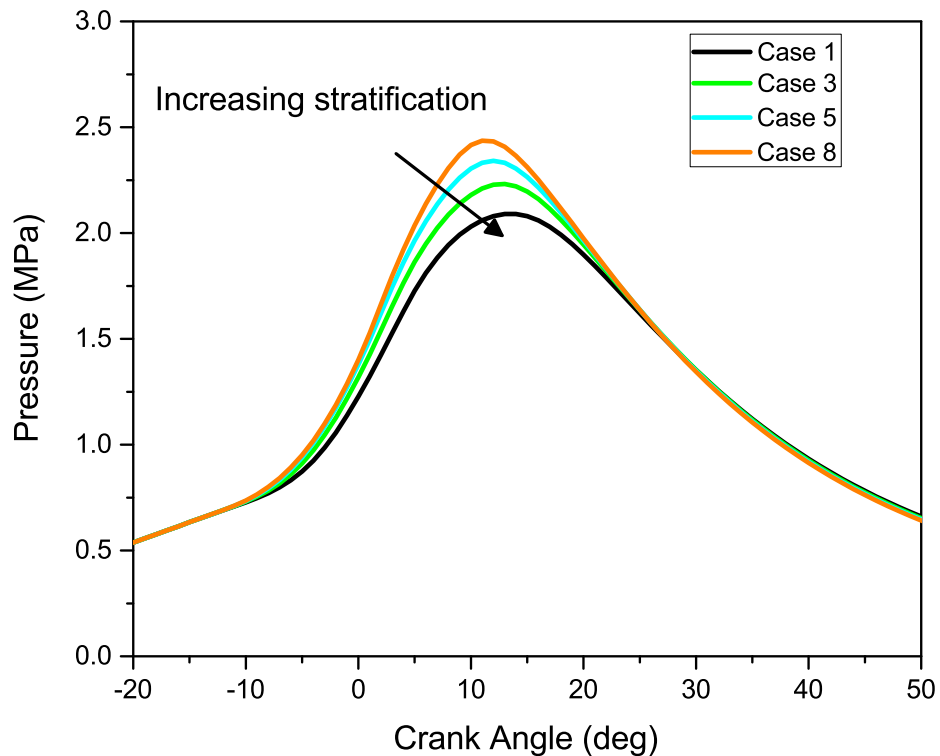


Figure 5.12: Crank resolved in-cylinder pressure profiles for increasing stratification at 1500 rpm.

in agreement with the findings by Robeck and Ellzey [1998]. The increase in the amount of unburned mass will also lead to an increase in the level of unburned HC emissions.

The reduction in mass burned for greater stratification also effects the maximum burned gas temperature. The maximum burned gas temperature for each case is presented in Figure 5.15 where it is shown that increasing stratification reduces the maximum burned gas temperature. The formation of NO<sub>x</sub> emissions is dependent upon both the temperature and oxygen concentration, with temperature being the dominant factor. Although this is unlikely based on the difference in temperature being relatively small.

Referring back to Figure 5.14, it is clear that the rate of mass burned decreases for increasing stratification. The investigation into burning velocities has been investigated further with the mean laminar and mean entrainment burning velocities compared for each case. The laminar burning velocity is dependent upon the equivalence ratio, pressure and temperature, with each one of the cases having quite different time resolved laminar burning velocity profiles. These different profiles are difficult to compare, hence the mean value has been analysed to resolve this issue. The mean laminar burning velocity for each case is presented in Figure 5.16. Over-

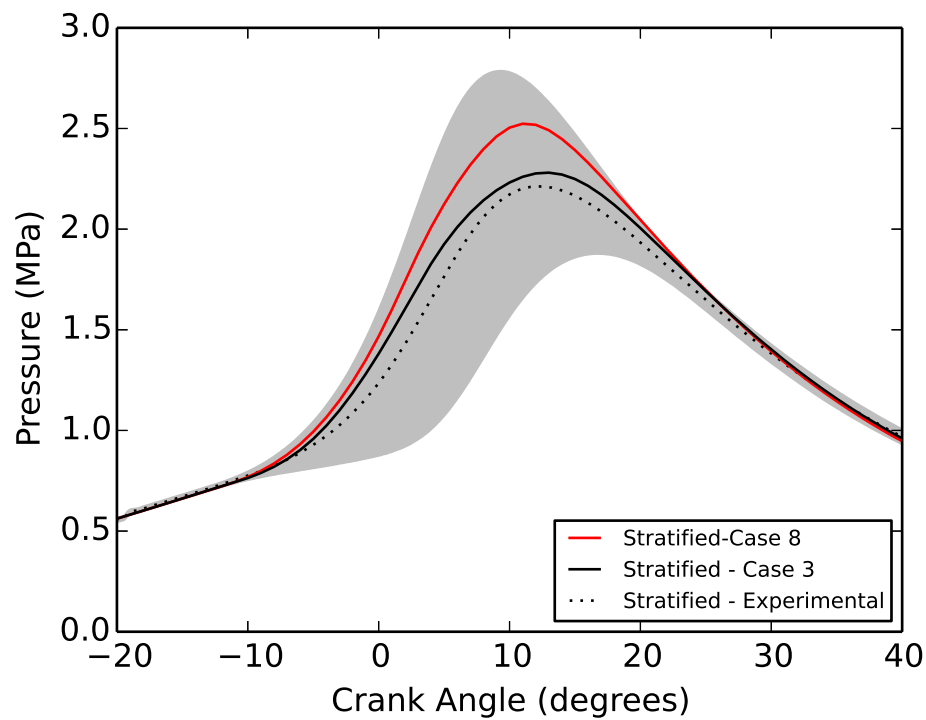


Figure 5.13: Comparison of pressure profiles for case 8 (used for stratified model validation) with case 3 at 1500 rpm.

all the trend shows that increasing stratification reduces the mean laminar burning velocity, although case 8 does not follow this trend. For case 8 the laminar burning velocity is greater during early stages where turbulence is greatest (due to the decaying nature of turbulence). The flame therefore propagates faster resulting in the increase in pressure trace and mass burned. Because of the speed of flame propagation the flame quickly reaches a point close to the wall leading to a long duration of laminar burning velocity at low values, which explains the lower mean value.

The mean turbulent entrainment velocity for each case is presented in Figure 5.17. The increase in stratification again leads to a reduction in velocity. This complies with overall trend for increased levels of stratification, which essentially leads to a reduction in numerous in-cylinder combustion parameters. More specifically, the parameters that have been observed to be reduced due to increasing stratification are: peak pressure, mass burned, maximum burned gas temperature, mean laminar and turbulent entrainment burning velocities. Increasing the stratification limits the range in which the flame propagates close to an optimal equivalence ratio value. This optimum zone has been defined as  $0.9 \leq \phi \leq 1.1$ . This range was chosen as the laminar burning velocity is at least 90% of the maximum burning velocity, for the same pressure and temperature. A plot of the crank equivalence ratio distributions from LUSIE is presented in Figure 5.18. The graph shows the duration

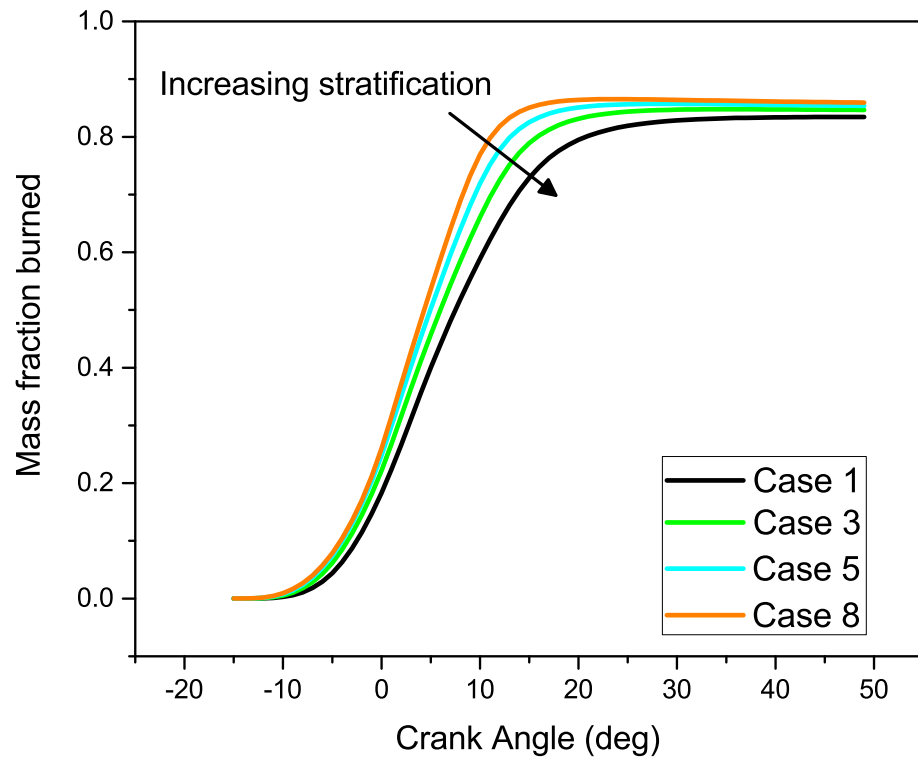


Figure 5.14: Crank resolved mass fraction burned profiles for increasing stratification at 1500 rpm.

each case has within the optimal equivalence ratio zone. The greater the length of time that the equivalence ratio is in the optimal range the faster the combustion and the greater the in-cylinder pressure. It is worth noting that the effect of expansion and mixing is accounted for.

### 5.7.2 Rich-lean and lean-rich stratification profiles

Fuel stratification in engines typically involves a rich mixture in close proximity to the spark plug, with the mixture becoming leaner as the charge approaches the cylinder walls. While a lean-rich mixture (where the mixture near the spark is lean and the mixture near the walls is rich) may be difficult to achieve practically, it is theoretically investigated in this section and compared to the rich-lean mixture typically associated with stratified engine combustion. Both mixture profiles were studied for both high ( $\phi_{max} = 1.8$ ,  $\phi_{min} = 0.2$ ) and low ( $\phi_{max} = 1.3$ ,  $\phi_{min} = 0.7$ ) levels of stratification. The initial equivalence ratio profiles for the four cases are shown in Figure 5.19.

The pressure traces for the rich-lean and lean-rich profiles are presented in Figure 5.20. The centrally rich simulations had both a greater peak pressure value and

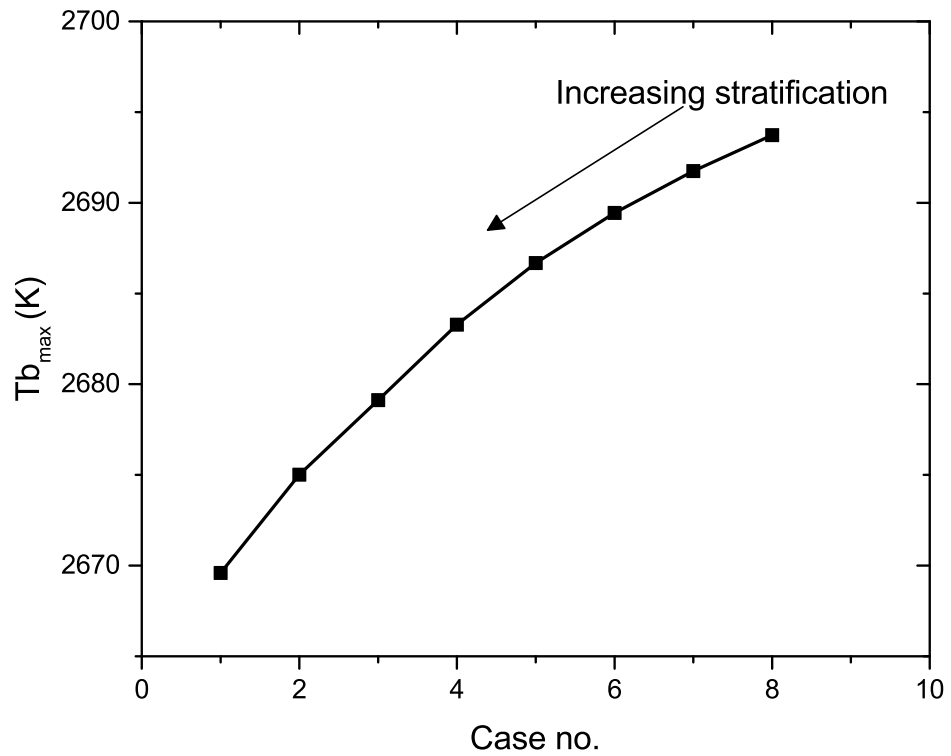


Figure 5.15: Maximum burned gas temperature for increasing stratification levels at 1500 rpm.

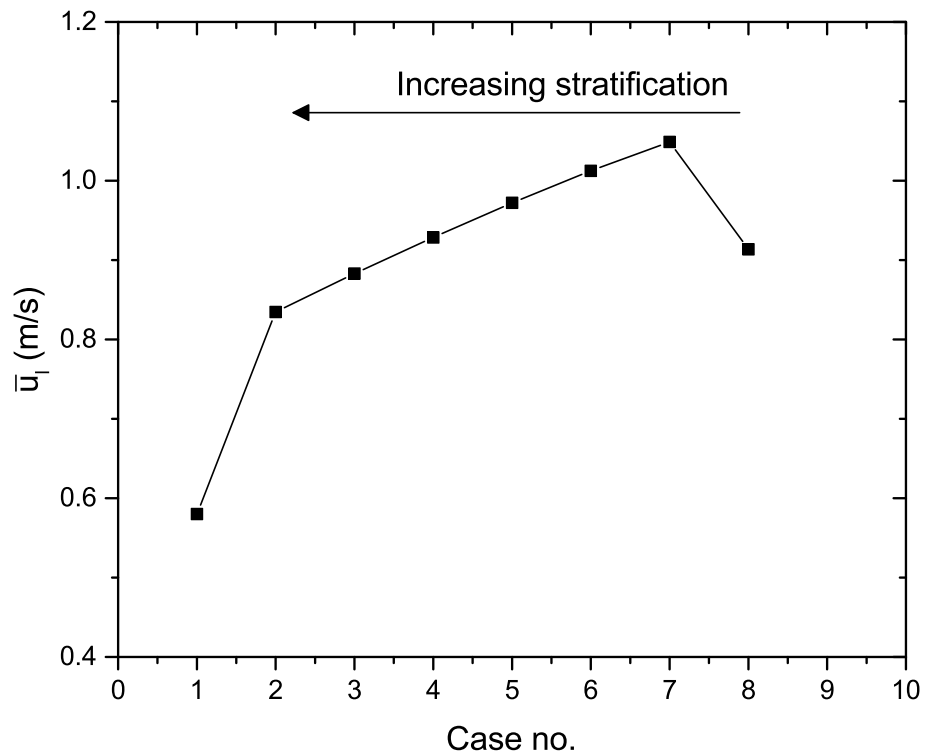


Figure 5.16: Mean laminar burning velocity for increasing stratification at 1500 rpm.

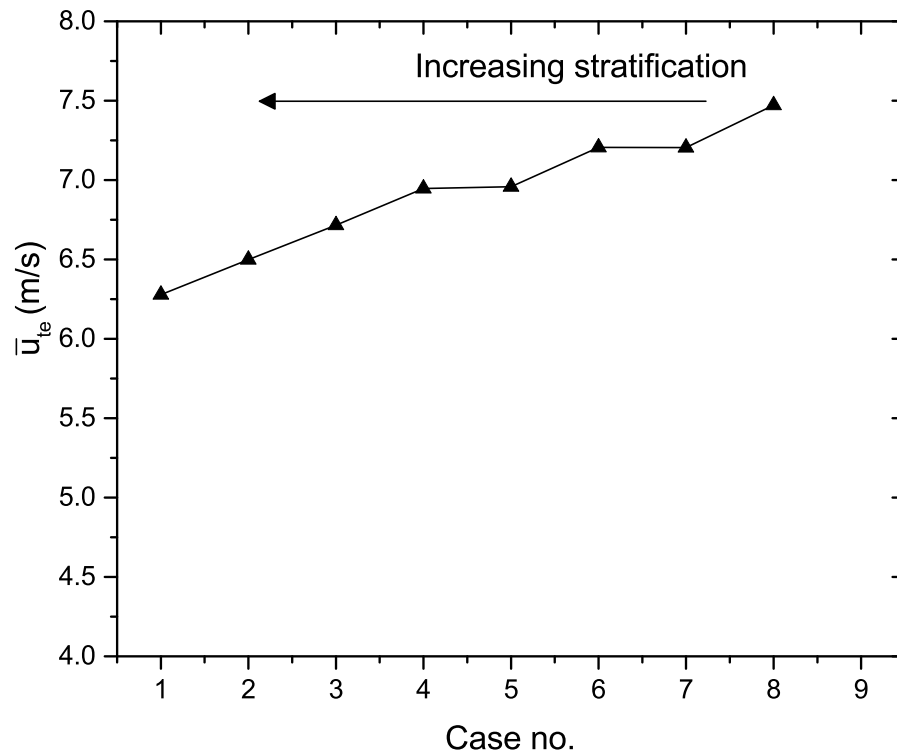


Figure 5.17: Mean turbulent entrainment velocity for increasing stratification at 1500 rpm.

an earlier occurrence of peak pressure when compared to the centrally lean case, however the difference was far more distinguishable for the higher level of stratification.

The rate of change of pressure with respect to time for the four cases studied are plotted in Figure 5.21. This plot was included in the analysis as Fujimoto et al. [1995] looked at centrally rich and centrally lean stratification profiles in a constant volume combustion chamber. One of the parameters analysed in the study by Fujimoto et al. [1995] was the rate of change of pressure. The simulations from the current study could therefore be compared to the experimental results. The particular focus was to see if the model captured any qualitative trends found from the experimental data, thus increasing the validity of the work presented here. The the rate of change of pressure from the study by Fujimoto et al. [1995] is included for direct comparison and is presented in Figure 5.22.

For the high stratification simulations the peak rate of change in pressure is significantly greater and occurs much earlier for the rich-lean case. These findings qualitatively follow the trend found experimentally (see Figure 5.22). Quantitatively they cannot be compared for several reasons. Firstly the method of determination is different. The SI case will experience a much greater rise in pressure due the

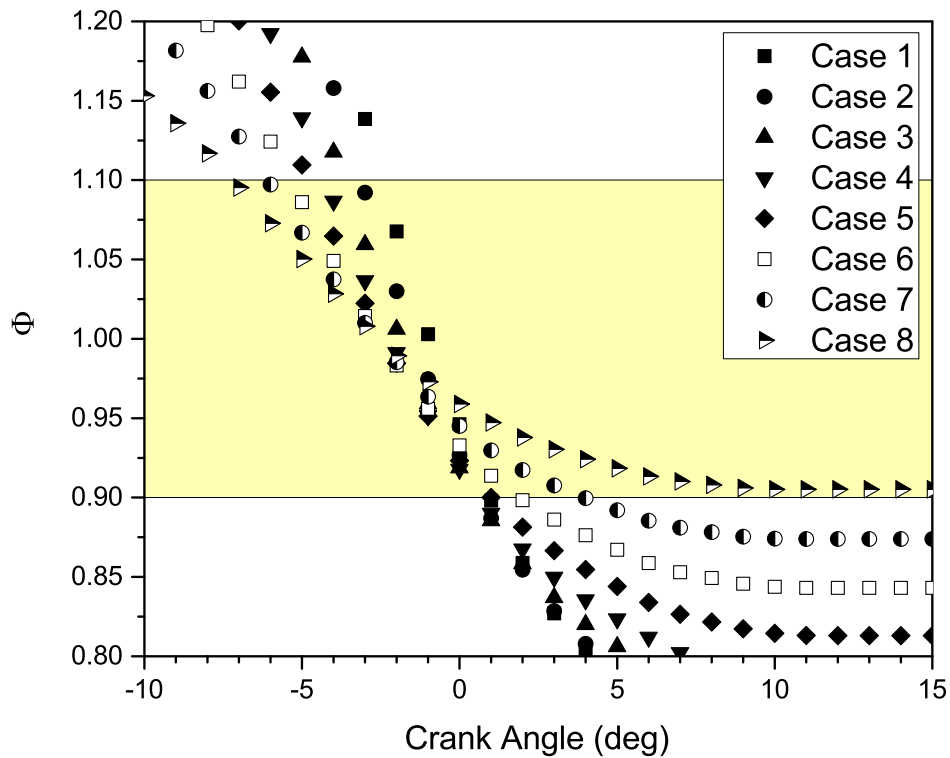


Figure 5.18: Crank resolved equivalence ratios for cases 1-8 with optimal equivalence ratios residing in the highlighted section.

compression effect of the moving piston. Secondly the fuel variants are different with the experiment using propane as opposed to the gasoline fuel modelled in this study. Finally the exact equivalence ratio profile for the experimental result is unknown. The low stratification cases also follow the qualitative trend, however the difference between rich-lean and lean-rich is greatly reduced. This is attributed to the relative change in equivalence ratio being considerably smaller for the weakly stratified case. In addition to the small change in  $\phi$ , the effect of turbulent mixing and burned gas expansion will quickly alter the mixture distribution with the in-cylinder charge becoming a similar equivalence ratio for both cases.

Fujimoto et al. [1995] also found that the centrally rich case had a greater amount of mass burned than the centrally lean case. The mass fraction burned for the simulated case was therefore investigated and is presented in Figure 5.23. The difference in mass burned is greatest for the highly stratified case, with the rich-lean simulation burning more mass than the lean-rich case. Again the case of low stratification follows the same trend where the difference is greatly reduced. The cause of this will also be due to the relatively small difference in equivalence ratio and the temporal changes to the fuel-air distribution.

The qualitative trend found in the literature for rich-lean and lean-rich fuel

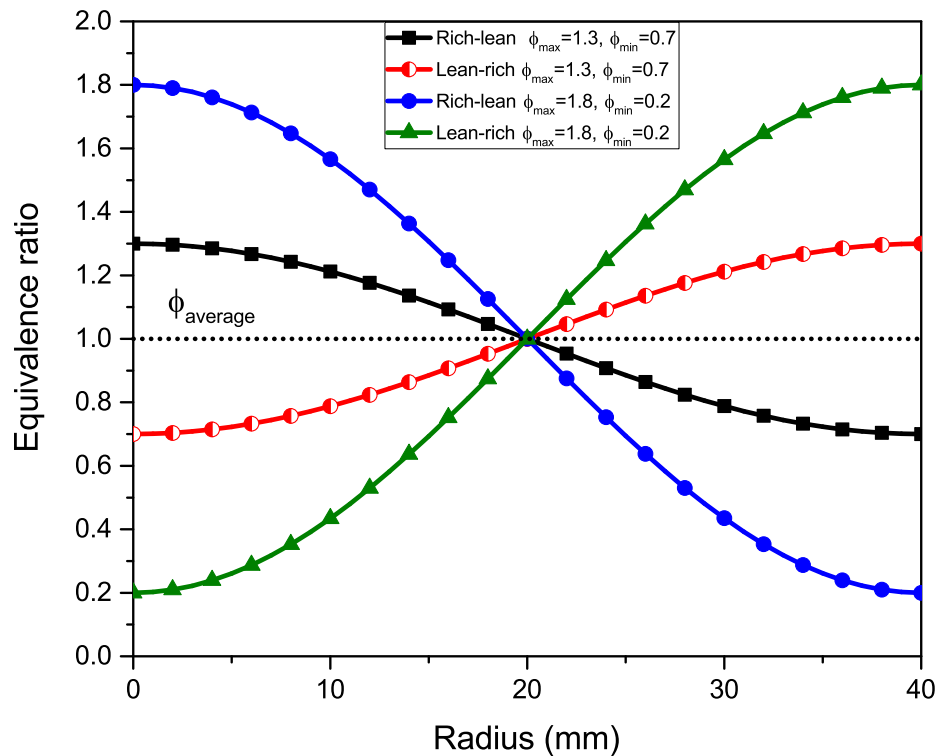


Figure 5.19: Two equivalence ratio profiles with same minima and maxima for rich-lean and lean-rich stratification profiles.

distributions is replicated by the stratified fuel model developed in this study, thus providing further evidence of the validity of the model.

## 5.8 Chapter Summary

This chapter describes the implementation of a stratified fuel mode model into a pre-existing quasi-dimensional thermodynamic predictive simulation code. The stratified fuel model included a radially varying fuel/air equivalence ratio based on spatial variations found within the literature, a turbulent mixing model and a model to capture the effect of burned gas expansion. The turbulent mixing model and burned gas expansion were incorporated to capture the temporal variation of the initial equivalence ratio profile. The burned gas expansion captures the effect of unburned but rich mixture propagating with flame as it expands. The turbulent mixing model looks to reduce the distribution to an equilibrium homogeneous value over time using a turbulent diffusivity value in the one-dimensional diffusion equation. It is well documented that over time the in-cylinder charge for a GDI engine will mix and become homogeneous for an early fuel injection strategy. While the charge may not become homogeneous for the late injection timing utilised in the stratified op-

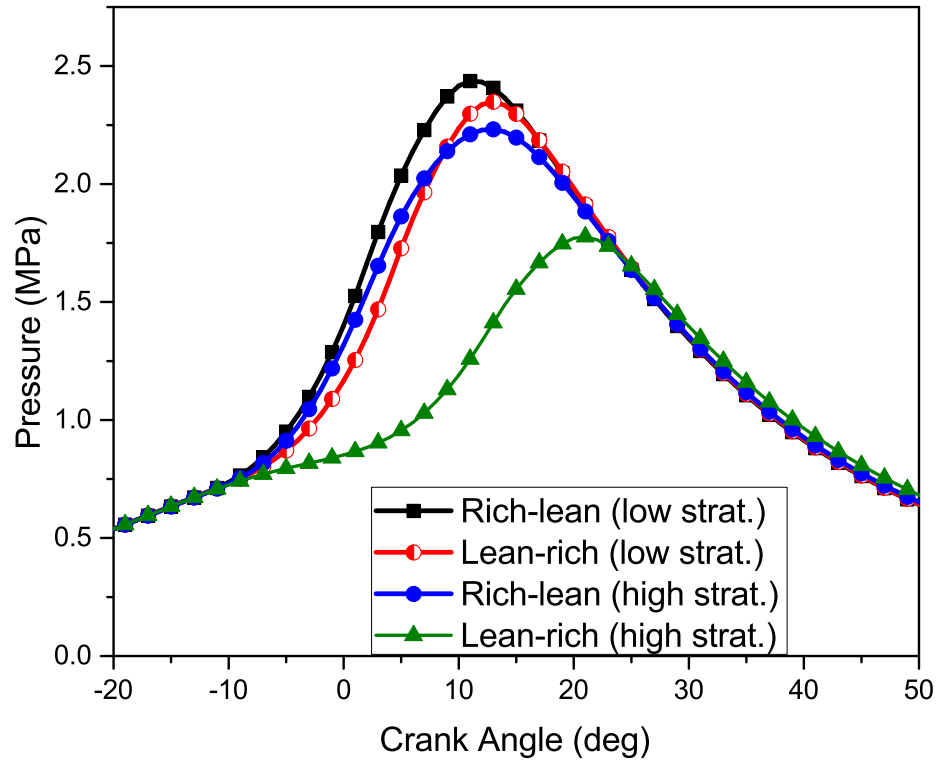


Figure 5.20: Crank resolved pressure trace for rich-lean and lean-rich stratification profiles at high and low levels of stratification.

erating mode, the effect of mixing has been found to be important in replicating experimental trends.

The stratified fuel model was validated against experimental data for both the in-cylinder pressure trace and rate of heat release. For both the in-cylinder pressure and heat release, the model fell within experimental bounds representing a fast combustion cycle. The effect of turbulent mixing was also investigated. The trend between the stratified and homogeneous simulations matched closest to the experimental data when the mixing model was included. The parameters  $\Delta P_{max}$  and  $\Delta P_{\theta}$  were the metrics used in this analysis. The simulations where mixing was not used for the stratified case showed the opposite trend to the experimental data.

The effect of the level of stratification on various combustion parameters were investigated under the same running conditions. The simulations found that increasing the stratification resulted in a decrease in both  $P_{max}$  and  $P_{\theta}$ . It was also found that increasing the stratification reduced the maximum burned gas temperature, with one practical application being a possible reduction in NOx emissions. However increased stratification led to a reduction in both the rate and absolute mass fraction burned. Less mass burned would lead to an increase in HC emissions. The reduction in mass burned with increasing stratification is in agreement with the

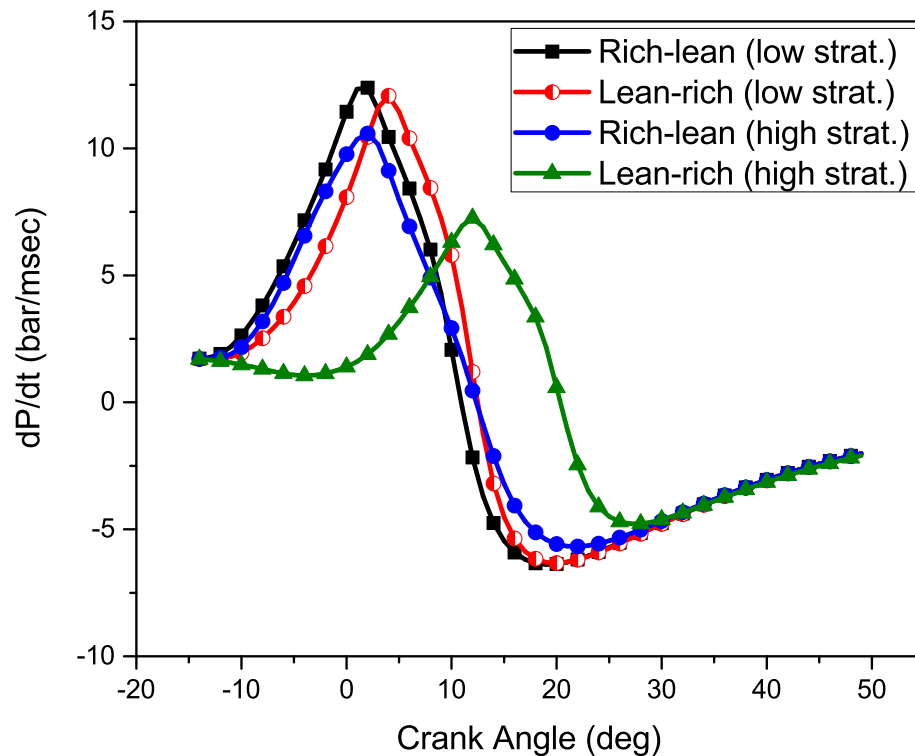


Figure 5.21: Rate of change of pressure w.r.t crank angle for rich-lean and lean-rich stratification profiles at high and low levels of stratification.

simulations by Robeck and Ellzey [1998]. The mean laminar and mean entrainment burning velocities also decreased with an increase in stratification.

A rich-lean stratification profile, typical of SI engine combustion was compared to a lean-rich profile for both high and low levels of stratification. The results of the simulations were compared to experimental data from Fujimoto et al. [1995] where a centre-rich and centre-lean equivalence ratio profile was investigated in a constant volume combustion vessel. The simulations found that for the highly stratified case, the rate of change of pressure was much greater and occurred considerably earlier for the rich-lean case. The total mass burned was also greater for the rich-lean case when compared to the lean-rich case at high levels of stratification. These qualitative trends are in agreement with the experimental results found in Fujimoto et al. [1995] and thus provide further evidence of the validity of the model. The low stratification simulations agreed with the high stratification findings, however the difference between the peak rate of pressure and mass burned was greatly reduced for the rich-lean and lean-rich cases. This is unsurprising as the relative change in equivalence ratio is considerably smaller for the weakly stratified case. In addition to this the nature of turbulent mixing and burned gas expansion will alter the equivalence ratio to a similar value for both the centre rich and centre lean cases.

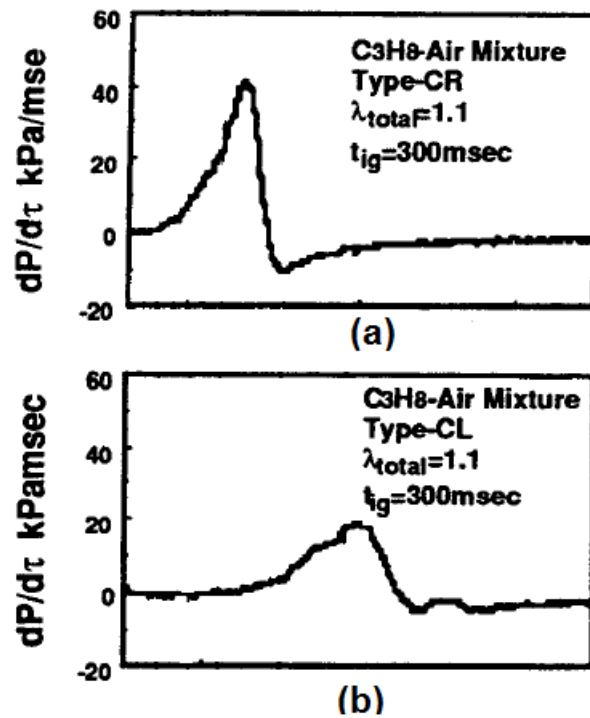


Figure 5.22: Rate of change of pressure w.r.t time for (a) a centrally rich stratification pattern and (b) a centrally lean stratification pattern. Taken from Fujimoto et al. [1995]

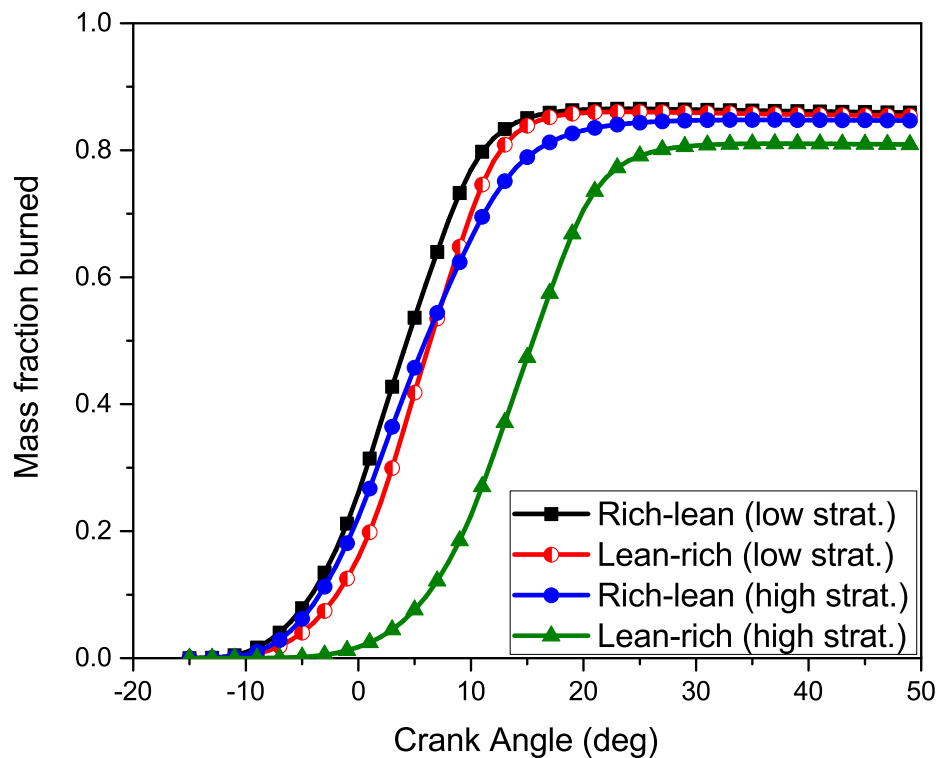


Figure 5.23: Crank resolved mass fraction burned for rich-lean and lean-rich stratification profiles at high and low levels of stratification.

# Chapter 6

## Conclusions and Recommendations

---

### 6.1 Introduction

The aim of the reported work was to update a quasi-dimensional thermodynamic combustion model to cope with recent trends in engine development strategies, dictated by the automotive industry, to meet ever more stringent environmental legislation. The two strategies used as a focal point for this study were: (i) a stratified fuel operation mode, where the equivalence ratio of the fuel-air mixtures varies spatially at the time of ignition and (ii) the introduction of cooled exhaust gas into the cylinder.

The quasi-dimensional predictive combustion model used throughout this work is identified as LUSIE (Leeds University Spark Ignition Engine). The routines within LUSIE can be easily incorporated into commercially available codes to enable full engine simulations. The predictive simulations were validated against data taken from a Jaguar Land Rover Single Cylinder Research Engine. The engine utilised a gasoline direct injection fuelling mechanism and a low pressure EGR loop. The reverse thermodynamic analysis of experimental engine data was carried out using the LUSIEDA (Leeds University Spark Ignition Engine Data Analysis) code.

Conclusions from the present study are described in this chapter. Recommendations for future research or further improvement to the work developed in this study are also presented.

## 6.2 Summary of EGR modelling conclusions

Presented in the current section are conclusions from the investigation into EGR correction factors derived from engine data (current work) and other methods (literature). The ability of these models to predict firing cycle pressure traces and mass fraction burned profiles were then analysed.

- A new method to determine correction factors for EGR from engine pressure trace data by using a reverse thermodynamic model is explored. Using this approach, a new correlation for the effects of exhaust gas diluent on the laminar burning velocity of a EURO VI specification gasoline is derived and compared against existing models. The reduction in laminar burning velocity due to EGR was found to be less than the values stated in the literature between the range of 5-25% EGR. At 5% EGR the value determined from engine data was found to be much closer to the literature values than at the greater levels of EGR, where the difference was much more pronounced. The models from the literature analysed here all utilise synthetic EGR, while the present study uses the full range of exhaust gas species. Using synthetic EGR has been found by Manna et al. [2017] to produce a greater reduction in the laminar burning velocity than real EGR. This is a conclusion that is supported by this study.
- The EGR correction factor derived using engine data requires a user defined constant,  $C_{ut}$ , to be constrained. This was manageable by comparing the Zimont-Lipatnikov turbulent burning velocity to the U/K correlation. While both models were developed years apart, analysis showed the models are indeed very similar. Direct comparison of the models allows  $C_{ut}$  to be constrained. Due to the dependency of the correction factor on  $C_{ut}$ , a sensitivity analysis was carried out. The constant was varied by  $\pm 10\%$ , with the maximum change at any point being 1.5%.
- The newly derived engine data correlation and models from the literature were then implemented into a predictive combustion code to compare their predictive modelling capabilities. The models were tested at three engine test points: 1500 rpm 0.36 MPa GMEP, 1500 rpm 0.79 MPa GMEP and 2000 rpm 0.98 MPa GMEP. The best fit was quantified using a RMS error comparing the simulated models to the mean cycle. Across all speed/load test points the model from the present study provided the best fit to the experimental mean for both pressure trace data and mass fraction burned profile.
- While no tuning of constants that affect burning velocity ( $C_{ut}, C_{\tau_b}$ ) were tuned

beyond the 0% EGR case, the time it takes for the spark kernel to form a specified diameter was tuned. It was found that as the level of EGR increases the time taken to form a spark kernel of a given size increased. As the early stages of the flame can be thought of as laminar-like it is not surprising that increasing EGR, and therefore decreasing laminar burning velocity, means it takes longer to reach a given kernel diameter. These findings agree with those by Robertson et al. [2018] who found a decrease in flame growth multiplier (analogous to inverse of kernel delay time) for increasing EGR fraction.

- The correlation derived by Metghalchi and Keck [1982] is the best performing model from the literature closely followed by the Bhattacharya et al. [2015] model. However, the derivation of the Metghalchi and Keck [1982] correlation is highly fortuitous. The pressure trace data analysed was found to be susceptible to cellularity, thus increasing the laminar burning velocity and the values of EGR correlation. However the exhaust gas composition is simulated and only comprises of the species  $\text{CO}_2$  and  $\text{N}_2$ . These species have been found to be more reductive than realistic exhaust gas composition, leading to a greater correction factor to the laminar burning velocity due to the effect of EGR. The increase in EGR factor due to cellularity and reduction due to simulated EGR appear to cancel out thus explaining why the correlation provided the best predictions from the literature models.

### 6.3 Summary of stratified fuel model conclusions

Presented in the current section are conclusions from the development of a quasi-dimensional stratified fuel model, and the investigations into the effect of the equivalence ratio distribution on combustion parameters.

- A quasi-dimensional stratified charge model that incorporated a radially varying equivalence ratio, the effect of burned gas expansion and turbulent mixing on the fuel distribution was validated against experimental data for both in-cylinder pressure and percentage heat released. The simulations fell within the bounds of experimental data representing a fast combustion cycle.
- The trend between the stratified and homogeneous simulations matched closest to the experimental data when the mixing model was included. The parameters compared were  $\Delta P_{max}$  and  $\Delta P_\theta$ . The simulations where mixing was not used for the stratified case actually showed the opposite trend to the experimental data.

- Combustion parameters are sensitive to the level of stratification. The increase in stratification leads to a reduction in pressure, maximum burned gas temperature, rate of mass burned, total mass burned, laminar burning velocity and turbulent entrainment velocity. While the increase in unburned mass for highly stratified cases will lead to greater unburned HC emissions, the reduction in burned gas temperature could offer a benefit in NOx reduction. This is assuming that the temperature is still great enough to allow the three-way catalyst to operate effectively.
- Initial distribution change allowed for better modelling of mean cycle for the stratified case. The stratified model validation was carried out under an arbitrary stratification profile, which was weakly constrained. The simulation predicted a fast combustion cycle. Increasing the level of stratification to  $\phi_{max} = 1.8$  and  $\phi_{min} = 0.2$  produced a pressure trace much closer to the mean cycle.
- The stratified fuel model replicates the qualitative trends found experimentally for centrally rich and centrally lean stratification profiles. The stratification profile with a centrally rich and radially decreasing equivalence ratio produces the highest in-cylinder maximum pressures when compared to a centrally lean with radially increasing equivalence ratio. This was true for both strongly and weakly stratified cases. The centrally rich case also has a greater rate of change of pressure (dP/dt) and burns more of the available fuel.
- The weaker the level of stratification the less the spatial distribution effects the combustion event. The rich-lean and lean-rich profile for the weakly stratified case show much smaller differences when comparing mass burned, pressure and rate of change of pressure to the highly stratified case.

## 6.4 Recommendations for future work

Throughout the reported work a number of areas for future investigation have been identified. These areas were either beyond the scope of the work or would have required additional experimental testing that was not feasible owing to time, equipment or resource restrictions. Suggestions for future research are as follows:

- Experimental investigation on how pressure, temperature and exhaust gas diluent effect stretch rate Markstein number,  $Ma_{sr}$ . This would allow for a modelling investigation to be carried out for the newly suggested U/K turbulent burning velocity correlation.

- Look to implement a chemical kinetics mechanism within the predictive LUSIE code to improve laminar burning velocity modelling. Furthermore compare this to experimental correlations already included in the code.
- While the effect of turbulent mixing was found to be necessary to match qualitative differences in the model validation it would be worth validating the mixing model against CFD or experimental data. It would be worth investigating how the mixing model changes the profile based on whether the in-cylinder bulk motion is swirl or tumble.
- The EGR correction factor was derived under stoichiometric ( $\phi = 1.0$ ) conditions. Engines operate under a number of different equivalence ratios which changes both the baseline laminar burning velocity (EGR=0) and the composition of exhaust gas. For an increased range of model applicability the work should be extended to account for different equivalence ratios.
- Investigation into spark kernel behaviour to eliminate early flame formation tuning. The investigation into spark kernel behaviour may enable a more realistic ignition model, improving model predictability and thus requiring less tuning by the user to match experimental data.

# References

---

- R.G. Abdel-Gayed, K.J. Al-Khishali, and D. Bradley. Turbulent burning velocities and flame straining in explosions. *Proceedings of the Royal Society of London A: Mathematical, Physical and Engineering Sciences*, 391: 393–414, 1984.
- R.G. Abdel-Gayed, D. Bradley, and M. Lawes. Turbulent burning velocities: a general correlation in terms of straining rates. *Proceedings of the Royal Society of London A: Mathematical, Physical and Engineering Sciences*, 414: 389–413, 1987.
- E. Abdi Aghdam, A. A. Burluka, T. Hattrell, K. Liu, C. G. W. Sheppard, J. Neumeister, and N. Crundwell. Study of cyclic variation in an SI engine using quasi-dimensional combustion model. SAE Technical Paper 2007-01-0939, 2007.
- S.K. Addepalli, O.P. Saw, and J.M. Mallikarjuna. Effect of mixture distribution on combustion and emission characteristics in a GDI engine - a CFD analysis. SAE Technical Paper 2017-24-0036, 2017.
- C.J. Adkins. *An introduction to thermal physics*. Cambridge University Press, Cambridge, England, 1987.
- E. Abdi Aghdam. *Improvement and validation of a thermodynamic S.I. engine simulation code*. PhD Thesis, School of Mechanical Engineering, University of Leeds, 2003.
- B. Ahmadi-Befrui, W. Brandstatter, and H. Kratochwill. Calculation of

- inhomogeneous-charge combustion in a swirl-assisted lean-burn engine, SAE Technical Paper 910266, 1991.
- F. Al-Mamar. *Combustion in a dual chamber spark ignition engine*. PhD Thesis, School of Mechanical Engineering, University of Leeds, 1983.
- A.S. Al-Shahrany, D. Bradley, M. Lawes, and R. Woolley. Measurement of unstable burning velocities of iso-octane-air mixtures at high pressure and the derivation of laminar burning velocities. *Proceedings of the Combustion Institute*, 30 (1): 225–232, 2005.
- P.G. Aleiferis, A.M.K.P. Taylor, K. Ishii, and Y. Urata. The relative effects of fuel concentration, residual-gas fraction, gas motion, spark energy and heat losses to the electrodes on flame-kernel development in a lean-burn spark ignition engine. *Proceedings of the Institution of Mechanical Engineers, Part D: Journal of Automobile Engineering*, 218 (4): 411–425, 2004.
- T. Alger, J. Gingrich, C. Roberts, and B. Mangold. Cooled exhaust-gas recirculation for fuel economy and emissions improvement in gasoline engines. *International Journal of Engine Research*, 12 (3): 252–264, 2011.
- T. Alger and S. Wooldridge. Measurement and analysis of the residual gas fraction in an SI engine with variable cam timing. SAE Technical Paper 2004-01-1356, 2004.
- M. Aliramezani, I. Chitsaz, and A.A. Mozafari. Thermodynamic modeling of partially stratified charge engine characteristics for hydrogen-methane blends at ultra-lean conditions. *International Journal of Hydrogen Energy*, 38 (25): 10640–10647, 2013.
- W.J.D. Annand. Heat transfer in the cylinders of reciprocating internal combustion engines. *Proceedings of the Institution of Mechanical Engineers*, 177 (1): 973–996, 1963.

- T. Ashizawa, K. Saitoh, Y. Tamura, and T. Sakai. Development of a new in-line 4-cylinder direct-injection gasoline engine. SAE Technical Paper 988265, 1998.
- S. O. Bade Shrestha and G. A. Karim. Considering the effects of cyclic variations when modeling the performance of a spark ignition engine. SAE Technical Paper 2001-01-3600, 2001.
- J.K. Ball, R.R. Raine, and C.R. Stone. Combustion analysis and cycle-by-cycle variations in spark ignition engine combustion part 2: A new parameter for completeness of combustion and its use in modelling cycle-by-cycle variations in combustion. *Proceedings of the Institution of Mechanical Engineers, Part D: Journal of Automobile Engineering*, 212 (6): 507–523, 1998.
- M. Baloo, B.M. Dariani, M. Akhlaghi, and M.A. Mirsalim. Effects of pressure and temperature on laminar burning velocity and flame instability of iso-octane/methane fuel blend. *Fuel*, 170: 235–244, 2016.
- S. Balusamy, A. Cessou, and B. Lecordier. Laminar propagation of lean premixed flames ignited in stratified mixture. *Combustion and Flame*, 161 (2): 427–437, 2014.
- M. Berckmüller, N.P. Tait, and D.A. Greenhalgh. The time history of the mixture formation process in a lean burn stratified-charge engine. SAE Technical Paper 961929, 1996.
- A. Bhattacharya, D.K. Banerjee, D. Mamaikin, A. Datta, and M. Wensing. Effects of exhaust gas dilution on the laminar burning velocity of real-world gasoline fuel flame in air. *Energy & Fuels*, 29 (10): 6768–6779, 2015.
- R. W. Bilger, S. B. Pope, K. N. C. Bray, and J. F. Driscoll. Paradigms in turbulent combustion research. *Proceedings of the Combustion Institute*, 30 (1): 21–42, 2005.
- N.C. Blizard and J.C. Keck. Experimental and theoretical investigation of turbulent

- burning model for internal combustion engines. SAE Technical Paper 740191, 1974.
- N. Bock, J. Jeon, D. Kittelson, and W.F. Northrop. Solid particle number and mass emissions from lean and stoichiometric gasoline direct injection engine operation. SAE Technical Paper 2018-01-0359, 2018.
- R. Borghi and M. Destriau. *Combustion and flames: chemical and physical principles*. Editions Technip, Paris, 1st Edition, 1998.
- F. Bozza, V. De Bellis, F. Berni, A. D’Adamo and L. Maresca. Refinement of a 0D Turbulence Model to Predict Tumble and Turbulent Intensity in SI Engines. Part I: 3D Analyses. SAE Technical Paper 2018-01-0850, 2018.
- F. Bozza, L. Teodosio, V. De Bellis, S. Fontanesi, and A. Iorio. Refinement of a 0D Turbulence Model to Predict Tumble and Turbulent Intensity in SI Engines. Part II: Model Concept, Validation and Discussion. SAE Technical Paper 2018-01-0856, 2018.
- D. Bradley, A.K.C. Lau, and M. Lawes. Flame stretch rate as a determinant of turbulent burning velocity. *Philosophical Transactions of the Royal Society of London A: Mathematical, Physical and Engineering Sciences*, 338 (1650): 359–387, 1992.
- D. Bradley, R.A. Hicks, M. Lawes, C.G.W. Sheppard, and R. Woolley. The measurement of laminar burning velocities and markstein numbers for iso-octane-air and iso-octane-n-heptane-air mixtures at elevated temperatures and pressures in an explosion bomb. *Combustion and Flame*, 115 (1): 126–144, 1998.
- D. Bradley, M. Lawes, and M. S. Mansour. Explosion bomb measurements of ethanol-air laminar gaseous flame characteristics at pressures up to 1.4 MPa. *Combustion and Flame*, 156 (7): 1462–1470, 2009.
- D. Bradley, M. Lawes, K. Liu, and M. S. Mansour. Measurements and correlations

- of turbulent burning velocities over wide ranges of fuels and elevated pressures. *Proceedings of the Combustion Institute*, 34 (1): 1519–1526, 2013.
- D. Bradley and C.M. Harper. The development of instabilities in laminar explosion flames. *Combustion and Flame*, 99 (3): 562–572, 1994.
- D. Bradley, P.H. Gaskell, and X.J. Gu. Burning velocities, Markstein lengths, and flame quenching for spherical methane-air flames: A computational study. *Combustion and Flame*, 104 (1): 176–198, 1996.
- D. Bradley, M. Lawes, and M.S. Mansour. The problems of the turbulent burning velocity. *Flow, Turbulence and Combustion*, 87 (2): 191–204, 2011.
- P. Bradshaw. *An introduction to turbulence and its measurement*. Pergamon Press, Oxford, 1971.
- A.A. Burluka, A.M.T.A. El-Dein Hussin, Z.Y. Ling, and C.G.W. Sheppard. Effects of large-scale turbulence on cyclic variability in spark-ignition engine. *Experimental Thermal and Fluid Science*, 43: 13–22, 2012.
- A.A. Burluka, R.G. Gaughan, J.F. Griffiths, C. Mandilas, C.G.W. Sheppard, and R. Woolley. Turbulent burning rates of gasoline components, part 2 - effect of carbon number. *Fuel*, 167: 357–365, 2016.
- A. Cairns, H. Blaxill, and G. Irlam. Exhaust gas recirculation for improved part and full load fuel economy in a turbocharged gasoline engine. SAE Technical Paper 2006-01-0047, 2006.
- A. Cairns, N. Fraser, and H. Blaxill. Pre versus post compressor supply of cooled EGR for full load fuel economy in turbocharged gasoline engines. SAE Technical Paper 2008-01-0425, 2008.
- H. Chen, H. Zhuang, D.L. Reuss, and V. Sick. Influence of early and late fuel injection on air flow structure and kinetic energy in an optical SIDI engine. SAE Technical Paper 2018-01-0205, 2018.

- H. Cho, K. Lee, J. Lee, J. Yoo, and K. Min. Measurements and modeling of residual gas fraction in SI engines. SAE Technical Paper 2001-01-1910, 2001.
- E. Conte and K. Boulouchos. A quasi-dimensional model for estimating the influence of hydrogen-rich gas addition on turbulent flame speed and flame front propagation in IC-SI engines. SAE Technical Paper 2005-01-0232, 2005.
- G.T. Conway. *Cyclic variability of flame propagation and autoignition in supercharged and naturally aspirated SI engines*. PhD Thesis, School of Mechanical Engineering, University of Leeds, 2013.
- H.J. Curran, P. Gaffuri, W.J. Pitz, and C.K. Westbrook. A comprehensive modeling study of n-heptane oxidation. *Combustion and Flame*, 114 (1): 149–177, 1998.
- H.J. Curran, P. Gaffuri, W.J. Pitz, and C.K. Westbrook. A comprehensive modeling study of iso-octane oxidation. *Combustion and Flame*, 129 (3): 253–280, 2002.
- W. Dai, G.C. Davis, M.J. Hall, and R.D. Matthews. Diluents and lean mixture combustion modeling for SI engines with a quasi-dimensional model. SAE Technical Paper 952382, 1995.
- W. Dai, N. Trigui, and Y. Lu. Modeling of cyclic variations in spark-ignition engines. SAE Technical Paper 2000-01-2036, 2000.
- A. Desoky. *An experiental and theoretical study of the combustion process in a divided chamber spark ignition engine*. PhD Thesis, School of Mechanical Engineering, University of Leeds, 1981.
- M.C. Drake and D.C. Haworth. Advanced gasoline engine development using optical diagnostics and numerical modeling. *Proceedings of the Combustion Institute*, 31 (1): 99–124, 2007.
- J.F. Driscoll. Turbulent premixed combustion: Flamelet structure and its effect on turbulent burning velocities. *Progress in Energy and Combustion Science*, 34 (1): 91–134, 2008.

- J.M. Duclos, D. Veynante, and T. Poinso. A comparison of flamelet models for premixed turbulent combustion. *Combustion and Flame*, 95 (1): 101–117, 1993.
- J.M. Duclos and M. Zolver. 3D modeling of intake, injection and combustion in a DI-SI engine under homogeneous and stratified operating conditions. In *Fourth Internatiuonal Symposium COMODIA*, 98, 335–340, 1998.
- M.H. Edson. Digital Calculations of Engine Cycle - *The Influence of Compression Ratio and Dissociation on Ideal Otto Cycle Engine Thermal Efficiency*, Chapter 4, Pergamon, Oxford, 1964.
- T.D. Fansler and M.C. Drake. Flow and combustion in reciprocating engines *Flow, mixture preparation and combustion in direct-injection two-stroke gasoline engines*, Springer, 2008.
- T.D. Fansler, D.L. Reuss, V. Sick, and R.N. Dahms. Combustion instability in spray-guided stratified-charge engines: A review. *International Journal of Engine Research*, 16 (3): 260–305, 2015.
- C.R. Ferguson and A. Kirkpatrick. *Internal combustion engines: applied thermo-sciences*, Wiley, Chichester, New York, 2nd edition, 2001.
- C.E.A. Finney, B.C. Kaul, C.S. Daw, R.M. Wagner, K.D. Edwards, and J.B. Green. A review of deterministic effects in cyclic variability of internal combustion engines. *International Journal of Engine Research*, 16 (3): 366–378, 2015.
- Department for Transport. Vehicle licensing statistics: October to December 2015 data tables, 2016.
- A. Frassoldati, R. Grana, T. Faravelli, E. Ranzi, P. Osswald, and K. Kohse-Höinghaus. Detailed kinetic modeling of the combustion of the four butanol isomers in premixed low-pressure flames. *Combustion and Flame*, 159 (7): 2295–2311, 2012.

- J. Fu, B. Deng, Y. Wang, J. Yang, D. Zhang, Z. Xu, and J. Liu. Numerical study and correlation development on laminar burning velocities of n-butanol, iso-octane and their blends: Focusing on diluent and blend ratio effects. *Fuel*, 124: 102–112, 2014.
- M. Fujimoto, K. Nishida, H. Hiroyasu, and M. Tabata. Influence of mixture stratification pattern on combustion characteristics in a constant-volume combustion chamber. SAE Technical Paper 952412, 1995.
- B. Galmiche, F. Halter, and F. Foucher. Effects of high pressure, high temperature and dilution on laminar burning velocities and Markstein lengths of iso-octane/air mixtures. *Combustion and Flame*, 159 (11): 3286–3299, 2012.
- L. Gillespie, M. Lawes, C.G.W. Sheppard, and R. Woolley. Aspects of laminar and turbulent burning velocity relevant to SI engines. SAE Technical Paper 2000-01-0192, 2000.
- J. F. Griffiths, J. A. Barnard, and J. N. Bradley. *Flame and combustion*, Blackie, London, 3rd edition, 1995.
- X.J. Gu, M.Z. Haq, M. Lawes, and R. Woolley. Laminar burning velocity and Markstein lengths of methane-air mixtures. *Combustion and Flame*, 121 (1): 41–58, 2000.
- R. Gukelberger, J. Gingrich, T. Alger, S. Almaraz, and B. Denton. LPL EGR and D-EGR® engine concept comparison part 1: Part load operation. *SAE International Journal of Engines*, 8 (2): 570–582, 2015.
- T. Hattrell. GGEOM technical manual. *University of Leeds*, 2009.
- T. Hattrell. *A computational and experimental study of spark ignition engine combustion*. PhD Thesis, School of Mechanical Engineering, University of Leeds, 2007.
- John B. Heywood. *Internal combustion engine fundamentals*. McGraw-Hill, 1988.

- P.G. Hill and D. Zhang. The effects of swirl and tumble on combustion in spark-ignition engines. *Progress in Energy and Combustion Science*, 20 (5): 373–429, 1994.
- J.O. Hinze. *Turbulence: An Introduction to its Mechanism and Theory*, McGraw-Hill, New York, 1959.
- K. Horie, Y. Kohda, K. Ogawa, and H. Goto. Development of a high fuel economy and low emission four-valve direct injection engine with a center-injection system. SAE Technical Paper 2004-01-2941, 2004.
- C. Huang, E. Yasari, L.C.R. Johansen, S. Hemdal, and A.N. Lipatnikov. Application of flame speed closure model to rans simulations of stratified turbulent combustion in a gasoline direct-injection spark-ignition engine. *Combustion Science and Technology*, 188 (1): 98–131, 2016.
- C. Huang, A. Lipatnikov, L.C.R. Johansen, and S. Hemdal. A study of two basic issues relevant to RANS simulations of stratified turbulent combustion in a spray-guided direct-injection spark-ignition engine. SAE 2014-01-2572, 2014.
- C. Huang, E. Yasari, and A. Lipatnikov. A numerical study on stratified turbulent combustion in a direct-injection spark-ignition gasoline engine using an open-source code. SAE 2014-01-1126, 2014.
- P. Huegel, H. Kubach, T. Koch, and A. Velji. Investigations on the heat transfer in a single cylinder research SI engine with gasoline direct injection. *SAE International Journal of Engines*, 8 (2): 557–569, 2015.
- A Hussin. *New and Renewable Energy: Renewable Fuels in Internal Combustion Engines*. PhD Thesis, School of Mechanical Engineering, University of Leeds, 2012.
- J. Hynes. *A Computational and Experimental Study of Spark Ignition Combustion*. PhD Thesis, School of Mechanical Engineering, University of Leeds, 1986.

- Y. Iwamoto, K. Noma, O. Nakayama, T. Yamauchi, and H. Ando. Development of gasoline direct injection engine. SAE Technical Paper 970541, 1997.
- S. Jarvis, T. Justham, A. Clarke, C.P. Garner, G.K. Hargrave, and D. Richardson. Motored SI IC engine in-cylinder flow field measurement using time resolved digital PIV for characterisation of cyclic variation. SAE Technical Paper 2006-01-1044, 2006.
- S. Jerzembeck, N. Peters, P. Pepiot-Desjardins, and H. Pitsch. Laminar burning velocities at high pressure for primary reference fuels and gasoline: Experimental and numerical investigation. *Combustion and Flame*, 156 (2): 292–301, 2009.
- T. Justham, S. Jarvis, C.P. Garner, G.K. Hargrave, A. Clarke, and D. Richardson. Single cylinder motored SI IC engine intake runner flow measurement using time resolved digital particle image velocimetry. SAE Technical Paper 2006-01-1043, 2006.
- G. Karl, R. Kemmler, M. Bargende, and J. Abthoff. Analysis of a direct injected gasoline engine. SAE Technical Paper 970624, 1997.
- J.C. Keck, J.B. Heywood, and G. Noske. Early flame development and burning rates in spark ignition engines and their cyclic variability. SAE Technical Paper 870164, 1987.
- Alan R. Kerstein. Pair-exchange model of turbulent premixed flame propagation. *Symposium (International) on Combustion*, 21 (1): 1281–1289, 1988.
- A.F. Khan. *Chemical kinetics modelling of combustion processes in SI engines*. PhD Thesis, School of Mechanical Engineering, University of Leeds, 2014.
- A.N. Kolmogorov. The local structure of turbulence in incompressible viscous fluid for very large reynolds numbers. *Proceedings: Mathematical and Physical Sciences*, 434 (1890): 9–13, 1991a.

- A.N. Kolmogorov. Dissipation of energy in the locally isotropic turbulence. *Proceedings: Mathematical and Physical Sciences*, 434 (1890): 15–17, 1991b.
- A. Kountouriotis. PhD Thesis (in preparation), School of Mechanical Engineering, Imperial College London, 2018.
- K. Kumano and S. Yamaoka. Analysis of knocking suppression effect of cooled EGR in turbo-charged gasoline engine. SAE Technical Paper 2014-01-1217, 2014.
- G. Larsson. *Turbulence related cyclic variation in combustion*. PhD Thesis, School of Mechanical Engineering, University of Leeds, 2009.
- G.A. Lavoie, J.B. Heywood, and J.C. Keck. Experimental and Theoretical Study of Nitric Oxide Formation in Internal Combustion Engines. *Combustion Science and Technology*, 1 (4): 313–326, 1970.
- C.K. Law. *Combustion physics*. Cambridge University Press, Cambridge, England, 2006.
- Z. Ling. *Flame propagation and autoignition in a high pressure optical engine*. PhD Thesis, School of Mechanical Engineering, University of Leeds, 2014.
- T.M. Liou and D.A. Santavicca. Cycle resolved turbulence measurements in a ported engine with and without swirl. SAE Technical Paper 830419, 1983.
- T.M. Liou, M. Hall, D.A. Santavicca, and F.V. Bracco. Laser doppler velocimetry measurements in valved and ported engines. SAE Technical Paper 840375, 1984.
- A.N. Lipatnikov and J. Chomiak. Turbulent flame speed and thickness: phenomenology, evaluation, and application in multi-dimensional simulations. *Progress in Energy and Combustion Science*, 28 (1): 1–74, 2002.
- A.N. Lipatnikov and J. Chomiak. Molecular transport effects on turbulent flame propagation and structure. *Progress in Energy and Combustion Science*, 31 (1): 1–73, 2005.

- A.N. Lipatnikov. Stratified turbulent flames: Recent advances in understanding the influence of mixture inhomogeneities on premixed combustion and modeling challenges. *Progress in Energy and Combustion Science*, 62: 87–132, 2017.
- A. Lipatnikov. *Fundamentals of Premixed Turbulent Combustion*, CRC Press, Boca Raton, Florida, 1st edition, 2012.
- A.N. Lipatnikov and J. Chomiak. A simple model of unsteady turbulent flame propagation. SAE Technical Paper 972993, 1997.
- A.N. Lipatnikov and J. Chomiak. Modeling of pressure and non-stationary effects in spark ignition engine combustion: A comparison of different approaches. SAE Technical Paper 2000-01-2034, 2000.
- K. Liu. LUSIE manual, School of Mechanical Engineering, University of Leeds, 2004.
- K. Liu, A.A. Burluka, and C.G.W. Sheppard. Turbulent flame and mass burning rate in a spark ignition engine. *Fuel*, 107: 202–208, 2013.
- J.L. Lumley. *Engines: an introduction*. Cambridge University Press, Cambridge, England, 1999.
- M.B. Luong, Z. Luo, T. Lu, S.H. Chung, and C.S. Yoo. Direct numerical simulations of the ignition of lean primary reference fuel/air mixtures with temperature inhomogeneities. *Combustion and Flame*, 160 (10): 2038–2047, 2013.
- O.A. Manna, M.S. Mansour, W.L. Roberts, and S.H. Chung. Influence of ethanol and exhaust gas recirculation on laminar burning behaviors of fuels for advanced combustion engines (FACE-C) gasoline and its surrogate. *Energy & Fuels*, 31 (12): 14104–14115, 2017.
- S.P. Marshall, S. Taylor, C.R. Stone, T.J. Davies, and R.F. Cracknell. Laminar burning velocity measurements of liquid fuels at elevated pressures and temperatures with combustion residuals. *Combustion and Flame*, 158 (10): 1920–1932, 2011.

- M. Metghalchi and J.C. Keck. Burning velocities of mixtures of air with methanol, isooctane, and indolene at high pressure and temperature. *Combustion and Flame*, 48: 191–210, 1982.
- R.J. Middleton, J.B. Martz, G.A. Lavoie, A. Babajimopoulos, and D.N. Assanis. A computational study and correlation of premixed isooctane air laminar reaction fronts diluted with EGR. *Combustion and Flame*, 159 (10): 3146–3157, 2012.
- H. Miyagawa, Y. Nomura, M. Koike, and T. Tomoda. CFD simulation of stratified combustion process in a direct injection spark ignition engine. *JSME International Journal Series B Fluids and Thermal Engineering*, 46 (2): 332–339, 2003.
- Y. Moriyoshi, H. Morikawa, T. Kamimoto, and T. Hayashi. Combustion enhancement of very lean premixture part in stratified charge conditions. SAE Technical Paper 962087, 1996.
- Y. Moriyoshi, H. Morikawa, and E. Komatsu. Analysis of turbulent combustion in simplified stratified charge conditions. *JSME International Journal Series B Fluids and Thermal Engineering*, 46 (1): 86–91, 2003.
- U.C. Müller, M. Bollig, and N. Peters. Approximations for burning velocities and Markstein numbers for lean hydrocarbon and methanol flames. *Combustion and Flame*, 108 (3): 349–356, 1997.
- R.D. Mumby. *Experimental Characterisation of Fuel Blends*. PhD Thesis, School of Mechanical Engineering, University of Leeds, 2016.
- G. Nivarti and S. Cant. Direct numerical simulation of the bending effect in turbulent premixed flames. *Proceedings of the Combustion Institute*, 36 (2): 1903–1910, 2017.
- T. Omura, K. Nakata, Y. Yoshihara, and D. Takahashi. Research on the measures for improving cycle-to-cycle variations under high tumble combustion. SAE Technical Paper 2016-01-0694, 2016.

- M.P. Ormsby. *Turbulent flame development in a high-pressure combustion vessel*. PhD Thesis, School of Mechanical Engineering, University of Leeds, 2005.
- F. Payri, J. Benajes, X. Margot and A. Gil. CFD modeling of the in-cylinder flow in direct-injection Diesel engines. *Computers & Fluids*, 33(8): 995–1021, 2004.
- M.S. Peckham, A. Finch, and B. Campbell. Analysis of transient HC, CO, NO<sub>x</sub> and CO<sub>2</sub> emissions from a GDI engine using fast response gas analyzers. *SAE International Journal of Engines*, 4 (1): 1513–1522, 2011.
- N. Peters. The turbulent burning velocity for large-scale and small-scale turbulence. *Journal of Fluid Mechanics*, 384: 107–132, 1999.
- A. Pires Da Cruz, A. M. Dean, and J. M. Grenda. A numerical study of the laminar flame speed of stratified methane/air flames. *Proceedings of the Combustion Institute*, 28 (2): 1925–1932, 2000.
- C. D. Rakopoulos, G. M. Kosmadakis, and E. G. Pariotis. Critical evaluation of current heat transfer models used in CFD in-cylinder engine simulations and establishment of a comprehensive wall-function formulation. *Applied Energy*, 87 (5): 1612–1630, 2010.
- C. J. Rallis and A. M. Garforth. The determination of laminar burning velocity. *Progress in Energy and Combustion Science*, 6 (4): 303–329, 1980.
- D.B. Rhodes and J.C. Keck. Laminar burning speed measurements of indolene-air-diluent mixtures at high pressures and temperatures. SAE Technical Paper 850047, 1985.
- H.R. Ricardo. Recent research work on the internal-combustion engine. SAE Technical Paper 220001, 1922.
- C.M. Robeck and J.L. Ellzey. Simulation of stratified charge combustion. SAE Technical Paper 981454, 1998.

- P.J. Roberts, A. Kountouriotis, P. Okroj, P. Aleiferis, and B. Cooper. Effects of valve deactivation on thermal efficiency in a direct injection spark ignition engine under dilute conditions. SAE Technical Paper 2018-01-0892, 2018.
- D. Robertson, G. Conway, C. Chadwell, J. McDonald, D. Barba, M. Struhldreher and A. Birckett. Predictive GT-Power Simulation for VNT Matching on a 1.6 L Turbocharged GDI Engine. SAE Technical Paper 2018-01-0161, 2018.
- T.W. Ryan and S.S. Lestz. The laminar burning velocity of isooctane, n-heptane, methanol, methane, and propane at elevated temperature and pressures in the presence of a diluent. SAE Technical Paper 800103, 1980.
- S. Samuel, D. Morrey, I. Whelan, and A. Hassaneen. Combustion characteristics and cycle-by-cycle variation in a turbocharged-intercooled gasoline direct-injected engine. SAE Technical Paper 2010-01-0348, 2010.
- H. Sandquist, R. Lindgren, and I. Denbratt. Sources of hydrocarbon emissions from a direct injection stratified charge spark ignition engine. SAE Technical Paper 2000-01-1906, 2000.
- A. Schmid, M. Grill, H. Berner, M. Bargende, S. Rossa, and M. Böttcher. Development of a quasi-dimensional combustion model for stratified SI-engines. SAE Technical Paper 2009-01-2659, 2009.
- S.J. Schmieg. Aspects of HC-SCR catalyst durability for lean-burn engine exhaust aftertreatment. *SAE International Journal of Fuels and Lubricants*, 3 (2): 691–709, 2010.
- M.J. Scott. *Distributions of strain rate and temperature in turbulent combustion*. PhD Thesis, School of Mechanical Engineering, University of Leeds, 1992.
- P. Sementa, B.M. Vaglieco, and F. Catapano. Thermodynamic and optical characterizations of a high performance GDI engine operating in homogeneous and stratified charge mixture conditions fueled with gasoline and bio-ethanol. *Fuel*, 96: 204–219, 2012.

- J. Serras-Pereira, P.G. Aleiferis, D. Richardson, and S. Wallace. Characteristics of ethanol, butanol, iso-octane and gasoline sprays and combustion from a multi-hole injector in a DISI engine. *SAE International Journal of Fuels and Lubricants*, 1 (1): 893–909, 2008.
- J. Serras-Pereira, P. G. Aleiferis, and D. Richardson. An analysis of the combustion behavior of ethanol, butanol, iso-octane, gasoline, and methane in a direct-injection spark-ignition research engine. *Combustion Science and Technology*, 185 (3): 484–513, 2013.
- J. Serras-Pereira, P. G. Aleiferis, and D. Richardson. An experimental database on the effects of single and split injection strategies on spray formation and spark discharge in an optical direct-injection spark-ignition engine fuelled with gasoline, iso-octane and alcohols. *International Journal of Engine Research*, 16 (7): 851–896, 2015.
- X. Shi, J. Chen, and Z. Chen. Numerical study of laminar flame speed of fuel-stratified hydrogen/air flames. *Combustion and Flame*, 163: 394–405, 2016.
- T.R.V. Silva, J.G.C. Baeta, N.A.D. Neto, A.C.T. Malaquias, M.G.F. Carvalho, and F.R. Filho. The use of split-injection technique and ethanol lean combustion on a SIDI engine operation for reducing the fuel consumption and pollutant emissions. SAE Technical Paper 2017-36-0259, 2017.
- M. Sjeric, D. Kozarac, and G. Sagi. Development of a stratified fractal combustion model. *XXIII JUMV International Automotive Conference "Science and motor vehicles 2011"*, 2011.
- M. Sjeric, D. Kozarac, and R. Tatschl. Modelling of early flame kernel growth towards a better understanding of cyclic combustion variability in SI engines. *Energy Conversion and Management*, 103: 895–909, 2015.
- M. Sjeric, I. Taritas, R. Tomic, M. Blazic, D. Kozarac, and Z. Lulic. Efficiency improvement of a spark-ignition engine at full load conditions using exhaust gas

- recirculation and variable geometry turbocharger - numerical study. *Energy Conversion and Management*, 125: 26–39, 2016.
- J.K. Smith, P. Roberts, A. Kountouriotis, D. Richardson, P. Aleiferis, and D. Ruprecht. Thermodynamic modelling of a stratified charge spark ignition engine. *International Journal of Engine Research (online first)*, 2018.
- D.B. Spalding and B.E. Launder. *Mathematical Models of Turbulence*. Academic Press, London, England, 1972.
- R.H. Stanglmaier, J. Li, and R.D. Matthews. The effect of in-cylinder wall wetting location on the HC emissions from SI engines. SAE Technical Paper 1999-01-0502, 1999.
- R. Stone. *Introduction to internal combustion engines*. Palgrave Macmillan, 2012.
- R.J. Tabaczynski. Turbulence and turbulent combustion in spark-ignition engines. *Progress in energy and combustion science*, 2 (3): 143–165, 1976.
- D. Takahashi, K. Nakata, Y. Yoshihara, and T. Omura. Combustion development to realize high thermal efficiency engines. *SAE International Journal of Engines*, 9 (3): 1486–1493, 2016.
- D. Takaki, H. Tsuchida, T. Kobara, M. Akagi, T. Tsuyuki, and M. Nagamine. Study of an EGR system for downsizing turbocharged gasoline engine to improve fuel economy. SAE Technical Paper 2014-01-1199, 2014.
- H. Tennekes and J.L. Lumley. *A first course in turbulence*. MIT Press, Cambridge, Massachusetts, 1972.
- S.R. Turns. *An introduction to combustion: concepts and applications*. McGraw-Hill, New York, 1996.
- S. Verhelst and C.G.W. Sheppard. Multi-zone thermodynamic modelling of spark-ignition engine combustion - an overview. *Energy Conversion and Management*, 50 (5): 1326–1335, 2009.

- I. Vibe. *Halbempirische formel dur die verbrennungsgeschwindigkeit*, pages 156–159, Springer Verlag, 1964.
- S. Wadekar, M. Oevermann, and A. Lipatnikov. Large eddy simulation of stratified combustion in spray-guided direct injection spark-ignition engine. SAE Technical Paper 2018-01-1420, 2018.
- J. Wallesten, A. Lipatnikov, and J. Chomiak. Modeling of stratified combustion in a direct-ignition, spark-ignition engine accounting for complex chemistry. *Proceedings of the Combustion Institute*, 29 (1): 703–709, 2002.
- J. Wheeler, D. Polovina, S. Ramanathan, K. Roth, D. Manning, and J. Stein. Increasing EGR tolerance using high tumble in a modern GTDI engine for improved low-speed performance, 2013. SAE Technical Paper 2013-01-1123, 2013.
- B. Williams, P. Ewart, R. Stone, H. Ma, H. Walmsley, R. Cracknell, R. Stevens, D. Richardson, J. Qiao, and S. Wallace. Multi-component quantitative PLIF: Robust engineering measurements of cyclic variation in a firing spray-guided gasoline direct injection engine. SAE Technical Paper 2008-01-1073, 2008.
- B. Williams, P. Ewart, X. Wang, R. Stone, H. Ma, H. Walmsley, R. Cracknell, R. Stevens, D. Richardson, H. Fu, and S. Wallace. Quantitative planar laser-induced fluorescence imaging of multi-component fuel/air mixing in a firing gasoline-direct-injection engine: Effects of residual exhaust gas on quantitative PLIF. *Combustion and Flame*, 157 (10): 1866–1878, 2010.
- N.D. Wilson, A.J. Watkins, and C. Dopson. Asymmetric valve strategies and their effect on combustion. SAE Technical Paper 930821, 1993.
- M. Wirth, W.F. Piock, G.K. Fraidl, P. Schoeggl, and E. Winklhofer. Gasoline DI engines: The complete system approach by interaction of advanced development tools. SAE Technical Paper 980492, 1998.
- P.O. Witze, J.K. Martin and C. Borgnakke. Measurements and Predictions of the

- Precombustion Fluid Motion and Combustion Rates in a Spark Ignition Engine. SAE Technical Paper 831697, 1983.
- G. Woschni. A universally applicable equation for the instantaneous heat transfer coefficient in the internal combustion engine. SAE Technical paper 670931, 1967.
- C.M. Wu, C.E. Roberts, R.D. Matthews, and M.J. Hall. Effects of engine speed on combustion in SI engines: Comparisons of predictions of a fractal burning model with experimental data. SAE Technical Paper 932714, 1993.
- V. Yakhot and S.A. Orszag. Renormalization group analysis of turbulence. i. basic theory. *Journal of Scientific Computing*, 1 (1): 3–51, 1986.
- V. Yakhot, S.A. Orszag, S. Thangam, T.B. Gatski, and C.G. Speziale. Development of turbulence models for shear flows by a double expansion technique. *Physics of Fluids A: Fluid Dynamics*, 4 (7): 1510–1520, 1992.
- Ya B. Zeldovich. *The Mathematical theory of combustion and explosions*. Consultants Bureau, 1985.
- Z. Zhang, H. Zhang, T. Wang, and M. Jia. Effects of tumble combined with EGR (exhaust gas recirculation) on the combustion and emissions in a spark ignition engine at part loads. *Energy*, 65: 18–24, 2014.
- F. Zhao, M.C. Lai, and D.L. Harrington. Automotive spark-ignited direct-injection gasoline engines. *Progress in Energy and Combustion Science*, 25 (5): 437–562, 1999.
- V.L. Zimont. Theory of turbulent combustion of a homogeneous fuel mixture at high Reynolds numbers. *Combustion, Explosion and Shock Waves*, 15: 305–311, 1979.

# Appendix A

## Fuel specification

The fuel specification provided here is a direct copy of the specification provided by the fuel supplier.

| Feature                                | Units                 | Results | Limits  |         | Method       |
|--|-----------------------|---------|---------|---------|--------------|
|  |                       |         | Minimum | Maximum |              |
| Density 15°C                           | kg/m <sup>3</sup>     | 751.5   | 743.0   | 756.0   | EN ISO 12185 |
| Clear and Bright at -7°C               | -                     | Pass    | -       | -       | ASTM D4176-1 |
| I.B.Pt.                                | °C                    | 37.8    |         |         | EN ISO 3405  |
| % Evaporated at 70°C, E70              | %(V)                  | 40.4    | 34.0    | 46.0    | EN ISO 3405  |
| % Evaporated at 100°C, E100            | %(V)                  | 56.5    | 54.0    | 62.0    | EN ISO 3405  |
| % Evaporated at 150°C, E150            | %(V)                  | 87.2    | 86.0    | 94.0    | EN ISO 3405  |
| F.B.Pt.                                | °C                    | 181.8   | 170.0   | 195.0   | EN ISO 3405  |
| Residue                                | %(V)                  | 0.8     | -       | 2.0     | EN ISO 3405  |
| RON (corrected)                        |                       | 96.3    | 95.0    | 98.0    | EN ISO 5164  |
| MON (corrected)                        |                       | 86.0    | 85.0    | 89.0    | EN ISO 5163  |
| Olefin content                         | %(V)                  | 7.3     | 6.0     | 13.0    | EN ISO 22854 |
| Aromatic content                       | %(V)                  | 31.0    | 25.0    | 32.0    | EN ISO 22854 |
| Benzene content                        | %(V)                  | 0.2     | -       | 1.0     | EN 238       |
| Saturate content                       | %(V)                  | 51.7    |         |         | EN ISO 22854 |
| Vapour pressure (DVPE) 37.8°C          | kPa                   | 57.1    | 56.0    | 60.0    | EN13016-1    |
| Water content                          | %(V)                  | 0.043   | -       | 0.050   | EN ISO 12937 |
| Oxidation stability (induction period) | min.                  | > 480   | 480     | -       | EN ISO 7536  |
| Oxygen content                         | %(m)                  | 3.67    | 3.30    | 3.70    | EN ISO 22854 |
| Gum - washed                           | mg/100cm <sup>3</sup> | <0.5    | -       | 4.0     | EN ISO 6246  |
| Sulphur content                        | mg/kg                 | <3.0    | -       | 10.0    | EN ISO 20846 |
| Copper corrosion, 3hrs at 50°C         | -                     | 1A      | -       | -       | EN ISO 2160  |
| Lead content                           | mg/l                  | <2.5    | -       | 5.0     | EN 237       |
| Phosphorous content                    | mg/l                  | <0.2    | -       | 1.3     | ASTM D3231   |
| Ethanol                                | %(V)                  | 10.0    | 9.0     | 10.0    | EN ISO 22854 |
| Carbon content                         | %(m)                  | 83.38   |         |         | ASTM D5291   |
| Hydrogen content                       | %(m)                  | 12.95   |         |         | ASTM D5291   |

| Feature                       | Units             | Results | Limits  |         | Method      |
|-------------------------------|-------------------|---------|---------|---------|-------------|
|                               |                   |         | Minimum | Maximum |             |
| C/H mass ratio                |                   | 6.44    |         |         | Calculation |
| C/O mass ratio                |                   | 22.72   |         |         | Calculation |
| Atomic H/C ratio              |                   | 1.8507  |         |         | Calculation |
| Atomic H/O ratio              |                   | 56.01   |         |         | Calculation |
| Stoichiometric Air/Fuel ratio |                   | 13.88   |         |         | SAE J1829   |
| Gross heat of combustion      | MJ/kg             | 44.52   |         |         | IP 12       |
| Net heat of combustion        | MJ/kg             | 41.78   |         |         | IP 12       |
| Density at 20°C               | kg/m <sup>3</sup> | 747.5   |         |         | ASTM D4052  |